

**CLASS VI PERMIT APPLICATION NARRATIVE
40 CFR 146.82(a)**

CLEAN ENERGY SYSTEMS MENDOTA



These documents were prepared by Schlumberger Technology Corporation and delivered to Clean Energy Systems



Plan revision number: 1.2

Plan revision date: September 20, 2021

Pages of this document contain Confidential Business Information that is privileged and is exempt from public disclosure. Such information shall be used or disclosed by EPA only to the extent, and by means of the procedures, set forth in 40 CFR Part 2 – Subpart B, in order to evaluate this Class VI Underground Injection Control permit application. The following figures contain Confidential Business Information:

- Figure 15. CONFIDENTIAL BUSINESS INFORMATION: 2D seismic line map, shotpoints, and area wells showing the 3 and 5-mile radii from Mendota plant site. The light blue lines over the Gill Ranch gas field are faults. This image displays data from SEI (2019), and it is marked as Confidential Business Information.
- Figure 16. CONFIDENTIAL BUSINESS INFORMATION: Seismic well tie: line W-SJ-202 and Sallaberry 1-6 well (API number 4019215350000). This image displays SEI data (2019), and it is marked as Confidential Business Information.
- Figure 17. CONFIDENTIAL BUSINESS INFORMATION: W-SJ-202 2D seismic line (depth) with interpreted horizons and faults. This image displays SEI data (2019), and it is marked as Confidential Business Information.
- Figure 18. CONFIDENTIAL BUSINESS INFORMATION: W-SJ-209 2D seismic line (depth) with interpreted horizons and faults. This image displays SEI data (2019), and it is marked as Confidential Business Information.
- Figure 19. CONFIDENTIAL BUSINESS INFORMATION: W-SJ-013W 2D seismic line (in depth) with interpreted horizons and faults. This image displays SEI data (2019), and it is marked as Confidential Business Information.
- Figure 20. CONFIDENTIAL BUSINESS INFORMATION: 3D view (facing SE) of interpreted faults on the 2D seismic lines and basement surface. Dotted lines are projected faults (color coded by horizon) or projected fault plane. A legacy Gill Ranch field structure map is inserted at the Second Panoche. This image displays SEI data (2019), and it is marked as Confidential Business Information.
- Figure 21. CONFIDENTIAL BUSINESS INFORMATION: 3D perspective of the depth-integrated geophysical model. This image displays SEI data (2019), and it is marked as Confidential Business Information.
- Figure 35. CONFIDENTIAL BUSINESS INFORMATION: Injection well cross-section traverse map, N-S and E-W. This image displays SEI data (2019), and it is marked as Confidential Business Information.
- Figure 36. CONFIDENTIAL BUSINESS INFORMATION: 3D perspective of N-S and E-W porosity cross sections at Mendota_INJ_1. This image displays SEI data (2019), and it is marked as Confidential Business Information.
- Figure 49. CONFIDENTIAL BUSINESS INFORMATION: USDW estimated using resistivity measured in wells near the Mendota site. This image displays IHS data (IHS, 2019), and it is marked as Confidential Business Information.

Contents

1.	Project Background and Contact Information	9
1.1	Preconstruction Application Intention	9
1.2	Project Background	11
1.3	Abbreviations	13
1.4	Units	14
2.	Site Characterization	15
2.1	Regional Geology, Hydrogeology, and Local Structural Geology [40 CFR 146.82(a)(3)(vi)]	15
2.2	Maps and Cross Sections of the Area of Review (AoR) [40 CFR 146.82(a)(2), 146.82(a)(3)(i)]	22
2.3	Faults and Fractures [40 CFR 146.82(a)(3)(ii)]	29
2.3.1	Geophysical Workflow	29
2.3.2	Fault Seal Analysis	31
2.3.3	Uncertainty, Additional Data, and Analysis	31
2.4	Injection and Confining Zone Details [40 CFR 146.82(a)(3)(iii)]	42
2.4.1	Structural Mapping	42
2.4.2	Petrophysics	42
2.4.3	Geocellular Modeling and Volumetrics	50
2.4.4	Pre-Operational Testing Requirements	63
2.5	Geomechanical and Petrophysical Information [40 CFR 146.82(a)(3)(iv)]	64
2.6	Seismic History [40 CFR 146.82(a)(3)(v)]	66
2.7	Hydrologic and Hydrogeologic Information [40 CFR 146.82(a)(3)(vi), 146.82(a)(5)].	72
2.7.1	Depth to the Deepest USDWs – 40 CFR 146.93(c)(1)(x)	72
2.7.2	Local Near-Surface Groundwater	74
2.8	Geochemistry [40 CFR 146.82(a)(6)]	78
2.8.1	Characteristics of Injection Zone Formation Water	78
2.8.2	Mineral Composition of the Injection Zone	79
2.8.3	Composition of the Injectate	80
2.8.4	Geochemical Modeling Setup	80
2.8.5	Simulated Reaction Pathways	81
2.9	Other Information (Including Surface Air and/or Soil Gas Data, if Applicable)	86
2.10	Site Suitability [40 CFR 146.83]	86
3.	AoR and Corrective Action	87
4.	Financial Responsibility	87

5.	Injection Well Construction.....	89
5.1	Proposed Stimulation Program [40 CFR 146.82(a)(9)]	92
5.2	Construction Procedures [40 CFR 146.82(a)(12)]	92
5.2.1	Surface Wellhead Configuration.....	92
5.2.2	Casing	93
5.2.3	Discussion on Well Construction.....	95
5.2.4	Tubing and Packer	96
5.2.5	Cement	97
6.	Pre-Operational Logging and Testing.....	99
7.	Well Operation.....	99
7.1	Operational Procedures [40 CFR 146.82(a)(10)].....	100
7.2	Proposed Carbon Dioxide Stream [40 CFR 146.82(a)(7)(iii) and (iv)]	101
8.	Testing and Monitoring.....	103
9.	Injection Well Plugging	103
10.	Post-Injection Site Care (PISC) and Site Closure.....	103
11.	Emergency and Remedial Response.....	104
12.	Injection Depth Waiver and Aquifer Exemption Expansion	104
13.	Other Information	104
14.	Approval	105
15.	Disclaimer Statement.....	107
16.	References.....	107
17.	Appendix A: Stratigraphic Nomenclature, San Joaquin Basin.....	112

List of Figures

Figure 1. The phases of a Class VI project (EPA, 2018).....	10
Figure 2. Mendota site location showing surface faults (USGS, 2019a), San Joaquin Basin (USGS, 2005), and nearby wells (IHS, 2019).	12
Figure 3. San Joaquin basin depositional model showing structural and stratigraphic traps. The yellow star indicates the proposed Mendota_INJ_1 location. GR, Gill Ranch. CR, Cheney Ranch (Hosford Scheirer & Magoon, 2007b).....	17
Figure 4a-d. San Joaquin basin depositional model showing possible depositional scenarios for the location of Mendota_INJ_1; modified from Hosford Scheirer and Magoon (2007b).19	
Figure 5. Mendota stratigraphic column and effective porosity log. Right-most track shows the Sears (Willis) tower for scale.....	20
Figure 6. Primary formations at the Mendota site and their intended use.	21
Figure 7. Subsurface geology and legacy wells surrounding the Mendota site, SW-NE cross section.	23
Figure 8. Subsurface geology and legacy wells surrounding the Mendota site, NW-SE cross section.	24
Figure 9. Ten wells used in petrophysical analysis and well correlation, showing the locations of cross sections N-S, W-E, and W-E 2, shown in Figure 10, Figure 11, and Figure 12, respectively.	25
Figure 10. N-S cross section (location shown in Figure 9) which shows 5 out of 10 petrophysical wells used in analysis of injection and confining rock properties. The Mendota_INJ_1 is located between B. B. Company 1 and Sterling-Coleman 1 wells. Tracks left to right are volume of clay (VCL), measured depth, zone log, facies calculated from VCL, and zone color fill between wells.....	26
Figure 11. W-E cross section (location shown in Figure 9). Tracks left to right are VCL, MD, zone log, facies calculated from VCL, and zone color fill between wells.....	27
Figure 12. W-E 2 cross section (location shown in Figure 9). Tracks left to right are VCL, MD, zone log, facies calculated VCL, and zone color fill between wells.	27
Figure 13. Formation surface maps generated from well tops and seismic data; well symbols indicate wells that are estimated to penetrate the mapped formation.	28
Figure 14. Formation isochore maps.	29
Figure 15. CONFIDENTIAL BUSINESS INFORMATION: 2D seismic line map, shotpoints, and area wells showing the 3 and 5-mile radii from Mendota plant site. The light blue lines over the Gill Ranch gas field are faults. This image displays data from SEI (2019), and it is marked as Confidential Business Information.	33
Figure 16. CONFIDENTIAL BUSINESS INFORMATION: Seismic well tie: line W-SJ-202 and Sallaberry 1-6 well (API number 4019215350000). This image displays SEI data (2019), and it is marked as Confidential Business Information.....	34
Figure 17. CONFIDENTIAL BUSINESS INFORMATION: W-SJ-202 2D seismic line (depth) with interpreted horizons and faults. This image displays SEI data (2019), and it is marked as Confidential Business Information.....	35
Figure 18. CONFIDENTIAL BUSINESS INFORMATION: W-SJ-209 2D seismic line (depth) with interpreted horizons and faults. This image displays SEI data (2019), and it is marked as Confidential Business Information.....	36

Figure 19. CONFIDENTIAL BUSINESS INFORMATION: W-SJ-013W 2D seismic line (in depth) with interpreted horizons and faults. This image displays SEI data (2019), and it is marked as Confidential Business Information. 37

Figure 20. CONFIDENTIAL BUSINESS INFORMATION: 3D view (facing SE) of interpreted faults on the 2D seismic lines and basement surface. Dotted lines are projected faults (color coded by horizon) or projected fault plane. A legacy Gill Ranch field structure map is inserted at the Second Panoche. This image displays SEI data (2019), and it is marked as Confidential Business Information. 38

Figure 21. CONFIDENTIAL BUSINESS INFORMATION: 3D perspective of the depth-integrated geophysical model. This image displays SEI data (2019), and it is marked as Confidential Business Information. 39

Figure 22. Fault 13 terminates within the Moreno shale. The Mendota_INJ_1 wellbore, which targets the Second Panoche injection sand, is shown in green with MD annotated in white text. Fault 13 is colored by fault clay prediction content based on the SGR algorithm, the results of which indicate the Moreno shale smearing along the fault. 40

Figure 23. Different fault displacement scenarios at Mendota_INJ_1 regarding Fault 13. 41

Figure 24. N-S cross section showing petrophysical analysis results and wells nearest to Mendota_INJ_1. From left to right, the tracks show PIGE, KINT, MD, zone log, sand and shale lithologies as calculated from VCL, and net lithology values for sand and shale per zone. 46

Figure 25. W-E cross section showing petrophysical analysis results. From left to right, the tracks show PIGE, KINT, MD, zone log, sand and shale lithologies as calculated from VCL, and net lithology values for sand and shale per zone. 46

Figure 26. W-E 2 cross section showing petrophysical analysis results. From left to right, the tracks show effective porosity (PIGE), permeability (KINT), MD, zone log, sand and shale lithologies as calculated from VCL, and net lithology values for sand and shale per zone. 47

Figure 27: Net thickness maps of Moreno shale and First and Second Panoche sands calculated based on VCL greater than or less than 30%; the white diamond denotes Mendota_INJ_1. 47

Figure 28. Example of PIGE and KINT upscaled well logs results for B.B. Company 1 and Sterling-Coleman 1 (closest petrophysical wells to Mendota_INJ_1 at different scales.. 52

Figure 29. Porosity histograms of well logs, upscaled cells, and model cells. 53

Figure 30. Permeability histograms of well logs, upscaled cells, and model cells. 54

Figure 31. Porosity-permeability crossplots of well logs and upscaled cells. 55

Figure 32. Porosity-permeability crossplot model cells colored by formation. 56

Figure 33. Modeled average porosity maps for each formation. 57

Figure 34. Modeled permeability thickness (KH) maps for each formation. 58

Figure 35. CONFIDENTIAL BUSINESS INFORMATION: Injection well cross-section traverse map, N-S and E-W. This image displays SEI data (2019), and it is marked as Confidential Business Information. 59

Figure 36. CONFIDENTIAL BUSINESS INFORMATION: 3D perspective of N-S and E-W porosity cross sections at Mendota_INJ_1. This image displays SEI data (2019), and it is marked as Confidential Business Information. 60

Figure 37. Effective porosity model cross section (N-S). 60

Figure 38. Volume clay model cross section (N-S). 61

Figure 39. Permeability model cross section (N-S)..... 61

Figure 40. Effective porosity model cross section (E-W)..... 62

Figure 41. Volume shale model cross section (E-W). 62

Figure 42. Permeability model cross-section (E-W)..... 63

Figure 43. Density, acoustic, and elastic properties in the Moreno shale..... 65

Figure 44. Relative earthquake risk (left) and earthquake map from the CEMA GIS unit (right) (CEMA, 2010). The red star is the location of the Mendota site..... 68

Figure 45. Regional faulting from the Department of Conservation (1998)(left) and quakes with magnitudes greater than 2.5 since 1900 (USGS, 2019a) (right). Red star represents the location of the Mendota site..... 69

Figure 46. Historical earthquakes near AoR greater than 2.5 since 1900. Red star represents Mendota site..... 70

Figure 47. All earthquakes (red) located by the USGS Advanced National Seismic Survey within a 10-mile radius of the proposed injection site since 2000 with the year and magnitude shown. Faults provided by the USGS are also shown in blue with the 10-mile radius in orange. Red star represents Mendota site. 71

Figure 48. Wells used to calculate the depth to the deepest USDW..... 73

Figure 49. CONFIDENTIAL BUSINESS INFORMATION: USDW estimated using resistivity measured in wells near the Mendota site. This image displays IHS data (IHS, 2019), and it is marked as Confidential Business Information. 74

Figure 50. Map of water wells and cross section depicting water wells and elevation of lowermost USDW. The vertical distance from the First Panoche sandstone to the calculated lowermost USDW (1,415 ft TVDSS)..... 76

Figure 51. Potentiometric map of the approximate shallowest groundwater surface..... 77

Figure 52. Changes of the amount of the minerals from the addition of CO₂ and O₂ in geochemical modeling. 82

Figure 53. Aqueous composition after the addition of CO₂ and O₂ in geochemical modeling. ... 83

Figure 54. Mineral volume and mass after the addition of CO₂ and O₂ in the geochemical modeling. 85

Figure 55. Mendota_INJ_1 well construction diagram. 90

Figure 56. Pore and fracture gradients used for well construction. 91

Figure 57. Temperature gradient used for well construction..... 91

Figure 58. Surface wellhead configuration..... 92

Figure 59. Stratigraphic column from northern San Joaquin Basin showing Cretaceous to Lower Paleocene section; modified from (Hosford Scheirer & Magoon, 2007a). 113

List of Tables

Table 1. Well control points for structural model of injection and confining formations.	42
Table 2. Wells used to characterize petrophysical properties within the AoR.	44
Table 3. Average porosity and permeability of injection and confining zones as calculated from NAPA AVE A/1.	49
Table 4. Mineralogy summary from core XRD for NAPA AVE A 1.	50
Table 5. Storage capacity input parameters and results showing P50 capacity estimate in million tonnes.	63
Table 6. Historical earthquakes near AoR greater than 2.5 since 1900. X and Y values are projected in California State Plane Zone IV, NAD27.	71
Table 7. Salinity of the formation waters from the oil and gas fields near the proposed Mendota site (California Department of Conservation, Division of Oil, Gas and Geothermal Resources, 1998).	78
Table 8. Gill Ranch wells from USGS study, showing top perforation and BFW (3,000 ppm) (Davis, Bennett, Metzger, & al., 2018) (CalGEMS, 2020).	78
Table 9. Estimated mineral composition (wt.%) for the Panoche formation used in geochemical modeling.	80
Table 10. Composition of the injectate (mass fractions).	80
Table 11. Chemical composition of the initial solution for geochemical modeling.	81
Table 12. Casing design factors.	93
Table 13. Casing design loads.	93
Table 14: Mendota_INJ_1 openhole diameters and intervals.	94
Table 15. Mendota_INJ_1 casing specifications.	95
Table 16. Mendota_INJ_1 tubing specifications.	96
Table 17. Mendota_INJ_1 packer specifications.	96
Table 18. Surface section fluid placement in annulus.	97
Table 19. Intermediate section fluid placement in annulus.	97
Table 20. Long-string section fluid placement in annulus.	98
Table 21. Proposed operational conditions.	102
Table 22. Approval.	106

Disclaimer

Any interpretation, research, analysis, data, results, estimates, or recommendation furnished with the services or otherwise communicated by Schlumberger to Clean Energy Systems at any time in connection with the services are opinions based on inferences from measurements, empirical relationships, and/or assumptions, which inferences, empirical relationships, and/or assumptions are not infallible, and with respect to which professionals in the industry may differ. Accordingly, Schlumberger cannot and does not warrant the accuracy, correctness, or completeness of any such interpretation, research, analysis, data, results, estimates, or recommendation. Clean Energy Systems acknowledges that it is accepting the services "as is", that Schlumberger makes no representation or warranty, express or implied, of any kind or description in respect thereto. Specifically, Clean Energy Systems acknowledges that Schlumberger does not warrant that any interpretation, research, analysis, data, result, estimate, or recommendation is fit for a particular purpose, including but not limited to compliance with any government request or regulatory requirement. Clean Energy Systems further acknowledges that such services are delivered with the explicit understanding and agreement that any action taken based on the services received shall be at its own risk and responsibility and no claim shall be made against Schlumberger as a consequence thereof.

To the extent permitted by applicable law, Clean Energy Systems shall not provide this report to any third party in connection with raising finance or procuring investment (other than pursuant to an equity capital raising on a public market) without a No Reliance Letter first being completed and signed by the third party and provided to Schlumberger. The form of the No Reliance Letter being agreed to by both Clean Energy Systems and Schlumberger. Subject to this requirement and upon full payment of applicable fees, copyright ownership in this report shall vest with Clean Energy Systems. Schlumberger grants no title or license or right to Clean Energy Systems to use Schlumberger's Intellectual Property except as necessary for Clean Energy Systems to use the report.

Copyrights

Copyright © 2021, Schlumberger

All rights reserved.

Trademarks

An asterisk (*) denotes a mark of Schlumberger. Other companies or product names mentioned in this document are used for identification purposes only and may be trademarks of their respective owners.

1. Project Background and Contact Information

GSDT Submission - Project Background and Contact Information

GSDT Module: Project Information Tracking

Tab(s): General Information tab; Facility Information and Owner/Operator Information tab

Please use the checkbox(es) to verify the following information was submitted to the GSDT:

Required project and facility details [**40 CFR 146.82(a)(1)**]

1.1 Preconstruction Application Intention

Clean Energy Systems (CES) has contracted Schlumberger to complete the technical analysis required to prepare a Class VI (GS) preconstruction permit application (EPA, 2019a) for the CES Mendota carbon storage site in California. An evaluation of the geologic, hydrogeologic, and area of review (AoR) delineation has been developed using available public data, purchased well data, and purchased 2D seismic data. CES is seeking approval of this Class VI preconstruction permit application from the Environmental Protection Agency (EPA).

The EPA (EPA, 2018), outlined five phases of a Class VI Project (Figure 1). Based on the descriptions of each phase, CES is in the preconstruction phase. The EPA understands that there will be uncertainties regarding the evaluation of the proposed Mendota site. Referring to underground injection control, the EPA states (EPA, 2019b): *“Because all of the information needed to evaluate the suitability of a proposed GS site will not be available at the time the permit application is submitted, there will likely be uncertainties regarding some aspects of the proposed site or the injection operation”*. Because of this uncertainty, CES plans to acquire site-specific data (characterization well, 3D seismic data, groundwater, etc.) to reduce the uncertainty necessary for EPA approval of future phases of the project. Before CES makes a large financial investment in acquiring these site-specific data, CES has two primary objectives for submitting this preconstruction application:

1. In this early phase of the project, CES intends to make the EPA aware of the intention to develop a carbon capture and sequestration (CCS) project at the Mendota site.
2. CES requests that the EPA review this preconstruction application, and, if the site characteristics and development plan are suitable, grant CES approval pending the acquisition of the site-specific data necessary to validate all aspects of the Mendota site suitability and underground sources of drinking water (USDW) nonendangerment.

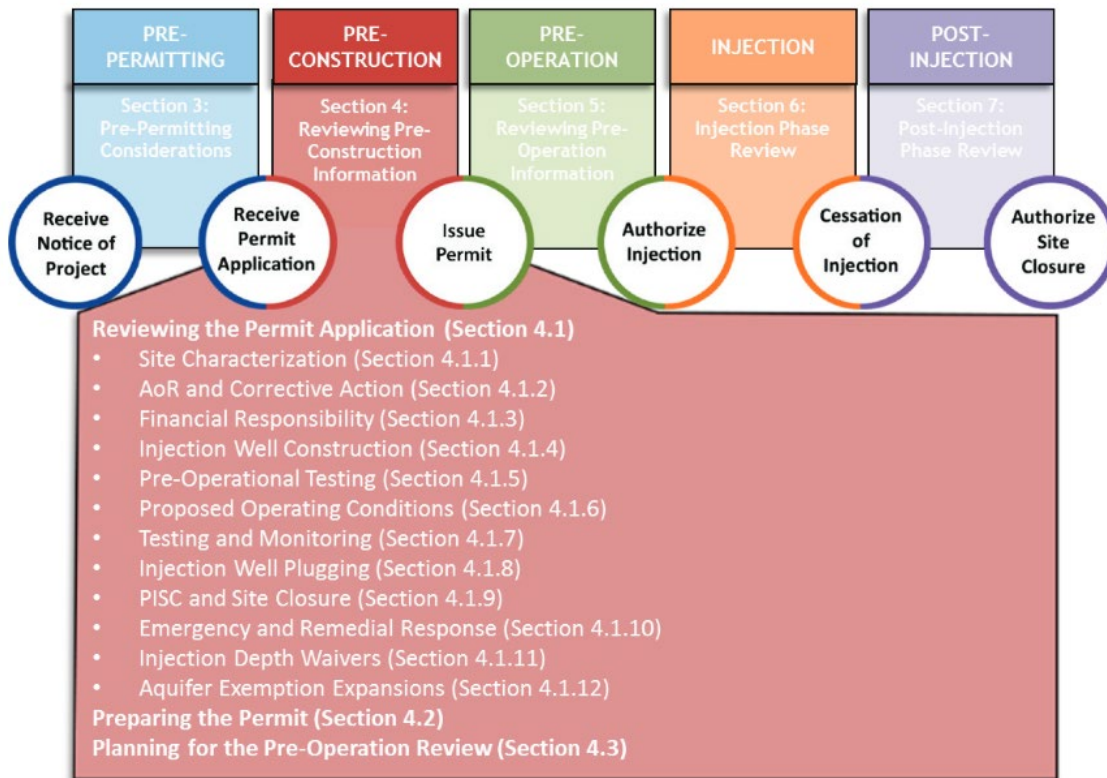


Figure 1. The phases of a Class VI project (EPA, 2018).

This narrative document is one of the several documents that were prepared by Schlumberger and delivered to CES. These documents were prepared to support the CES preconstruction permit application to the EPA. This narrative document summarizes the detailed information provided in the following supplemental document templates provided by the EPA:

- Attachment A: Summary of Requirements Class VI Operating (Schlumberger, 2021a)
- Attachment B: Area of Review and Corrective Action Plan (Schlumberger, 2021b)
- Attachment C: Testing and Monitoring Plan (Schlumberger, 2021c)
- Attachment D: Injection Well Plugging Plan (Schlumberger, 2021d)
- Attachment E: Post-Injection Site Care and Site Closure Plan (Schlumberger, 2021e)
- Attachment F: Emergency and Remedial Response Plan (Schlumberger, 2021f)
- Attachment G: Construction Details Clean Energy Systems Mendota (Schlumberger, 2021g)
- Attachment H: Financial Assurance Demonstration (Schlumberger, 2021h)
- Class VI Permit Application Narrative (Schlumberger, 2021i)
- Quality Assurance and Surveillance Plan (Schlumberger, 2021j)

1.2 Project Background

Clean Energy Systems (CES) is developing a series of carbon negative energy (CNE) plants in California. CNE plants use waste biomass as feedstock and gasification technology to produce a renewable syngas. The hydrocarbon syngas then passes through CES' proprietary oxy-combustion system generating a pure stream of high-pressure steam and CO₂ to power electrical turbines. After power generation, the drive gas is condensed, and the CO₂ is captured and compressed to a supercritical state for injection deep into the subsurface for geologic sequestration (GS). This process is also known as carbon capture and sequestration (CCS).

CES is submitting this preconstruction phase application for the Mendota CNE project site located near Mendota, California, in Fresno County. CO₂ from the oxy-combustion system will be captured and stored onsite via GS. This preconstruction application was prepared by Schlumberger and delivered to CES.

The site map in Figure 2 shows the location of the Mendota site and the proposed Mendota_INJ_1 CO₂ injection well (T13S R15E S32, LAT LONG: 36.75585015/-120.36440423, derived from SPCS27_0404). The figure illustrates the Mendota_INJ_1 location relative to known public data such as other wells, the town of Mendota, county lines, rivers, and known faults (USGS, 2019a). There are no tribal lands near the area of review (AoR).

The anticipated CO₂ mass to be captured and injected at the Mendota site is 350,000 tonnes/year over the next 12 (4,200,000 tonnes total) to 20 years (7,000,000 tonnes total). The injection of CO₂ into the subsurface is regulated by the EPA via the Underground Injection Control (UIC) program.

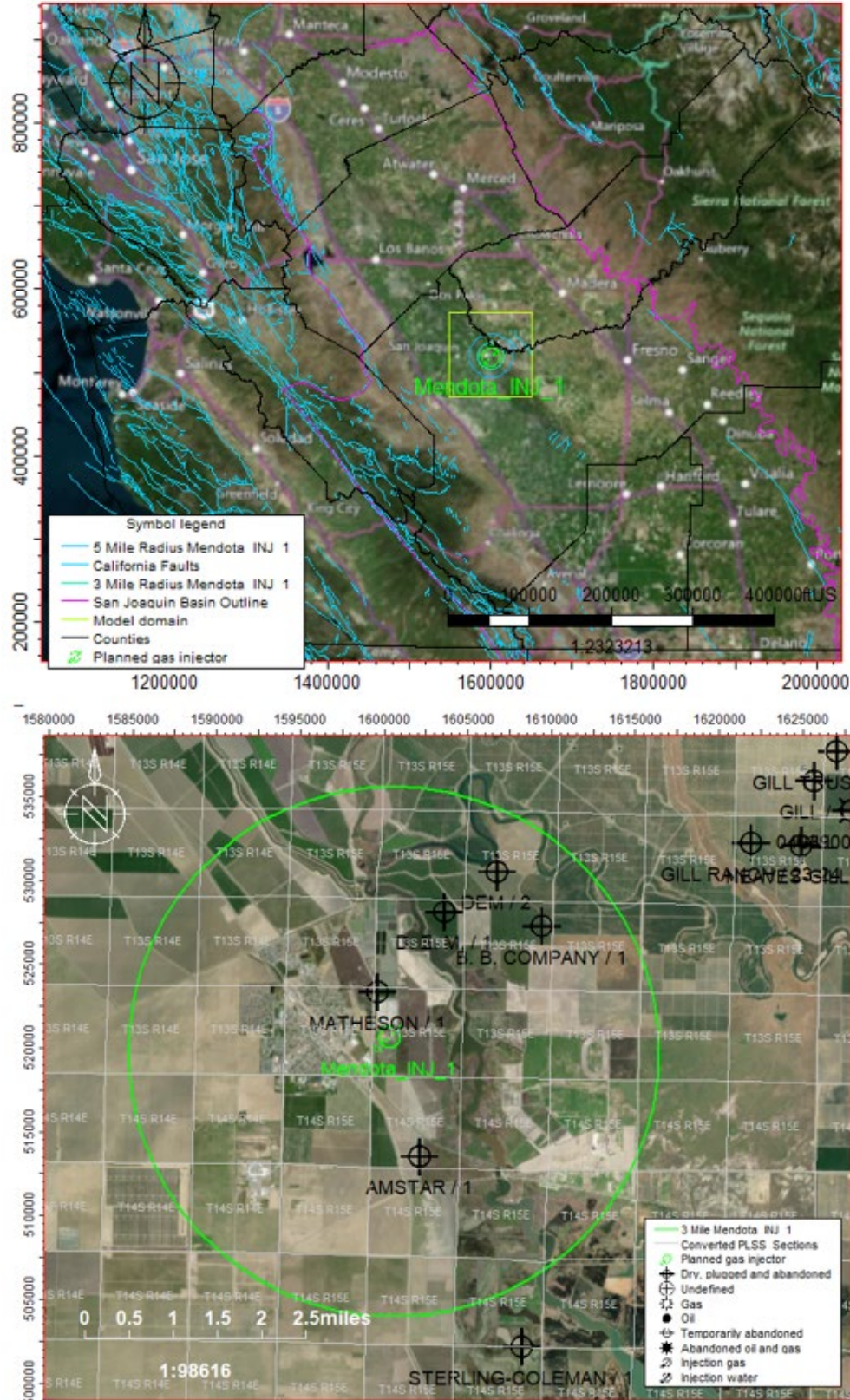


Figure 2. Mendota site location showing surface faults (USGS, 2019a), San Joaquin Basin (USGS, 2005), and nearby wells (IHS, 2019).

1.3 Abbreviations

AoR: area of review
ANSI: American National Standards Institute
API: American Petroleum Institute
BFW base of freshwater
BGS: below ground surface
CCS: carbon capture and sequestration
CalGEM: California Geologic Energy Management Division
CEMA: California Emergency Management Agency
CES: Clean Energy Systems
CNE: carbon negative energy
DOGGR: Division of Oil, Gas, and Geothermal Resources (as of 2020, CalGEM)
DST: drillstem test
DT: compressional slowness
DTS: distributed temperature sensing
EPA: Environmental Protection Agency
GL: ground level
GRFS: Gaussian random function simulation
GR: gamma ray
GS: geological sequestration
HRA: heterogeneous rock analysis
KH: permeability thickness
KINT: permeability
LAS: log ASCII standard
Mendota_INJ_1: proposed CO₂ injection well
MD: measured depth
MIT: mechanical integrity test
MWD: measurement while drilling
NPHI: neutron porosity
PISC: post-injection site care
PHIT: total porosity
PIGE: effective porosity
RHOB: bulk density
Rwa: formation water resistivity
SEM: scanning electron microscopy
SGR: shale gouge ratio
Shmax: maximum horizontal stress
Shmin: minimum horizontal stress
SP: spontaneous potential
TDS: total dissolved solids
TVD: true vertical depth
TVDSS: true vertical depth subsea
UIC: underground injection control
USDW: underground sources of drinking water
USGS: US Geological Survey

VCL: volume of clay
VME: von Mises equivalent
VSP: vertical seismic profile
Vp/Vs: compressional to shear velocity ratio
XRD: X-ray diffraction analysis
XRF: X-ray fluorescence

1.4 Units

°F: degrees Fahrenheit
ft: feet
ft³: cubic feet
ft/sec: feet/second
gAPI: API gamma ray unit
g/cm³: grams/cubic centimeter
g.ft/ cm³.s: grams per foot/cubic centimeter
in: inch
lb: pound (mass)
lb/gal: pound (mass) per gallon
Ma: mega-annum, millions of years
Md: millidarcy
miles
mg/kg: milligrams per kilogram
Mpa: megapascal
Mpsi: megapound-force/square inch
mV: millivolt
ohm.m: ohm.meter
percent, %
ppg: pounds per gallon
ppm: parts per million
psi: pounds per square inch
psi/ft: pounds per square inch/foot
p.u.: porosity units
tonne: metric tonne (megagram)

2. Site Characterization

2.1 Regional Geology, Hydrogeology, and Local Structural Geology [40 CFR 146.82(a)(3)(vi)]

The Mendota site is in the central San Joaquin Basin in Fresno County, California. The San Joaquin Basin formed as a forearc basin between the subducting Farallon plate in the west and the Sierra Nevada volcanic arc to the east, accumulating 25,000 ft of sediment overlying basement rocks capturing the last 100 million years of sedimentary and tectonic history. The San Joaquin Basin forms the southern half of California's Great Valley and is a major petroleum province.

The proposed Mendota_INJ_1 site is situated approximately 10 miles east of the late Cretaceous axis of the San Joaquin Basin, between the Gill Ranch gas field (6.5 miles northeast), and Cheney Ranch gas field (11.7 miles southwest), respectively (Figure 3). Historical gas production at Gill Ranch targeted Late Cretaceous sandstones in a low-amplitude structural closure, <100 ft, bounded by faults interpreted as high-angle reverse faults oriented NW-SE. Currently, the Gill Ranch field is primarily used for gas storage operations exploiting the properties of the reservoir sandstones (CalGEMS, 2020). Mapping depositional settings in this basin is challenging because of the varying interpretations of stratigraphic classifications over time, the changes in sea level through time, and the evolving tectonic settings from forearc margin to strike-slip (Hosford Scheirer & Magoon, 2007a).

Regional studies across the San Joaquin Basin show a Cretaceous shelf edge subparallel to the NW-SE orientation of the basin axis just west of the Gill Ranch field (shown by solid brown line in Figure 3) (Hosford Scheirer & Magoon, 2007a). West of the shelf-edge margin is an interpreted slope and basin floor with expected channel and fan deposits as depicted in Figure 4. The position of the Gill Ranch field on the Cretaceous shelf suggests that its reservoir sandstones are deltaic; these are referred to in multiple publications and well records as the Starkey sandstones. However, Panoche has also been used historically to describe the Cretaceous sandstones at Gill Ranch in published reports and in well records. Current well records from Gill Ranch indicate that gas storage takes place in the first and second Starkey sands (CalGEMS, 2020). Deltaic Starkey deposits on the shelf edge prograde into channel and fan deposits downdip. In some instances, the lower Starkey sands are considered coeval with the more distal slope Lathrop sands which are interpreted in the Panoche Formation (Figure 4a). Multiple well reports and publications refer to the shelf, slope, and basin floor sandstones as Panoche, which can be confusing. This is partly due to correlation of the subsurface stratigraphy with outcrop interpretation and a less well constrained understanding of the subsurface depositional setting and lateral correlation. Based on Panoche as a naming convention for the slope and deltaic sandstones and as a Late Cretaceous formation below the regional Moreno shale, this terminology has been retained for characterization purposes. Appendix A provides additional information on the stratigraphic relationships and nomenclature of the Cretaceous deposits in the San Joaquin basin.

In addition to the inconsistent naming convention, there is uncertainty in the depositional environment at the injection well due to the paucity of site-specific data. Figure 4b, Figure 4c,

and Figure 4d show three possible scenarios for the depositional environment expected at Mendota_INJ_1:

- Figure 4b shows a likely scenario in which the Mendota_INJ_1 well is in channel and submarine fan deposits located on the slope of the basin with an updip stratigraphic pinchout into Moreno shales.
- Figure 4c shows the modeled scenario in which the Panoche formation sandstones of different depositional environments (Figure 4b and Figure 4d) are connected (labeled as Lathrop sand to the west and Third Starkey sands to the east). Because of the correlation in well logs across the model domain, a conservative approach was taken to connect these sandstones for reservoir characterization and reservoir simulation purposes.
- Figure 4d shows a scenario that, although less likely, is within the mapping uncertainty. In this scenario, the Mendota_INJ_1 well intersects the distal deltaic shelf deposits.

The Mendota_INJ_1 well location may intersect several different depositional systems as explained above and in Figure 4b–4d. These series of diagrams demonstrate possible depositional environments that Mendota_INJ_1 could encounter, but are conceptual, and not representations of well construction design.

If the Mendota_INJ_1 well location is in the submarine fan sandstones (Figure 4b), which is the likely scenario based on the interpretation of the data, then there is a much greater chance of an updip stratigraphic pinchout into Moreno shales, providing an additional lateral seal for injected CO₂ to the northeast. However, in this scenario there is still a chance that these distal sandstones connect updip through sand-filled channels to the deltaic Starkey deposits. Because of these depositional uncertainties and to take a conservative approach to AoR estimation, the geomodel used in site characterization and dynamic modeling considered connected sandstones (Figure 4c).

Updip lateral constraints to reservoir continuity, shown stratigraphically in Figure 4, can also include faults. Approximately 6 miles updip to the east from the proposed injection well at the Mendota site are two known faults (USGS, 2019a) located in the Gill Ranch gas storage field as discussed further in Section 2.3.1. Interpretation from limited 2D seismic data across the study area also shows minor structural deformation where any incoherency in the data was interpreted for this study as a possible fault. This interpretation has a high degree of uncertainty because of poor seismic quality, but the lack of clear fault offset suggests that large throw faults are not common, and lateral structural controls limiting updip CO₂ migration is unlikely.

Figure 5 is a site-specific stratigraphic column and synthetic porosity log for Mendota_INJ_1 derived from nearby subsurface wells that shows the Cretaceous Panoche reservoir section overlain by the Late Cretaceous Moreno shale. The Panoche formation is separated into specific sandstone intervals separated by shale layers and labeled First, Second, Third, and Fourth Panoche from youngest to oldest. Injection and confinement zones under consideration for the Mendota_INJ_1 well include the Cretaceous First and Second Panoche sandstones and their associated intraformational shale formations at a depth of 8,000 to 12,000 ft below ground surface (BGS), with the overlying Moreno shale at 7,000 to 8,000 ft BGS providing a regional seal.

Figure 6 summarizes the primary formations of interest at the Mendota site and their intended use in this project.

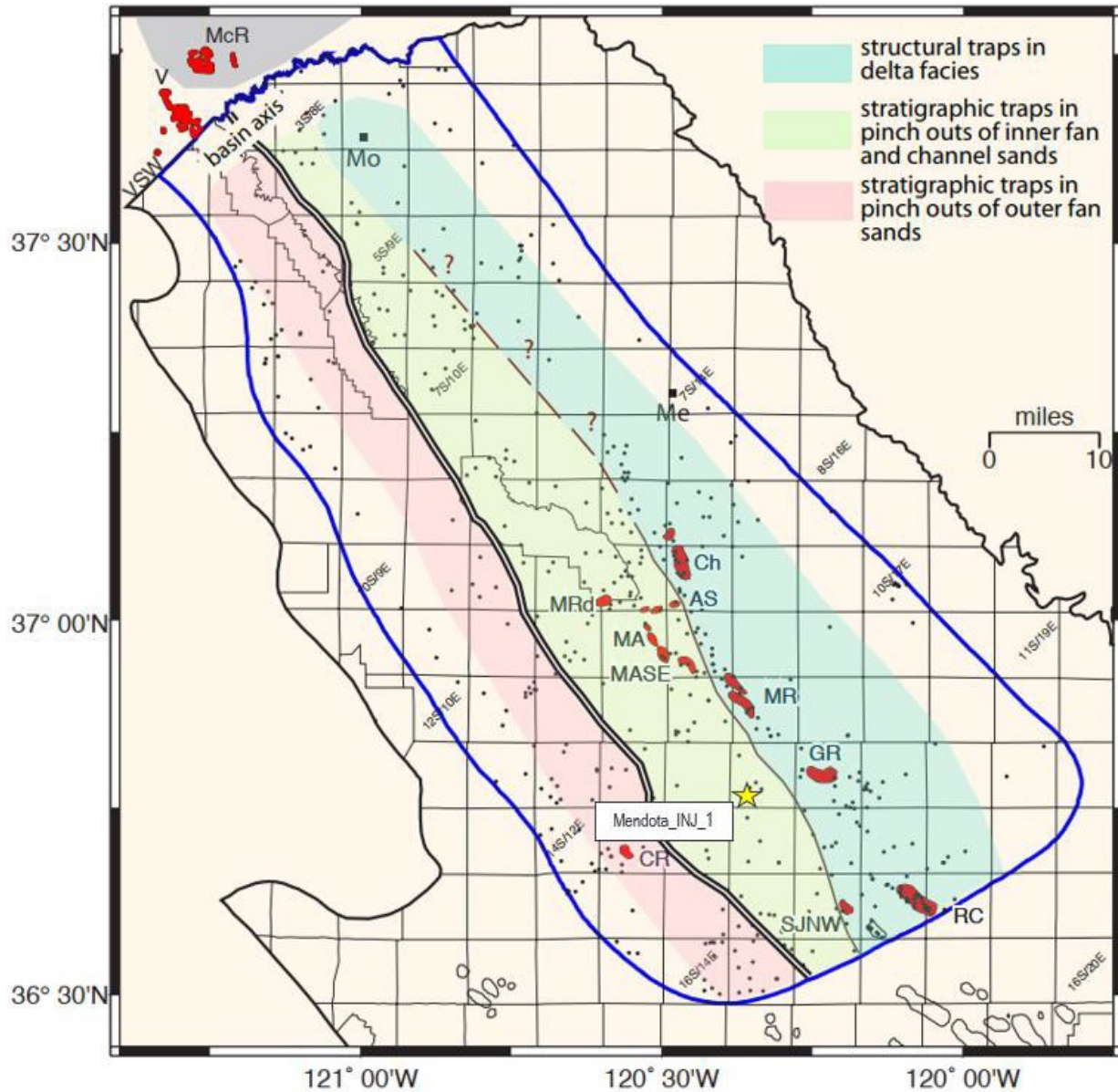
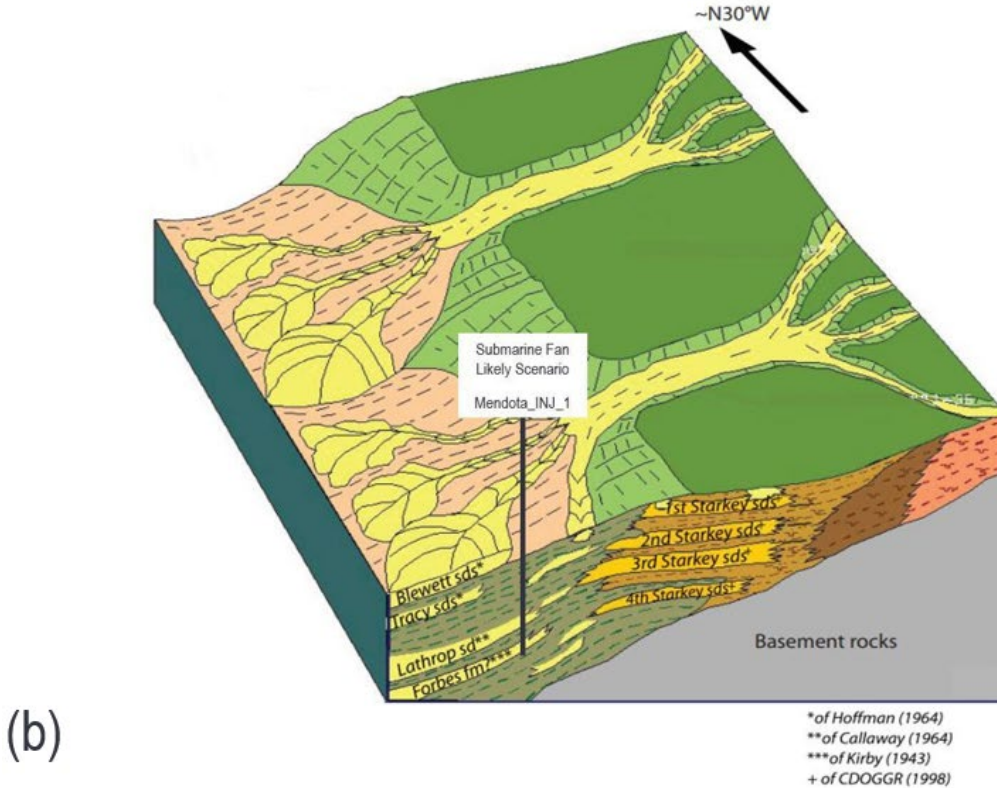
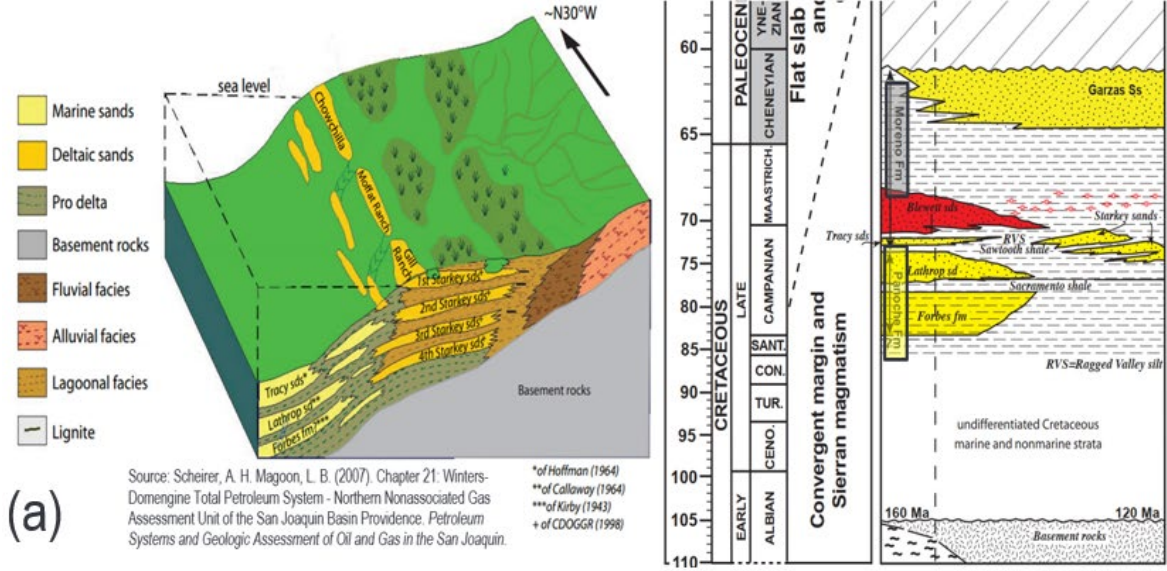
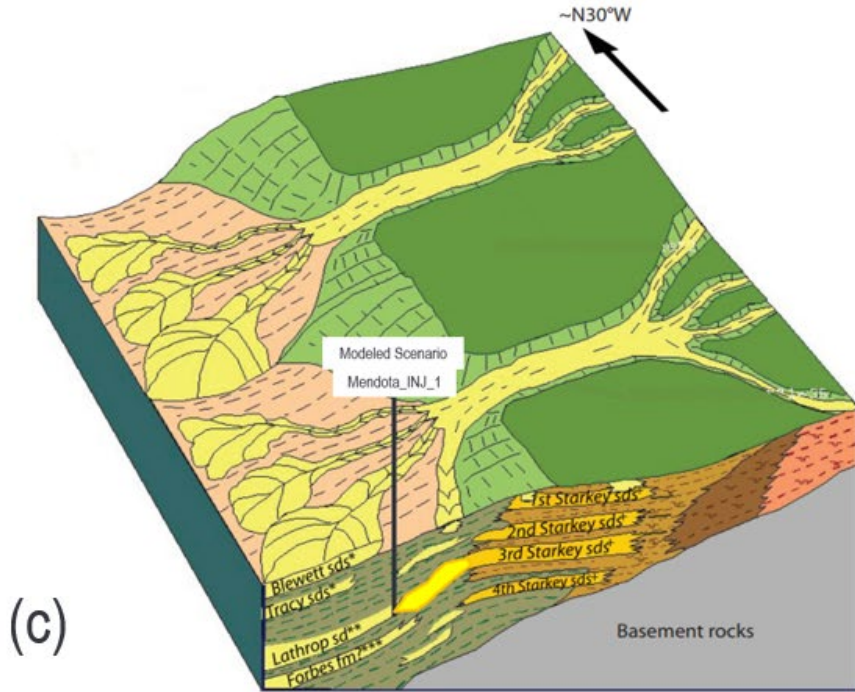
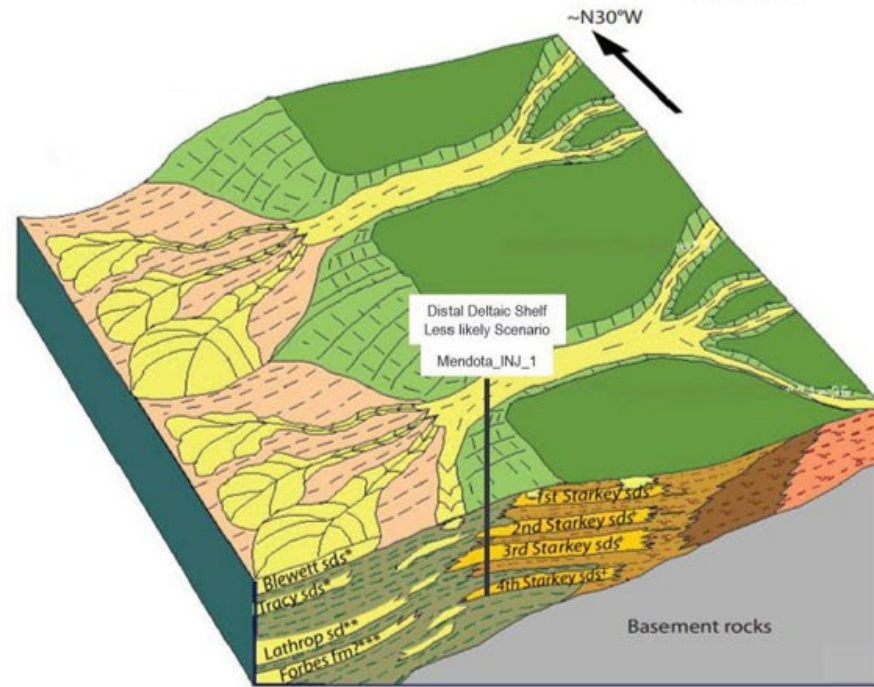


Figure 3. San Joaquin basin depositional model showing structural and stratigraphic traps. The yellow star indicates the proposed Mendota_INJ_1 location. GR, Gill Ranch. CR, Cheney Ranch (Hosford Scheirer & Magoon, 2007b).





*of Hoffman (1964)
 **of Callaway (1964)
 ***of Kirby (1943)
 + of CDOGGR (1998)



*of Hoffman (1964)
 **of Callaway (1964)
 ***of Kirby (1943)
 + of CDOGGR (1998)

Figure 4a-d. San Joaquin basin depositional model showing possible depositional scenarios for the location of Mendota_INJ_1; modified from Hosford Scheirer and Magoon (2007b).

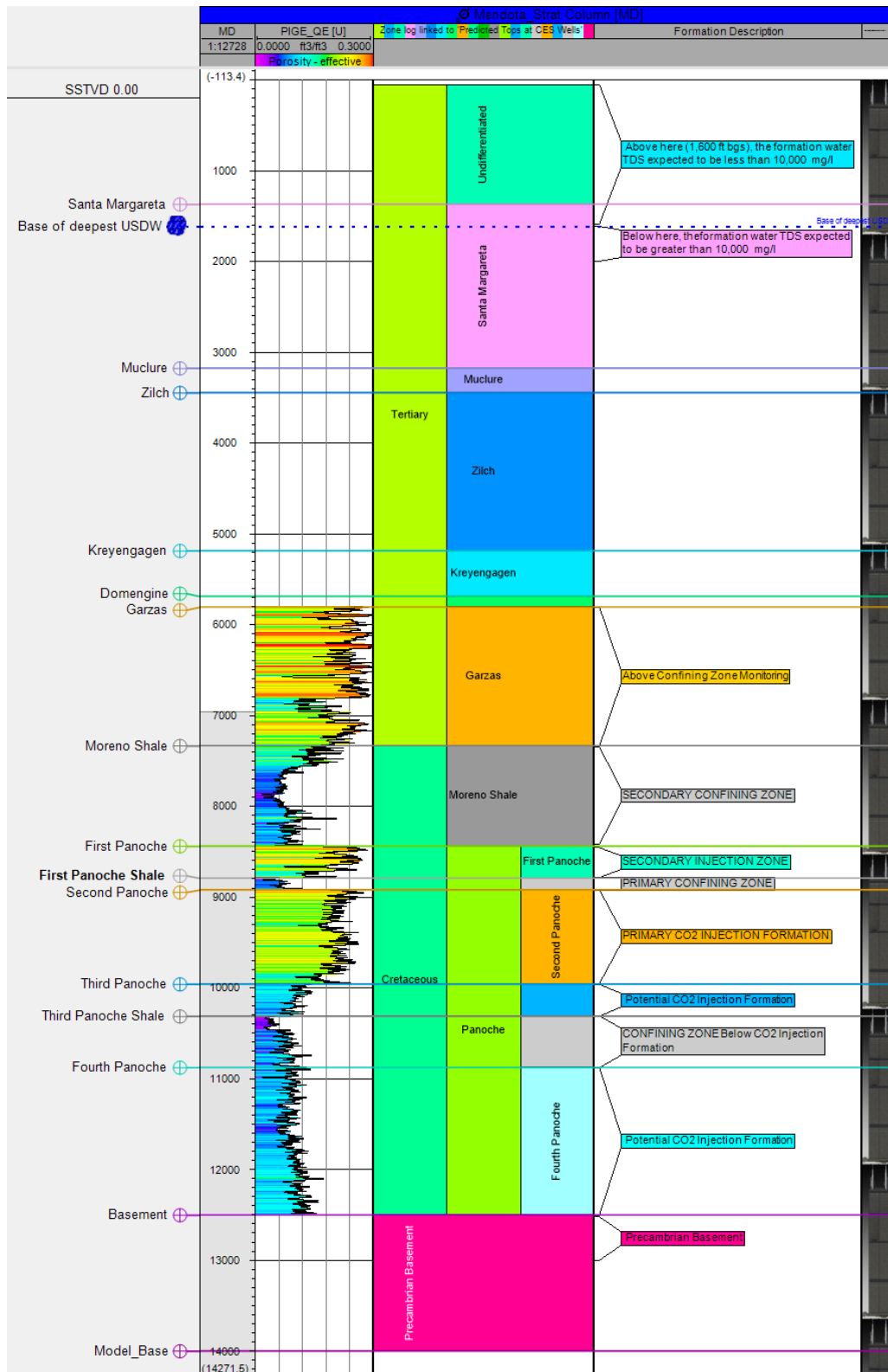


Figure 5. Mendota stratigraphic column and effective porosity log. Right-most track shows the Sears (Willis) tower for scale.

Primary Formations of Interest	Formation Description and Intended Use
Garzas Sandstone	The Garzas sandstone member of the Moreno formation represents a major deltaic complex and overlies the Moreno shale. This zone will be monitored for above-confining-zone migration of CO ₂ .
Moreno Shale (Well correlation includes the Ragged Valley Silt) Secondary Confining Zone	The Moreno shale is an organic-rich marine shale. Because of the Moreno shale's thickness (~1100ft) and because it is regionally extensive, it is intended to provide a seal to ultimately contain any injected CO ₂ that may be migrating up from the underlying First Panoche sandstone.
First Panoche Sandstone Secondary CO ₂ Injection Zone (Permission to inject into this formation is requested)	The First Panoche is intended to be a secondary injection zone to be used if the Second Panoche below is unsuitable for injection or if there is CO ₂ migration that passes up through the below First Panoche shale.
First Panoche Shale Primary Confining Zone	The First Panoche shale is intended to be the primary confining zone that will vertically contain most or possibly all the injected CO ₂ . Because it is relatively thin (127 ft) and because its lateral continuity is unproven, this formation is not being relied upon to contain all the injected CO ₂ . Currently, this formation is interpreted to be continuous within the model domain.
Second Panoche Sandstone Primary CO ₂ Injection Formation (Permission to inject into this formation is requested.)	The Second Panoche sandstones is the primary target for CO ₂ injection.
Third Panoche Sandstone Potential CO ₂ Injection Zone (Permission to inject into this formation is requested)	Although not the target of this project currently, the Third Panoche sandstone may have potential in the future for CO ₂ injection. The lower permeability of this member will likely make this a lower confining zone.
Third Panoche Shale Lower Confining Zone	The shales of the Third Panoche are intended to act as the lowermost confining zone.
Fourth Panoche Sandstone Potential CO₂ Injection Zone	Although not the target of this project currently, the Fourth Panoche sandstone may have potential for future CO ₂ injection.

Figure 6. Primary formations at the Mendota site and their intended use.

2.2 Maps and Cross Sections of the Area of Review (AoR) [40 CFR 146.82(a)(2), 146.82(a)(3)(i)]

2D seismic and well data, including tops, logs, and core, were assembled from various sources to assess the feasibility of geological sequestration at the Mendota site. Using these data, structural maps and cross sections were generated in the Petrel* E&P software platform encompassing the AoR. Figure 7 and Figure 8 show that in this part of the San Joaquin basin, the subsurface dip is approximately 4° to the SW, with the closest known faults 6 miles updip to the east. The lowermost underground source of drinking water (USDW) is estimated around 1,600 ft BGS (Section 2.7.1). The proposed injection targets, the First and Second Panoche sands, are estimated to be at depths of 8,437 ft and 8,918 ft BGS, respectively, with the overlying Moreno shale estimated at 7,332 ft at Mendota_INJ_1 (Figure 5).

Well and 2D seismic data show the Panoche sand targets are continuous through the model domain. Wells used for geological top interpretation and petrophysics are shown in Figure 9 and will be discussed further in Section 2.4.2. The log sections in Figure 10, Figure 11, and Figure 12) show that the target sands and confining shales appear continuous and laterally extensive; however, the extents are uncertain because of the current lack of available seismic and well data. Published interpretations indicate that the Maastrichtian-age sand and shale submarine fan facies vary in thickness and lateral extent (Suchsland & Peters, 1997; Bartow & Nilsen, 1990; Hosford Scheirer & Magoon, 2007b) (see also Section 2.1), and as more data become available after acquisition of 3D seismic and a characterization well is drilled, the extents and thickness of injection and confining zones will be reassessed. Formation surface maps and formation thickness maps from the current data and interpretations are presented in Figure 13 and Figure 14. These maps incorporate the 2D seismic and fault interpretation discussed below in Section 2.3.

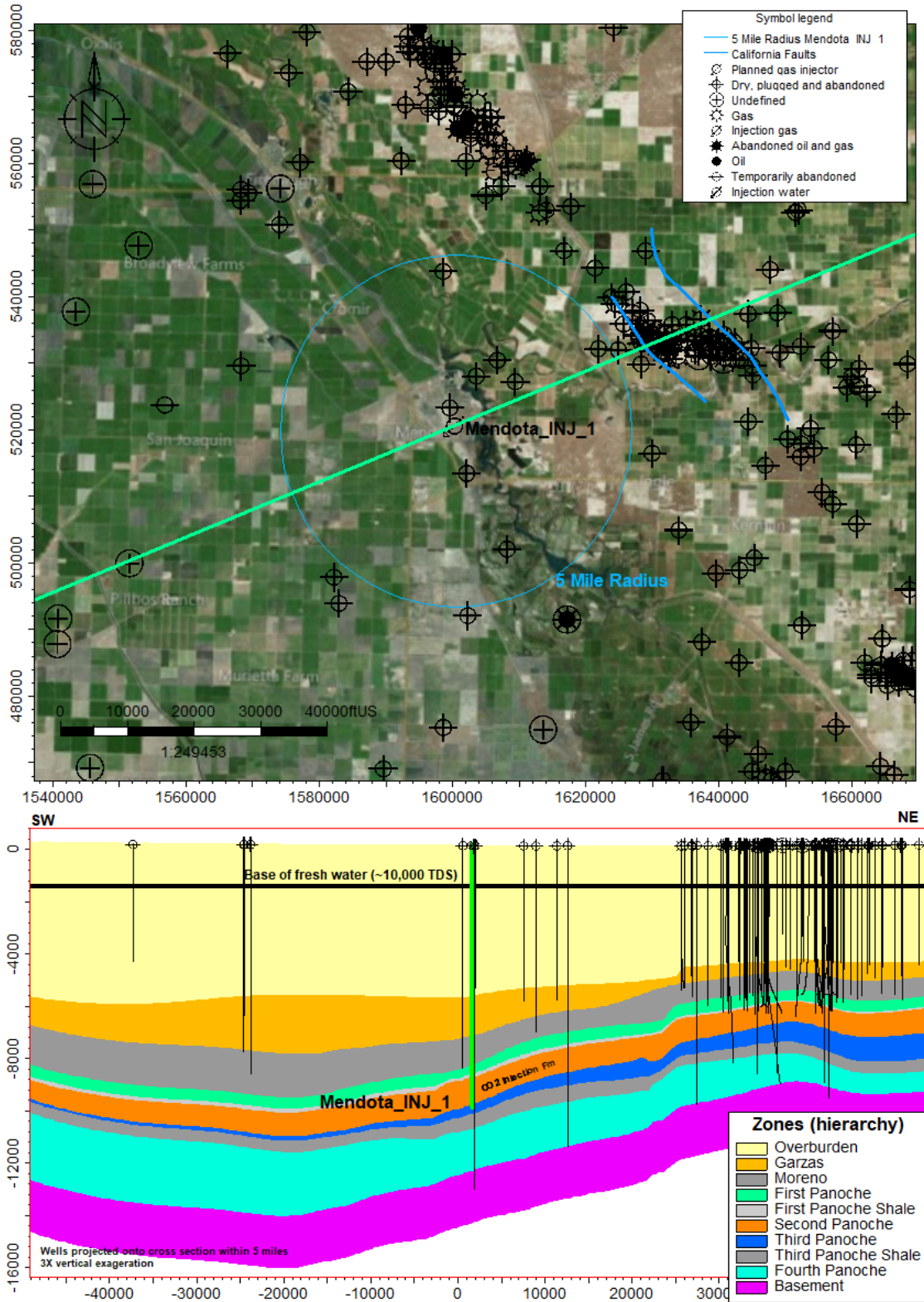


Figure 7. Subsurface geology and legacy wells surrounding the Mendota site, SW-NE cross section.

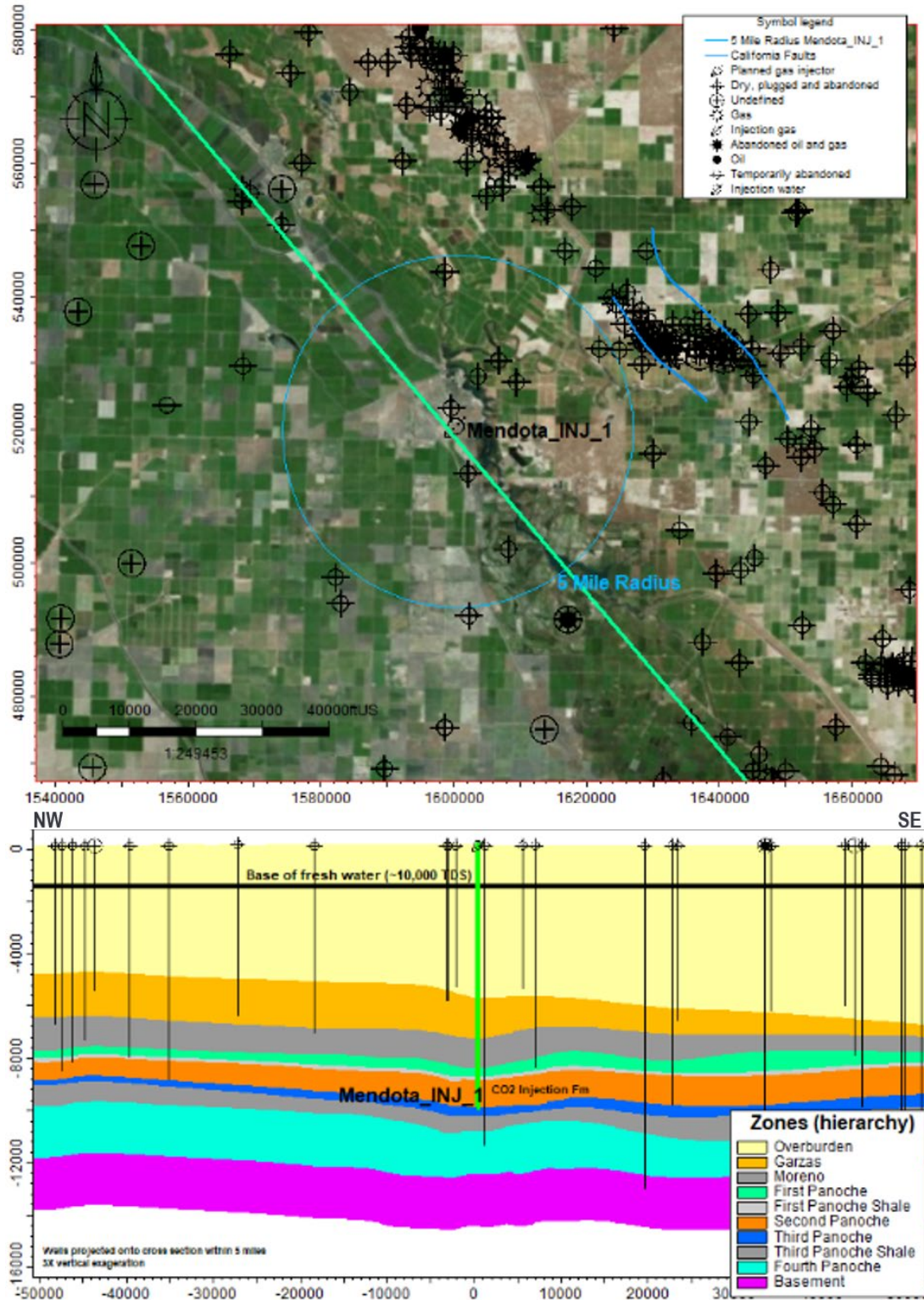


Figure 8. Subsurface geology and legacy wells surrounding the Mendota site, NW-SE cross section.

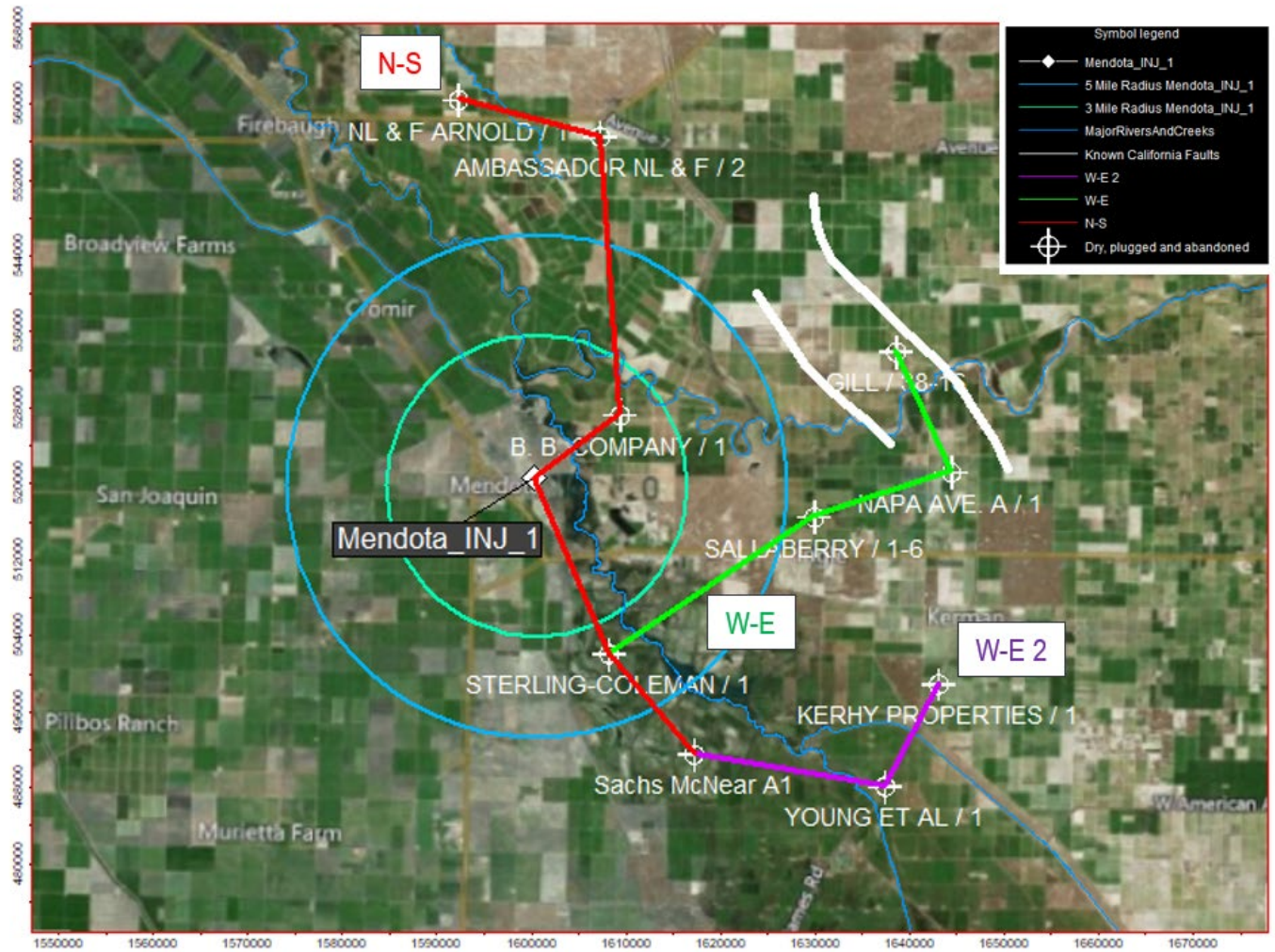


Figure 9. Ten wells used in petrophysical analysis and well correlation, showing the locations of cross sections N-S, W-E, and W-E 2, shown in Figure 10, Figure 11, and Figure 12, respectively.

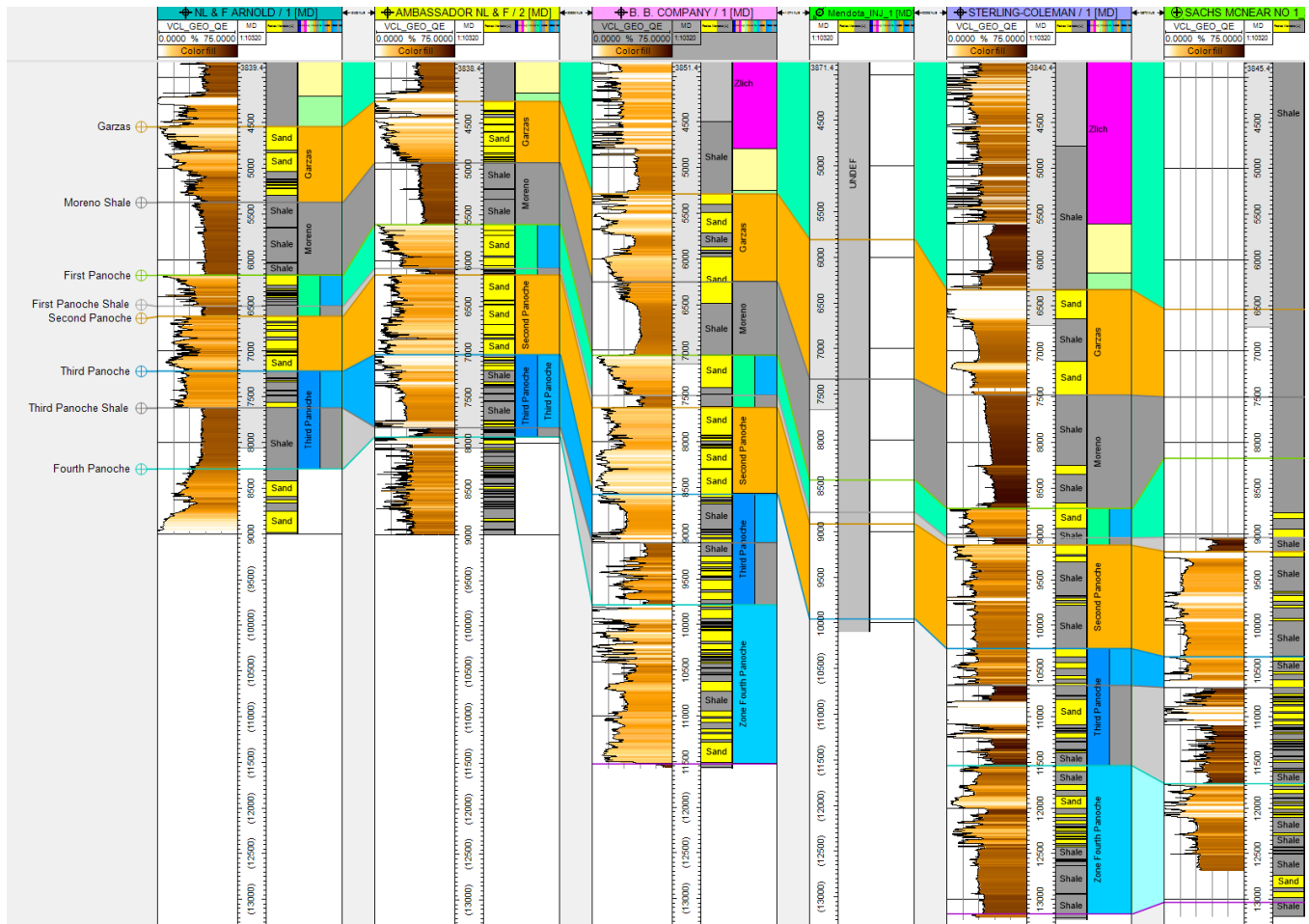


Figure 10. N-S cross section (location shown in Figure 9) which shows 5 out of 10 petrophysical wells used in analysis of injection and confining rock properties. The Mendota_INJ_1 is located between B. B. Company 1 and Sterling-Coleman 1 wells. Tracks left to right are volume of clay (VCL), measured depth, zone log, facies calculated from VCL, and zone color fill between wells.

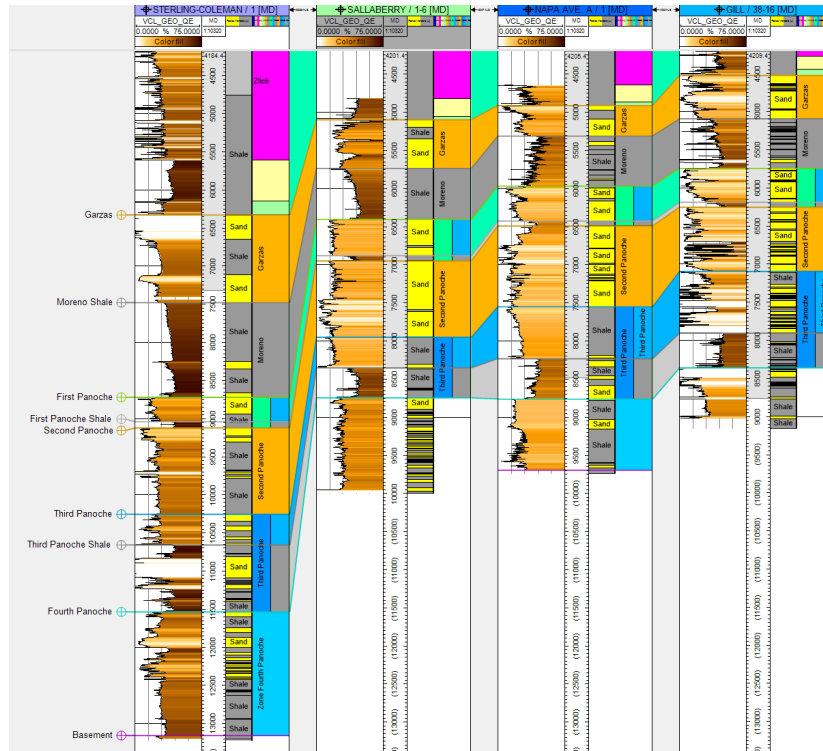


Figure 11. W-E cross section (location shown in Figure 9). Tracks left to right are VCL, MD, zone log, facies calculated from VCL, and zone color fill between wells.

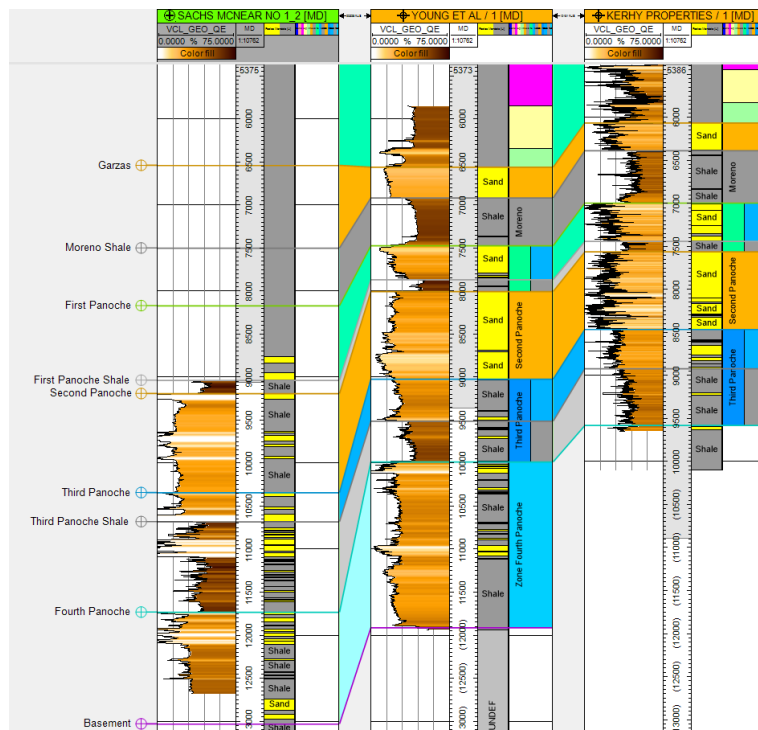


Figure 12. W-E 2 cross section (location shown in Figure 9). Tracks left to right are VCL, MD, zone log, facies calculated VCL, and zone color fill between wells.

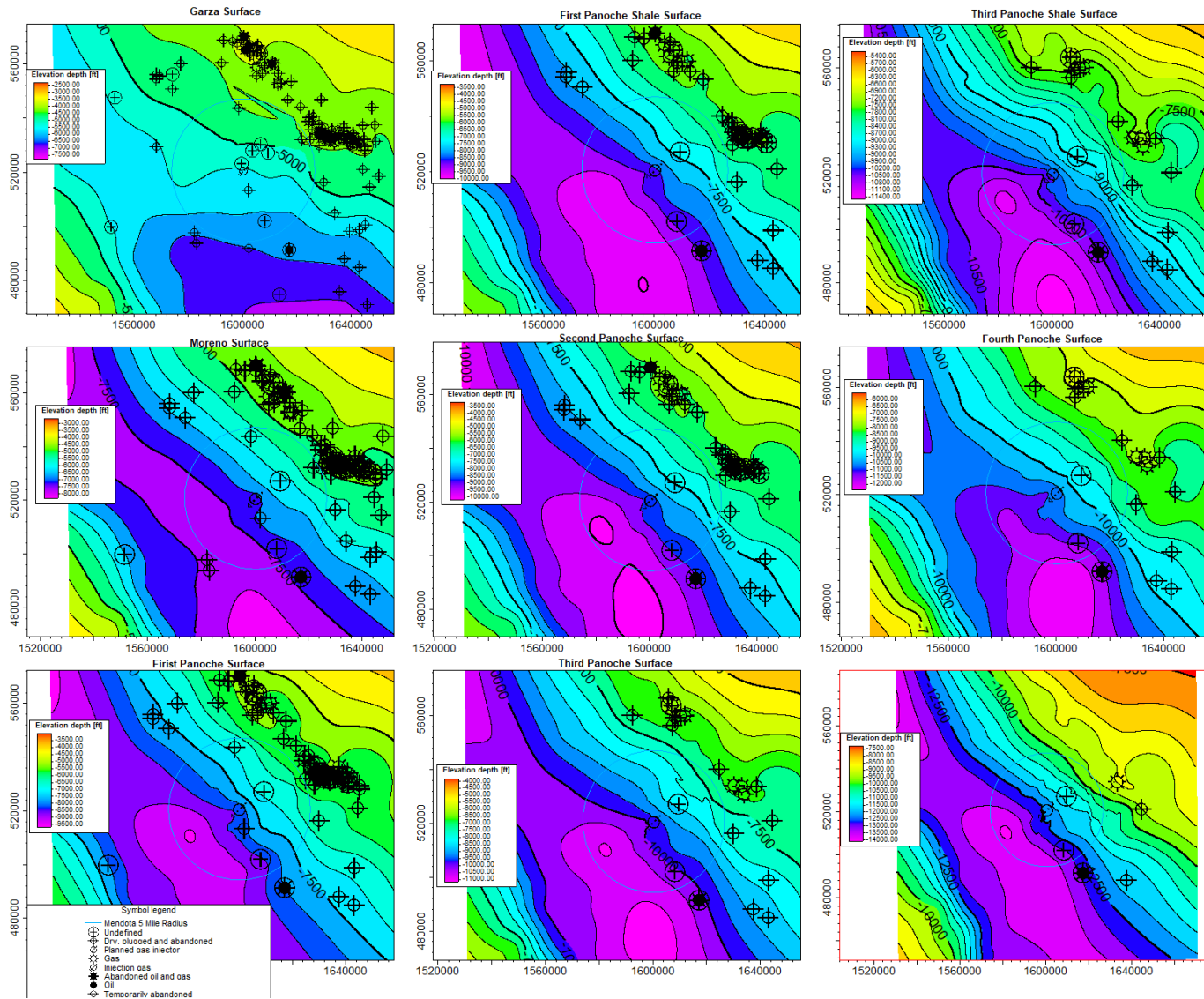


Figure 13. Formation surface maps generated from well tops and seismic data; well symbols indicate wells that are estimated to penetrate the mapped formation.

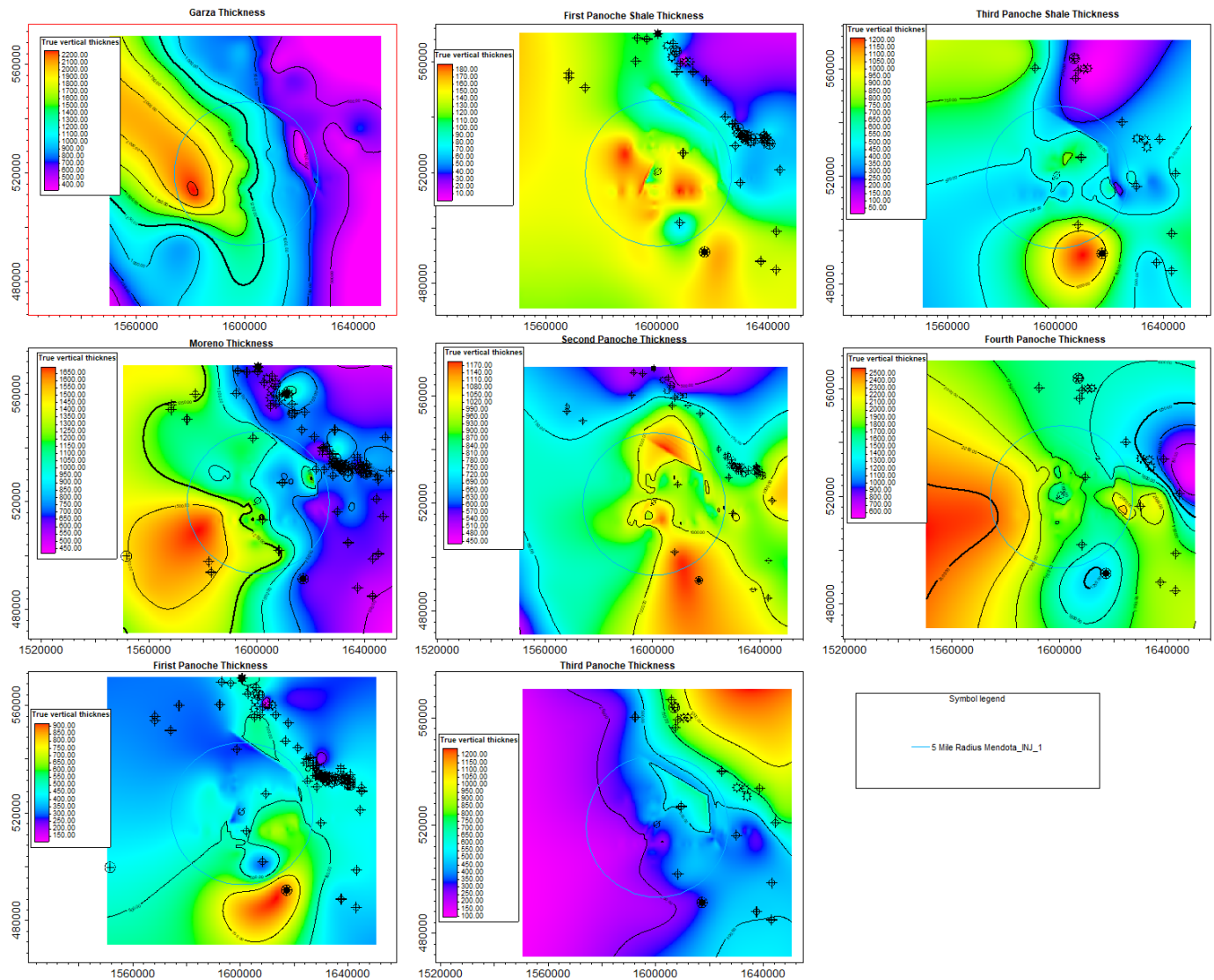


Figure 14. Formation isochore maps.

2.3 Faults and Fractures [40 CFR 146.82(a)(3)(ii)]

2.3.1 Geophysical Workflow

To evaluate faulting regionally and locally, fault data were gathered from public sources (USGS, 2019c) and interpreted locally across three 2D seismic lines that encompass the AoR (SEI, 2019) (Figure 15). Faults were interpreted in the time domain across the 2D seismic lines and converted to depth using a regional velocity model derived from synthetic seismic-well ties, horizon interpretations, and well formation tops. Well tie analysis was completed to calculate the time-depth relationship between 2D seismic interpretations in time and well tops interpreted in depth. In Figure 15, the light blue lines trending NW-SE represent surface faulting identified by the USGS (<https://mrdata.usgs.gov/geology/state/map-us.html>). The subsurface locations and names

of these faults are currently unknown. Field pool data from Gill Ranch estimates the western fault dips east and the eastern fault is near vertical. The Sallaberry 1-6 well was used to complete the seismic-well tie analysis, which is shown in Figure 16. The depth-converted seismic lines with horizon and fault interpretations are shown in Figure 17, Figure 18, and Figure 19.

A 3D perspective view in Figure 20 provides an overview of the interpreted faults. Most of the interpreted faults have small throws and are not interpreted between the 2D seismic lines. One exception is the two northerly trending faults that separate the Gill Ranch field from the Mendota AoR nearly 4 miles east of the proposed Mendota_INJ_1. These faults are labeled in Figure 17 as Fault 1 and Fault 2 near shotpoint 1650 and in Figure 20 are associated with a step shown on the basement surface. Also, Fault 1 is projected northwest in Figure 20 parallel to the faults shown in the legacy Gill Ranch field Second Panoche structure map; however, sufficient control is missing for accurate positioning of this fault. A few minor faults are projected in 3D, but most are small and cannot be connected between the seismic lines. Two additional normal faults, Faults 3 and 4, are interpreted deeper in the Panoche formation near the proposed injection well as shown on 2D seismic line W-SJ-209 (Figure 18). These normal faults are subtle, have small displacement, and do not appear to extend above the Third Panoche.

The seismic interpretations, minus these small offset faults, provided the structural framework, which was calibrated in depth to geologic formation tops and integrated into the geologic model shown in Figure 21. Fault 13 as described below was included in the geocellular model but not in the dynamic simulation; fault seal analysis was applied to this single fault to show the expected impact on cross-fault flow (Section 2.3.2).

The preliminary fault interpretation of the 2D seismic data includes a low-angle fault, Fault 13 (Figure 20) with an approximate 30° dip to the SE below the planned Mendota_INJ_1. On Figure 18, Fault 13 is projected onto a 2D seismic line. The image quality is poor possibly because of “out of plane” interference reducing the confidence in the interpretation. The trace of the Fault 13 is interpreted with greater confidence with the better imaging on the E-W seismic lines W-SJ-202 and W-SJ-013W (Figure 17 and Figure 19). Fault 13 has minimal offset and is interpreted to terminate at the base of the Moreno shale without reaching the shallower Garzas horizon. Publicly available fault movement maps show no evidence of historical movement of this fault (California Geological Survey, 2010). The fault is unlikely to provide a CO₂ migration pathway through the Moreno shale as mapped terminating at the base of the shale. The modeled plume migration is updip in the NE direction (Schlumberger, 2021b) away from Fault 13.

This dip orientation of Fault 13 is consistent with a thrust, but it is nearly perpendicular to the regional maximum horizontal principal stress direction of ~N45E from the world stress map, which is inconsistent. Assuming the fault geometry is correct, then Fault 13 would have formed with the present-day maximum horizontal stress direction as a minimum horizontal stress direction in a thrust tectonic regime. Rotation of stress direction locally and regionally is possible over time, and the fault may have developed at an earlier time due to a rotation of the stress. Alternatively, 3D seismic data may provide an alternative interpretation of the fault more consistent with the present-day regional stress. Regardless of the origin of Fault 13, its orientation and position based on current mapping is below Mendota_INJ_1 at a depth of 9,850 TVDSS. The Mendota_INJ_1 well injection target is the Second Panoche sand interval, which is shallower (9,718 to 9,757 TVDSS) than the interpreted Fault 13.

2.3.2 Fault Seal Analysis

Fault 13 was incorporated into a geocellular model to analyze zonal facies juxtaposition and to conduct shale gouge ratio (SGR) fault seal analysis. Preliminary analysis of fault seal clay content distribution was completed using a VCL modeled grid property derived from petrophysical analysis (discussed in Section 2.4.2) from wells and extrapolated through the model using a facies model for bias. Using the VCL modeled property, fault seal facies juxtaposition and SGR were calculated (Figure 22). Facies juxtaposition analysis shows areas of reservoir juxtaposed against reservoir or against shales to assess the cross-fault flow behavior and risks to confinement of injected CO₂. If displacement across the fault is high, then an injection target could be juxtaposed against a shallower sand facies posing leakage risk to another zone or the juxtaposition can create a seal with the reservoir juxtaposed against a shale such as the caprock. Figure 23 illustrates the difference between low and high fault displacement. Based on interpretation of Fault 13 across all three seismic lines (Figure 17, Figure 18, and Figure 19), it is likely that displacement is low, indicating that the right illustration of Figure 23 is most likely with much of the reservoir self-juxtaposed.

Clay distribution along the fault from a mixing of the protolith cut by the fault could provide a seal. To assess this risk, fault clay content was calculated across Fault 13 from a SGR algorithm, which is a function of the VCL grid property and the fault throw (Yielding, Freeman, & Needham, 1997) (Yielding, 2002). The results of this analysis (Figure 22) are consistent with the low throw across the fault. In areas with high clay content across the fault, such as the shales, little to no cross-fault flow is expected. The reservoir section cut by the fault, however, has a distribution of low and moderate clay content, which is a function of clay-rich areas in the facies distribution. This would suggest the fault may act as a baffle but is unlikely to act as a seal to the CO₂ cross-fault flow. A risk of upwards migration of CO₂ along Fault 13 is still possible but limited by the fault height in the section below the Moreno caprock. Without additional data, there is insufficient information currently to quantify the transmissibility of CO₂ across Fault 13.

2.3.3 Uncertainty, Additional Data, and Analysis

Uncertainty regarding the extent of fracturing and faulting within the AoR includes elements of seismic imaging, depth calibration and availability of deep well control and physical measurements (well logs) near the proposed site. In future phases of this project, 3D seismic data and core and image logs from a characterization well can be used for discrete fracture modeling to determine the intensity of fractures and provide more precise mapping and clearer understanding of the faulting complexity and connectivity. Fractures, however, are unlikely to play a role in these porous reservoirs and are more likely a risk in the integrity of the caprock.

Due to poor imaging and the wide distance between seismic lines and limited number of seismic lines, the exact location of faults, such as the longer Fault 13, for example, is uncertain. A more comprehensive analysis of faults and potential associated risks will be performed after additional site-specific data are collected. A 3D geomechanical model using well logs, geomechanical core analysis, and well test data combined with 3D seismic data will provide better characterization of the in-situ stress field, pore pressure and rock strength, for a fault stability analysis and sealing

capacity of these faults (Chiaramonte, Zoback, Friedmann, & Stamp, 2008). The final location of the injection and monitoring wells will consider all identified faults to mitigate any risk of interaction with the pressure AoR based on the updated AoR delineation and geomechanical models.

The plan for the 3D seismic survey is that it will contain full-fold and maximized azimuth distribution over the modeled area of the plume after 20 years of injection. The fold and azimuthal distribution will taper away from the plume edge.

The objectives of the planned 3D survey and other pre-operational structural work are the following:

- Validate the position of Fault 1 via 3D seismic data.
3D seismic will be acquired to better define the geometry of all faults within the plume area.
- Validate the nature of the displacement of Fault 13.
By combining the 3D seismic data interpretation with a geomechanical model calibrated to core and well test data, the dynamic mechanical stability and displacement along the fault can be determined either through analytical or numerical stress analysis. Since there is uncertainty associated with the current location of the faults interpreted on the 2D seismic lines - (especially Fault 13, which is interpreted on the E-W seismic lines, but not evident on the seismic line closest to the well), the 3D seismic interpretation will improve the position and relative displacement of the faults.
- Collect core data to demonstrate the sealing capacity of Fault 13.
Core data will be collected from the monitor and injection well locations.

The location of Fault 13 is uncertain and possibly may not even exist (because of the nature of interpreting on 2D seismic and the distance between the 2D seismic lines). Also, the injection well, as currently planned, stops several hundred feet above the interpreted fault. Therefore, the well does not intersect the interpretation for Fault 13. Since the injection well stops above the interpreted Fault 13, no core data can be collected across the location of Fault 13. The core analysis results will validate the geomechanical model, which will facilitate a more reliable assessment of the fault stability.

- Perform 3D geomechanical modeling based on data collected via well logs, geomechanical core analysis, and well testing, combined with 3D seismic data to better characterize the faults in the area and determine their sealing capacity and that they are nontransmissive.

3D seismic data will be acquired to enhance the fault geometry throughout the area. The same methodology referred to above in determining the displacement of Fault 13 will be applied to the faults in the survey area. The improved interpretation of the fault and horizon data and the integration of the well data will better constrain the analysis of any cross-fault transmissivity and associated risks.

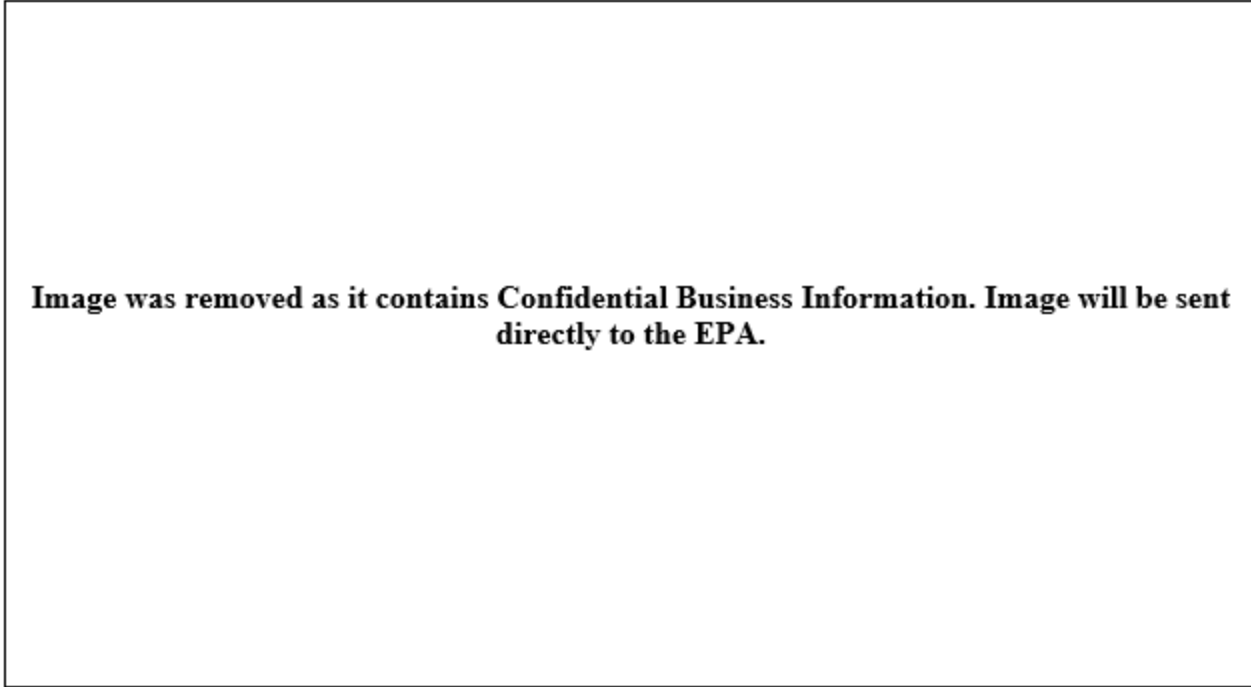


Figure 15. CONFIDENTIAL BUSINESS INFORMATION: 2D seismic line map, shotpoints, and area wells showing the 3 and 5-mile radii from Mendota plant site. The light blue lines over the Gill Ranch gas field are faults. This image displays data from SEI (2019), and it is marked as Confidential Business Information.

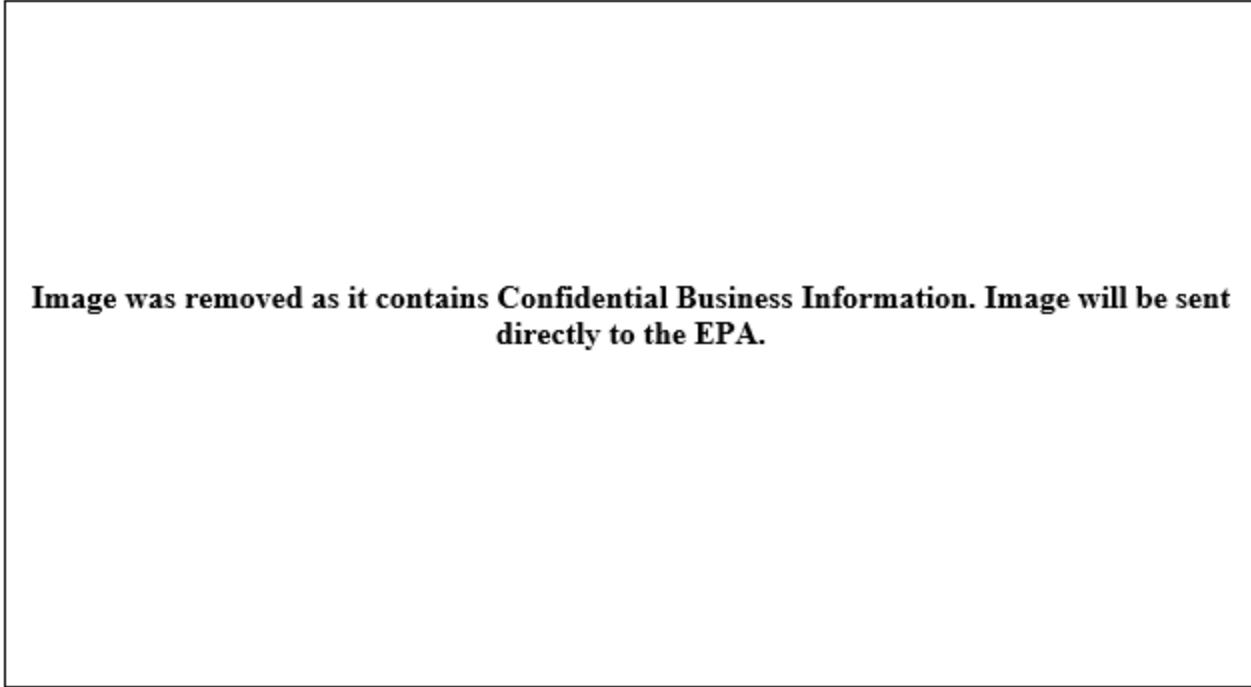


Figure 16. CONFIDENTIAL BUSINESS INFORMATION: Seismic well tie: line W-SJ-202 and Sallaberry 1-6 well (API number 4019215350000). This image displays SEI data (2019), and it is marked as Confidential Business Information.

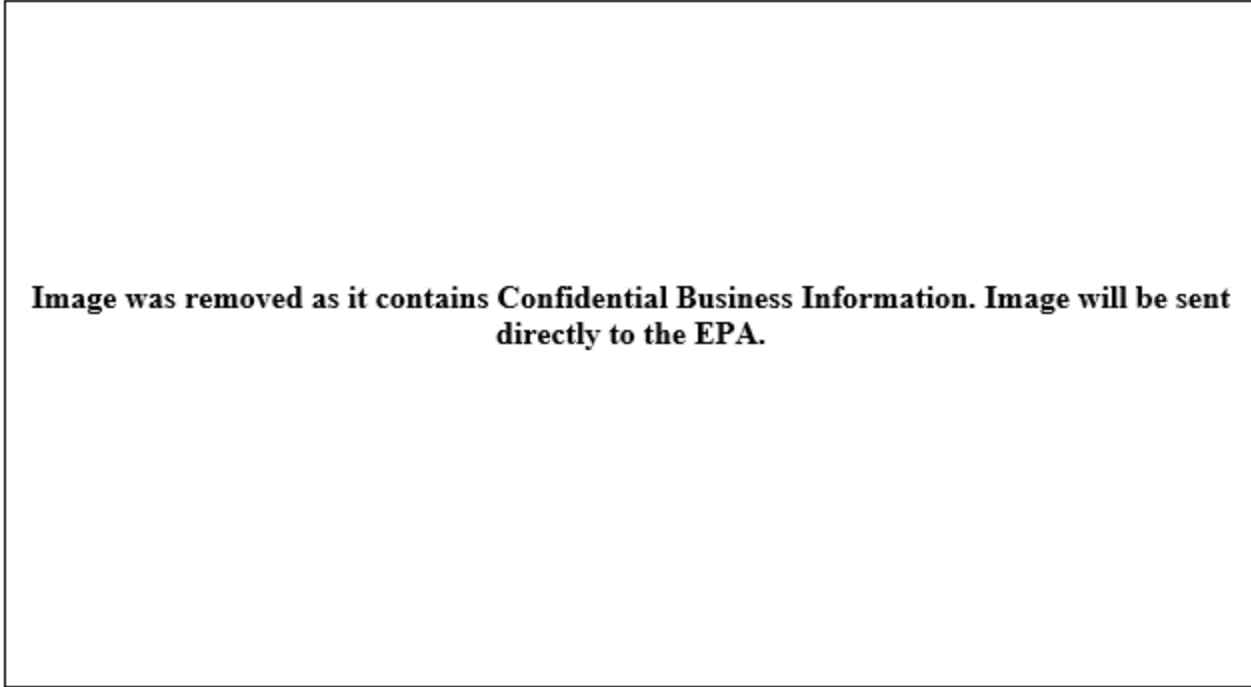


Figure 17. CONFIDENTIAL BUSINESS INFORMATION: W-SJ-202 2D seismic line (depth) with interpreted horizons and faults. This image displays SEI data (2019), and it is marked as Confidential Business Information.

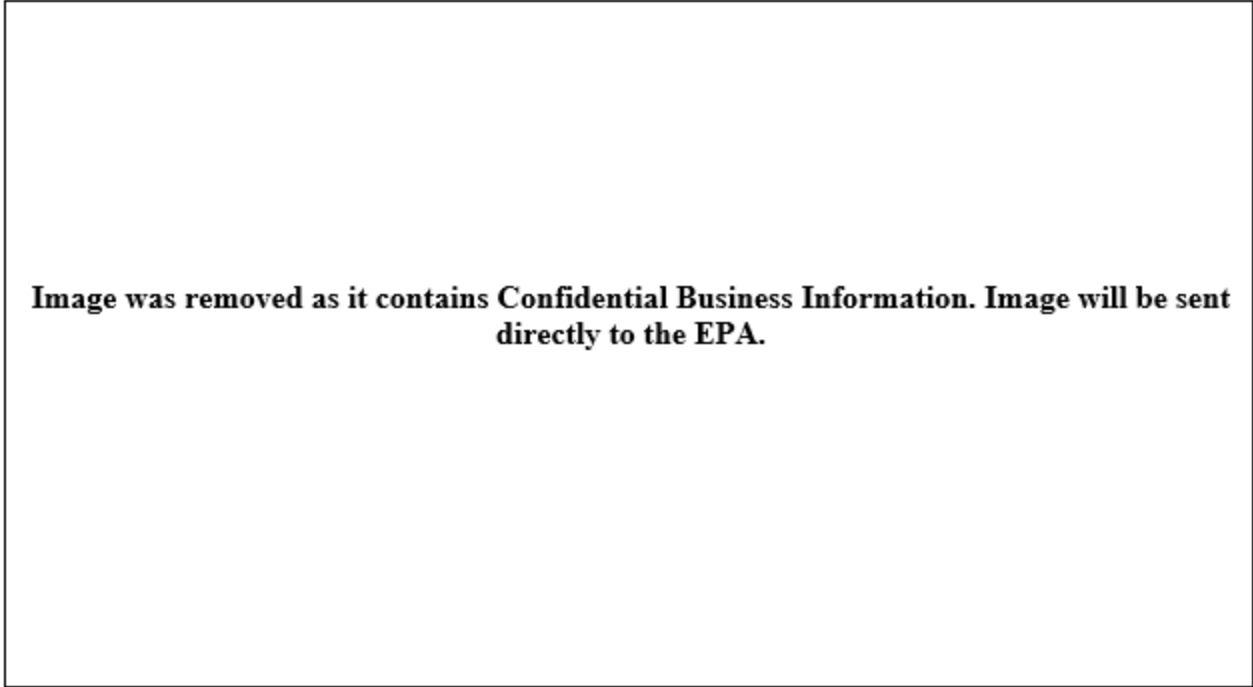


Figure 18. CONFIDENTIAL BUSINESS INFORMATION: W-SJ-209 2D seismic line (depth) with interpreted horizons and faults. This image displays SEI data (2019), and it is marked as Confidential Business Information.

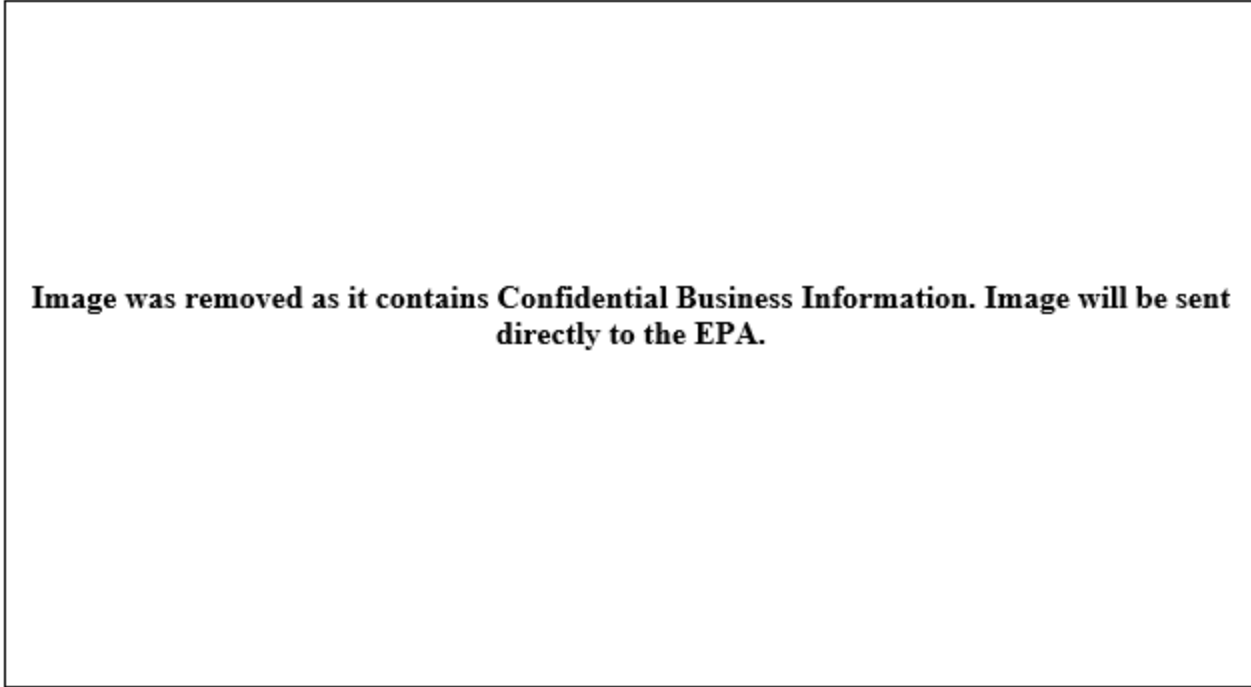


Figure 19. CONFIDENTIAL BUSINESS INFORMATION: W-SJ-013W 2D seismic line (in depth) with interpreted horizons and faults. This image displays SEI data (2019), and it is marked as Confidential Business Information.

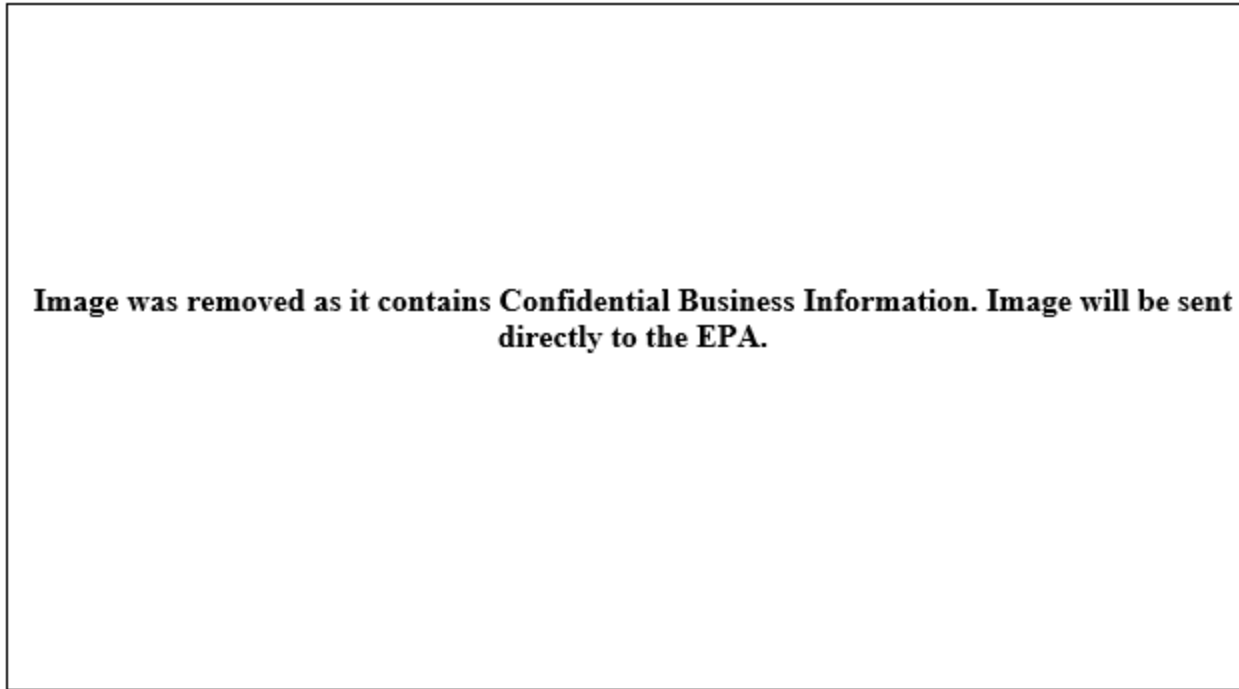


Figure 20. CONFIDENTIAL BUSINESS INFORMATION: 3D view (facing SE) of interpreted faults on the 2D seismic lines and basement surface. Dotted lines are projected faults (color coded by horizon) or projected fault plane. A legacy Gill Ranch field structure map is inserted at the Second Panoche. This image displays SEI data (2019), and it is marked as Confidential Business Information.

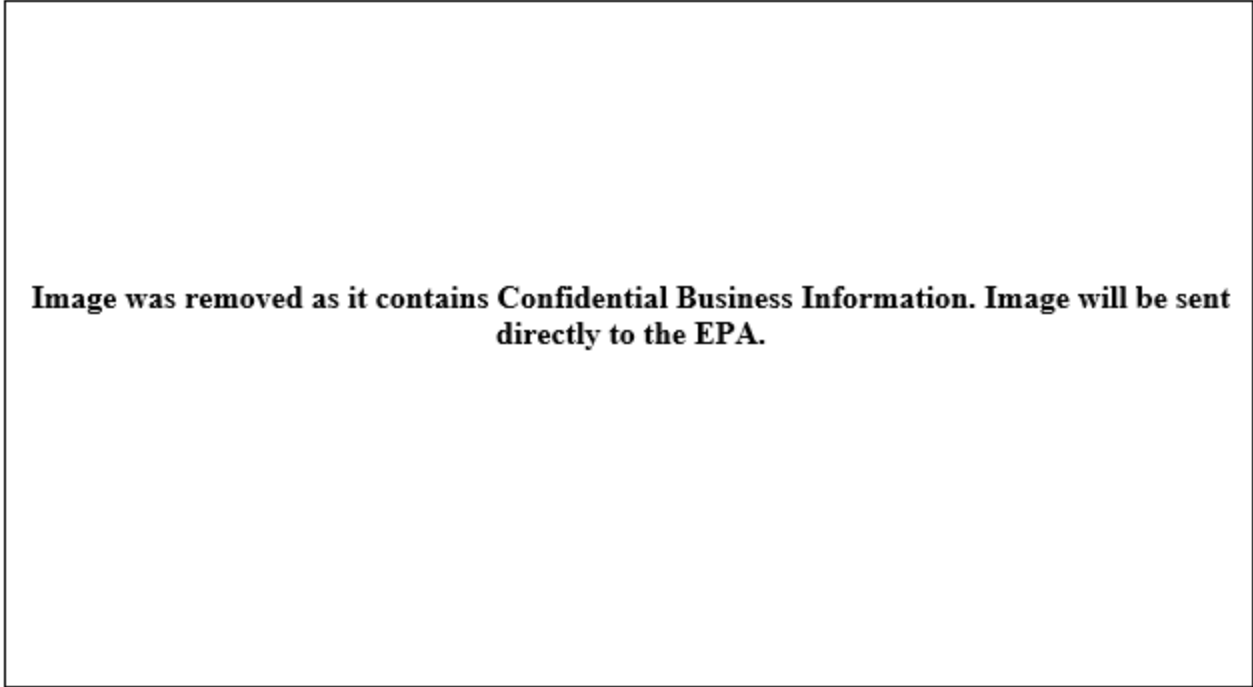


Figure 21. CONFIDENTIAL BUSINESS INFORMATION: 3D perspective of the depth-integrated geophysical model. This image displays SEI data (2019), and it is marked as Confidential Business Information.

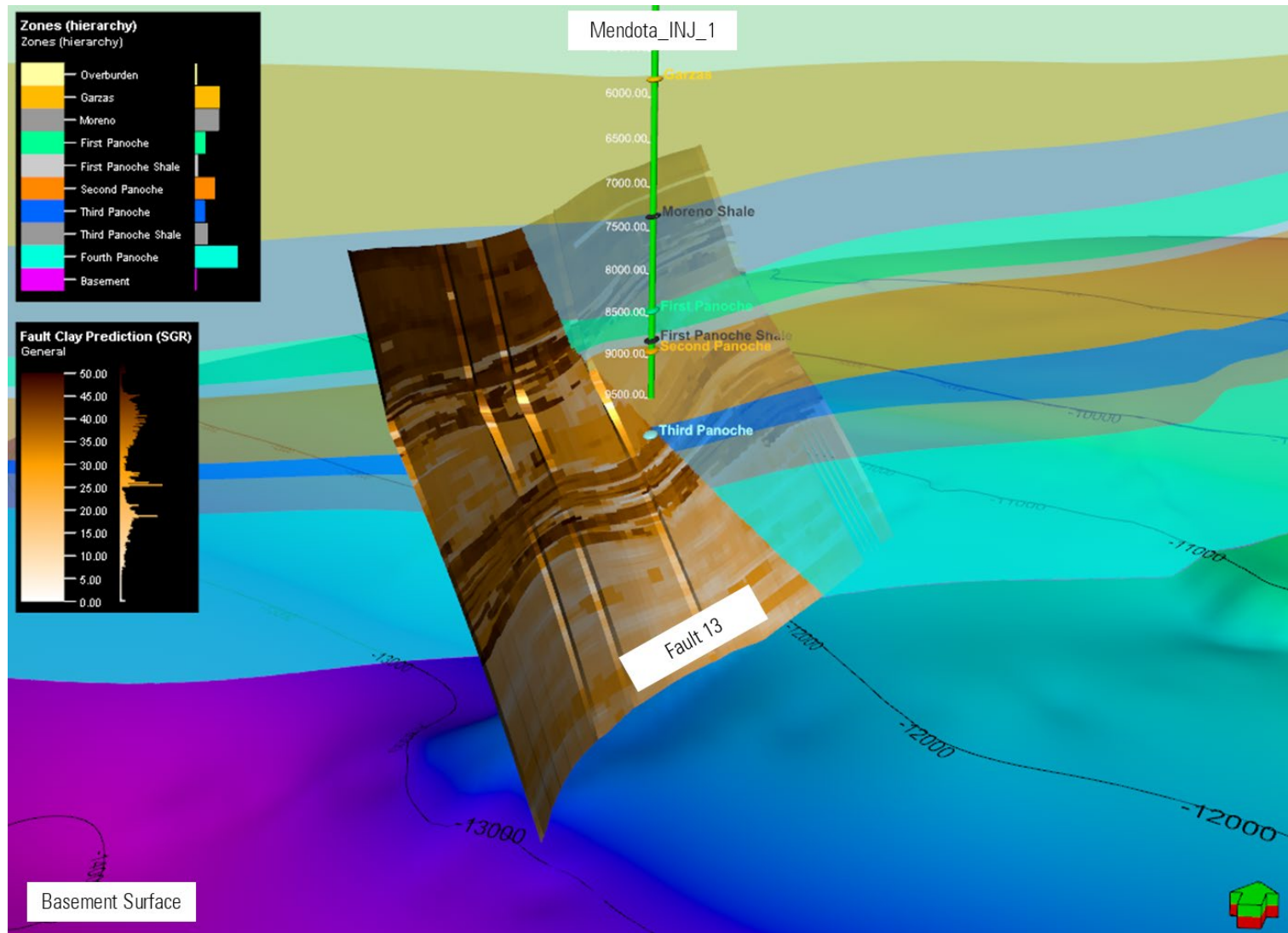


Figure 22. Fault 13 terminates within the Moreno shale. The Mendota_INJ_1 wellbore, which targets the Second Panoche injection sand, is shown in green with MD annotated in white text. Fault 13 is colored by fault clay prediction content based on the SGR algorithm, the results of which indicate the Moreno shale smearing along the fault.

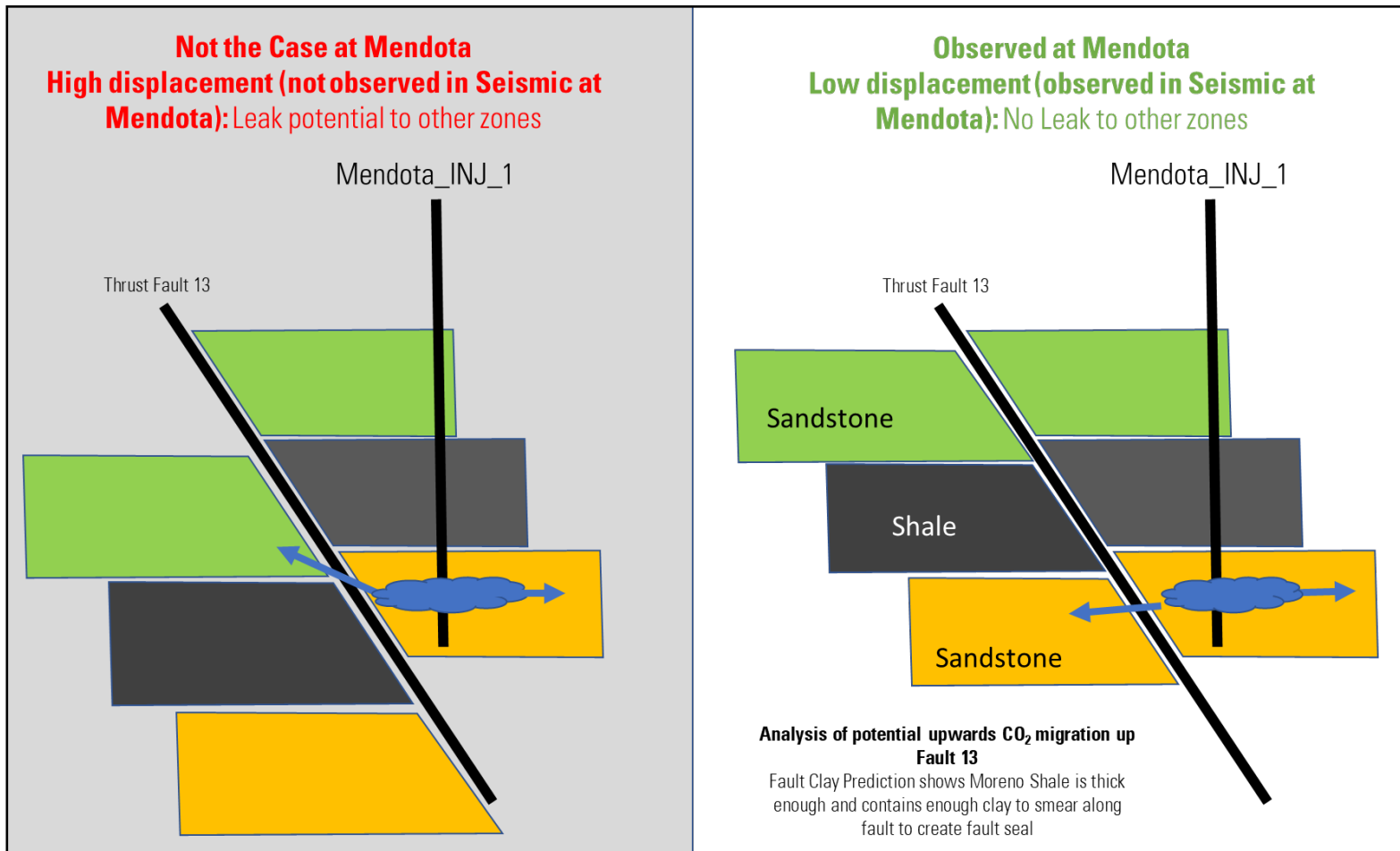


Figure 23. Different fault displacement scenarios at Mendota_INJ_1 regarding Fault 13.

2.4 Injection and Confining Zone Details [40 CFR 146.82(a)(3)(iii)]

2.4.1 Structural Mapping

Well and 2D seismic data were incorporated into a geomodel in the Petrel software platform to determine depth, areal extent, and thickness of the injection and confining zones. Well tops were re-interpreted when necessary, but otherwise imported from DOGGR (DOGGR, 2019) or IHS (IHS, 2019) data sources. Surface gridding was completed using a combination of convergent and conformal interpolation mapping algorithms. Seismic interpretation data were used as secondary input for surface gridding. Table 1 shows the number of well top control points used in surface gridding. Figure 13 (Section 2.2) shows the structure maps. Figure 21 illustrates the 3D structural model built from seismic and well tops and converted from time to depth. The thicknesses and depths of the injection and confining zones at the Mendota site will be confirmed with the use of 3D seismic data and data gathered while drilling the injection and monitoring well.

Table 1. Well control points for structural model of injection and confining formations.

Formation	Well Control
Moreno	31
First Panoche	23
Second Panoche	11
Third Panoche	11
Fourth Panoche	10

2.4.2 Petrophysics

Petrophysical analysis for 10 wells (Figure 9) was completed using the Techlog* wellbore software platform and the Quanti.Elan* multicomponent inversion solver to estimate porosity and permeability of the injection and confining zones targeted for geologic storage. The basic log data were from wells drilled between 1942 and 1987 (Table 2). Raw log data in both raster and LAS form were acquired from IHS (IHS, 2019) and DOGGR (DOGGR, 2019) The logs were imported into the Techlog software and normalized. Petrophysical properties such as effective porosity (PIGE), permeability (KINT), and VCL were calculated. PIGE and KINT logs were used to populate the geologic model properties discussed in Section 2.4.3. Petrophysical results show a reasonable estimate of total porosity and permeability based on nearby legacy well data (California Department of Conservation, Division of Oil, Gas and Geothermal Resources, 1998); however, there is uncertainty in the effective porosity because an empirical relationship was used to estimate irreducible water. Based on experience, the empirical relationship of 20% for sandstones and 30% in shales was used as a reasonable cutoff in the model to estimate irreducible water. Irreducible water is calculated from porosity and permeability and therefore is subject to the same level of uncertainty as the porosity and permeability calculations. Further acquisition of logs and core will increase the accuracy of porosity and permeability estimates, which will decrease the amount of uncertainty regarding irreducible water. Future irreducible water calculations will use data from logs and core to develop empirical relationships for petrophysics. These new calculations will be available to help refine the simulation modeling.

The petrophysical workflow involved building a model using well log data from NAPA AVE A 1 calibrated to core data from the same well (TGS, 2019). This workflow was applied to the other nine petrophysical wells, which did not have core data to determine the porosity and permeability. As shown in Table 2, some of the wells have a limited set of well log data. The petrophysical property uncertainty around these wells was reduced by calibrating parameters and multiwell comparisons across different formations. The petrophysical evaluation focused on the formations included in the geological model from the Garzas formation to the Precambrian basement. Petrophysical calculation results are illustrated in the cross sections in Figure 24, Figure 25, and Figure 26.

NAPA AVE A/1 may not prove to be a perfect analogue of expected mineralogy at the proposed Mendota_INJ_1 site as it is approximately 8.3 miles east and updip from the site. Uncertainty persists regarding to the lateral continuity of the formations, which could produce variations in the reservoir properties and mineralogy. This uncertainty will be significantly reduced by acquiring 3D seismic data and logging a comprehensive suite of wireline tools and core data, as detailed in Attachment G: Construction Details (Schlumberger, 2021g), from a characterization well drilled in future phases of this project.

VCL logs derived from petrophysical modeling were used to generate a simple lithology log of sand and shale for the purpose of fault seal analysis. VCL log values greater than 30% were considered shale and anything less than 30% VCL was flagged as sand. The resulting facies logs are shown in the Figure 24, Figure 25, and Figure 26 cross sections. Facies definition will be re-evaluated and refined as new well data are added to the petrophysical model, and a heterogenous rock analysis (HRA) facies will be assigned comprising all relevant data from logs and core. HRA facies assignment uses principal component analysis to classify rock types based on their fundamental attributes of texture and composition as discriminated by log inputs. The advantage of this approach is that results are not biased to human interpretation. The limitations of the HRA facies determination is that the result may or may not be directly correlated with geologic depositional models. Algorithmically, HRA identifies consistent data structures, defined initially by unsupervised pattern recognition of the input data channels (well logs). The unsupervised classification is thus predicated on the structure of the data variance and not on preconceived ideas of what these classes should represent. HRA is driven by well data, and because existing well data is sparse and biased towards gas fields, the results of HRA analysis will contain the same bias.

Figure 27 shows facies thickness maps of the Moreno shale caprock and First and Second Panoche sand intervals. At Mendota_INJ_1, the estimated thickness of the First Panoche sand is 325 ft and the second Panoche sand 1,000 ft. The Moreno shale caprock seal thickness is estimated at 1,000 ft and the First Panoche shale thickness is estimated at 128 ft. Within the AoR, the thickness of the injection target varies from approximately 1,000 to 2,000 ft. The Moreno shale main seal reaches thicknesses of approximately 500 to 1,700 ft, as shown in Figure 27. Regional well data show Panoche sand targets to be continuous across the modeled area based on well log data as discussed in Section 2.2.

Table 2. Wells used to characterize petrophysical properties within the AoR.

Well Name	UWI	Latitude (deg)	Longitude (deg)	Spud Date	Data Available ^a
AMBASSADOR NL & F/2	4039001440000	36.85492	-120.34239	09-23-1962	SP, DT, Resistivity
B B COMPANY /1	4019207520000	36.774431	-120.334662	04-12-1973	SP, DT, Resistivity
GILL / 38-16	4039000460000	36.79396	-120.23433	12-02-1942	SP, Resistivity
KERHY PROPERTIES / 1	4019216070000	36.86941	-120.21743	01-14-1978	GR, DT, RHOB, NPHI, Resistivity
NAPA AVE A /1	4019225380000	36.75919	-120.21387	01-24-1987	GR, DT, RHOB, NPHI, Resistivity, Core
NL & F ARNOLD / 1	4039200320000	36.86496	-120.39371	03-07-1982	SP, DT, Resistivity
SACHS MCNEAR NO 1_2	4019060420000	36.6767	-120.30546	08-18-1965	SP, DT, Resistivity
SALLABERRY / 1-6	4019215350000	36.74573	-120.26308	07-27-1981	GR, DT, RHOB, NPHI, Resistivity
STERLING COLEMAN /1	4019203700000	36.70535	-120.337582	07-14-1969	SP, Resistivity
YOUNG ETAL / 1	4019204110000	36.66817	-120.23627	12-19-1969	DT, RHOB, Resistivity

^a Log types: DT, compressional slowness; GR, gamma ray, NPHI, neutron porosity, RHOB, bulk density, SP, spontaneous potential.

Although the wells are spread over several miles, they are located in the same Cretaceous depositional setting expected at the proposed injection well based on regional mapping and published interpretation (Hosford Scheirer & Magoon, 2007b). The well nearest to the AoR that reaches the Panoche formation is B.B. Company 1 (2 miles northeast of Mendota_INJ_1). Digital log responses from B.B. Company 1 show sandstones that correlate across the 10 petrophysical wells below and above the First Panoche shale. These sandstones are interpreted as either part of the distal deltaic sandstones or the channel fan sequence on the slope. CES expects that within these sequences there may be some minor differences in mineralogy, grain size, and porosity, but that, in general the properties will be similar.

Calibrating the petrophysical model to the core data involves taking the core variables (bulk density, porosity, permeability, mineralogy, etc.) and overlaying them on top of the corresponding well log or processed log variables for comparison and making model adjustments as needed. In addition to performing a direct comparison, the data were also plotted as trend vs. depth (for example, increase in permeability/porosity or changing clay volume with depth). Adjustments were made to refine the model to improve the relationship between core and well/processed logs. In the model, endpoints of the minerals were altered, constraints on volume

of minerals, and other adjustments were made in the porosity/permeability relationship to enhance the correlation.

Variabilities can exist with both core and log data due to the age of the information, existing technology when data was acquired, experience and quality of the service company, handler/logger errors, differences in resolution of the data, and digitization of paper logs. These variabilities are within the standard level of uncertainty and are addressed in the core to well calibration. New core and log acquisition will indicate whether any changes can be made to the petrophysical model to help with the log-to-core calibration or if the cores themselves are of poor quality and not a good representation of the formation.

After logs and core have been obtained from the injection well, permeability and porosity estimates will be refined, and geology and reservoir models will be updated using these data. Site-specific data will reduce overall project uncertainty. In addition, using the site-specific data, an uncertainty program will be designed to understand model sensitivities in greater detail, analyzing variables such as effective porosity. When core is acquired, effective porosity (with a range of error) will be calculated via laboratory measurements.

In principle, the methods described above will be used to compare the core and well log data at the injection site. However, at the Mendota site, additional cores and well logs will be acquired. With modern core processes and the latest logging technology, it will be possible to compare not only porosity and permeability but also mineral weights and volumes, geomechanical stresses, geochemistry, total and effective porosity, and saturations. Zone-to-zone adjustments will be required in the model to account for changes in the formation that are observed in the acquired core. The calibration from log to core is not made for the simple fact that the log variables must match the core variables. Physics of the inputs need to be real and not forced, meaning the model inputs must agree with each other and make sense. The calibration of the petrophysical models' outputs to the processed core variables requires an in-depth knowledge of the core measurements taken and how they align to the well log data. Modern core analyses and logs will enable a more accurate calibration between the two.

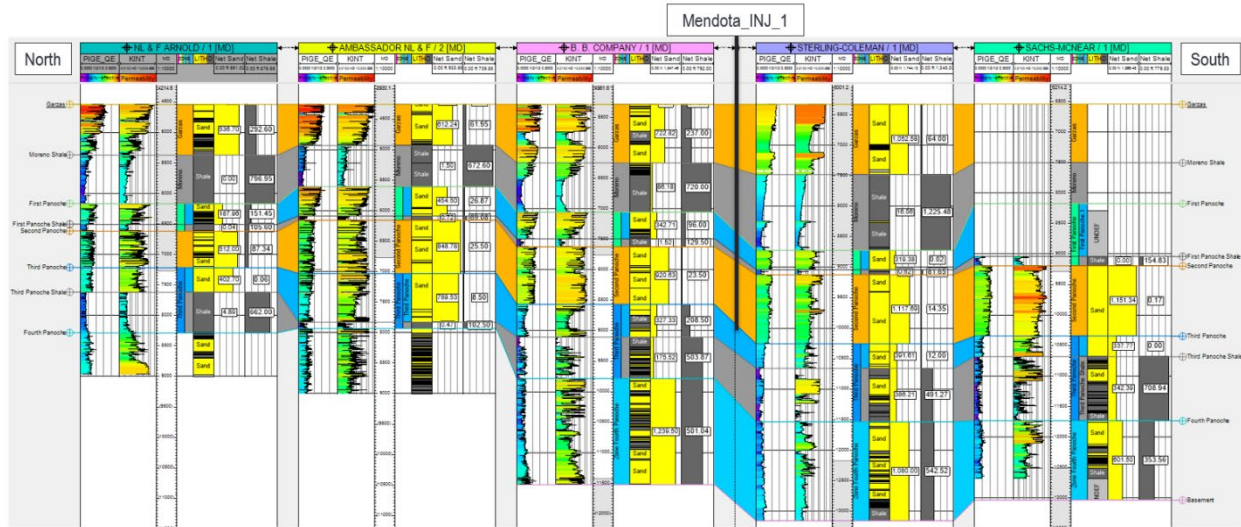


Figure 24. N-S cross section showing petrophysical analysis results and wells nearest to Mendota_INJ_1. From left to right, the tracks show PIGE, KINT, MD, zone log, sand and shale lithologies as calculated from VCL, and net lithology values for sand and shale per zone.

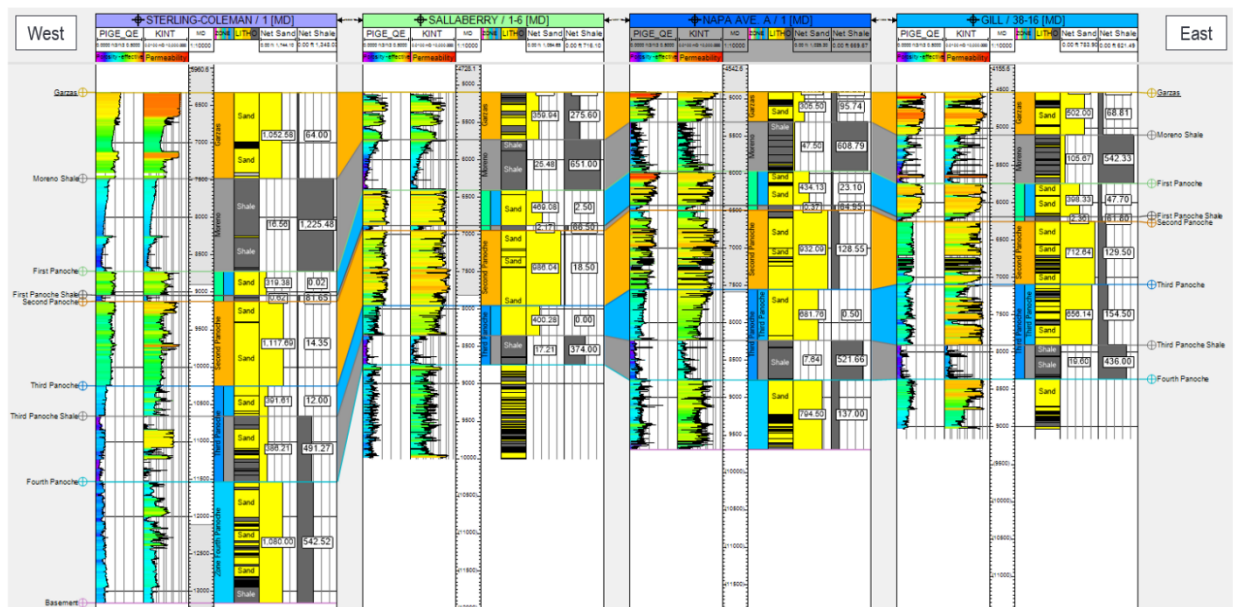


Figure 25. W-E cross section showing petrophysical analysis results. From left to right, the tracks show PIGE, KINT, MD, zone log, sand and shale lithologies as calculated from VCL, and net lithology values for sand and shale per zone.

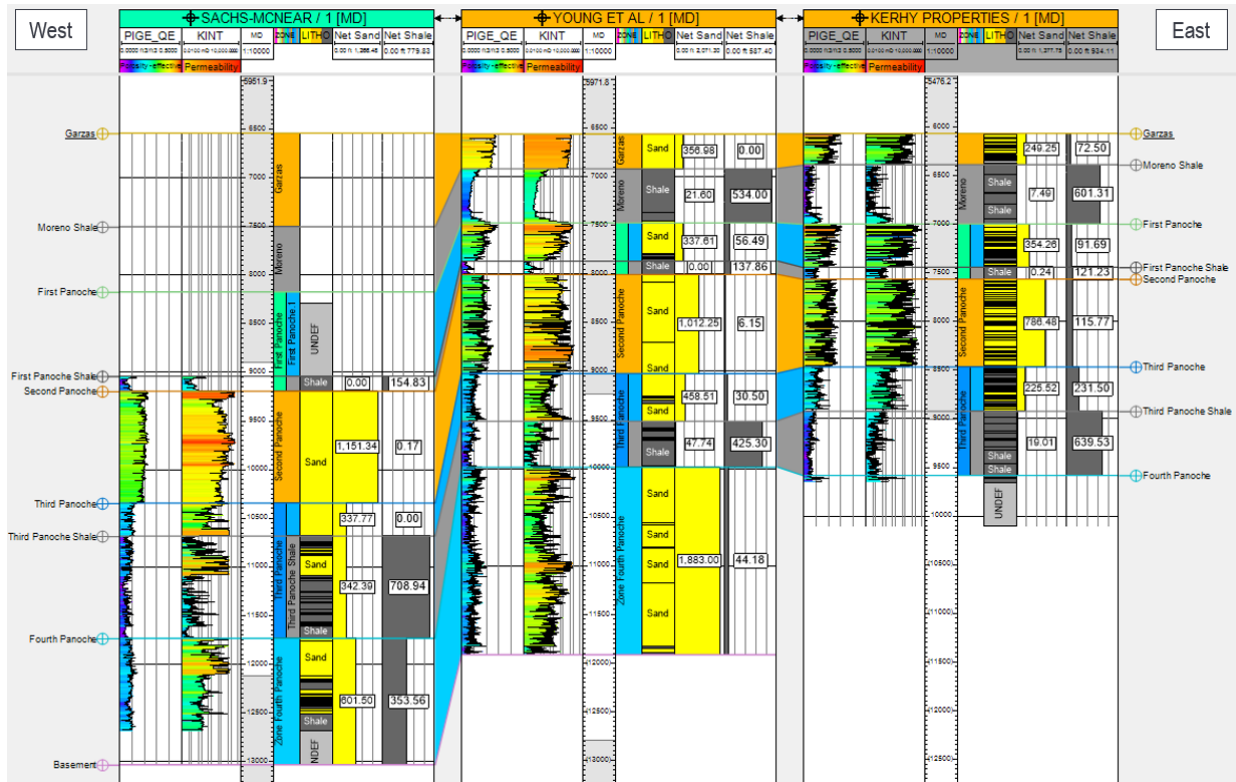


Figure 26. W-E 2 cross section showing petrophysical analysis results. From left to right, the tracks show effective porosity (PIGE), permeability (KINT), MD, zone log, sand and shale lithologies as calculated from VCL, and net lithology values for sand and shale per zone.

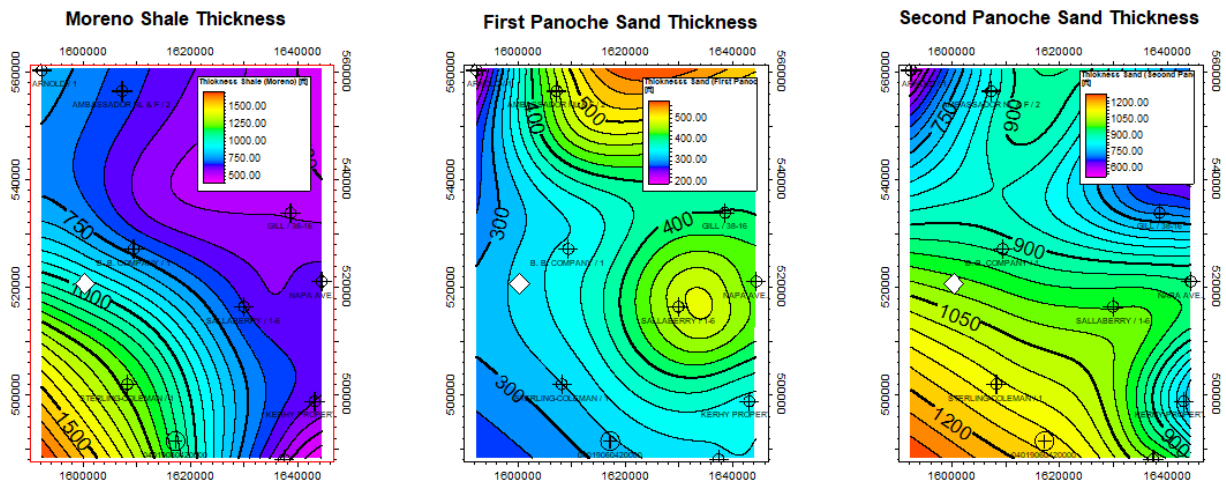


Figure 27: Net thickness maps of Moreno shale and First and Second Panoche sands calculated based on VCL greater than or less than 30%; the white diamond denotes Mendota_INJ_1.

2.4.2.1 Log-to-Core Calibration

Log-to-core correlation is the preferred method to calibrate petrophysical log data. The well, NAPA AVE A/1, had 47 core plugs acquired between the depths of 3,452 ft and 9,666 ft. The

legacy analysis performed on these core plugs in 1987 provided the core permeability, porosity, grain density, and water saturation. Another six core plugs were acquired between the depths of 8,200 ft and 8,751 ft for X-ray diffraction (XRD) analysis. Due to limited documentation as to how the core was acquired, how the points were selected, condition of cores at acquisition and processing, and the methods used to process the core, the data were used as-is with no refinements. These core points were compared with the petrophysical model evaluation outputs and adjustments were made to the model to align the core variables while still honoring reasonable model assumptions. Most legacy well log data aligned with modeling results from NAPA AVE A/1, but there is still the need for additional core data and logs to further enhance the petrophysical model.

The additional core and log data will allow for a better-fit model by accurately matching core in all zones. The future proposed coring program is designed to take several hundred feet of conventional whole core in the shales and reservoir packages as well as tens of rotary sidewall core samples as necessary to address any areas of interest identified during drilling. Drill cuttings will be gathered to identify changes in formations and mineralogy over the entire wellbore. Core processing in the laboratory will be performed on the whole conventional core, rotary sidewall cores, and drill cuttings and will include, but is not limited to porosity, permeability, mercury injection, fracture analysis, triaxial compression testing, XRD, X-ray fluorescence (XRF), fluid inclusion technology and FIS* fluid inclusion stratigraphy analysis on cuttings, and scanning electron microscopy (SEM) analyses. These core measurements will be used to calibrate the logs gathered and the resulting models. The spectroscopy and density neutron logs will facilitate the lithology determination in accordance with the XRD and XRF core measurements. Combinable magnetic resonance and density/neutron logs will determine the porosity and permeability and align with the core measurements taken. Sonic and density logs will be used for geomechanics and will be compared with the triaxial compression measurements taken in the sands and the shales. All core data will be used to verify and calibrate the log models and outputs.

Any poor relationships between the core and log measurements will be evaluated to understand the reason for the discrepancy. The discrepancy may be related to errors related to one or more log acquisitions, problems with acquisition of the core samples, core heterogeneity not matching scale of logs, or core plug issues. If necessary, whole core could be used for additional processing if further validation is required for the log model.

2.4.2.2 Porosity

The total porosity of the injection zone was determined from either the bulk density or compressional slowness depending on data availability. The porosity of the Third and Fourth Panoche sands is lower than that of the First and Second Panoche sands, as evidenced by the denser, faster log responses seen on the raw logs from all the wells within the geologic model. Clay volume was estimated from the spontaneous potential or gamma ray log to derive the clay-bound water.

This effective porosity was distributed into the geomodel. The average effective porosity for the injection and confining zones is shown in Table 3.

2.4.2.3 Permeability

The intrinsic permeability was estimated based on the porosity and lithology of the formation (Herron, 1987) using the wells around Mendota_INJ_1. The lithology model consisted primarily of quartz, clay, and feldspars based on the core from NAPA AVE A/1. The average permeability of both the injection and confining zones is shown in Table 3.

Table 3. Average porosity and permeability of injection and confining zones as calculated from NAPA AVE A/1.

Formation	Average Porosity (%)	Average Permeability (md)
Moreno	8	4.7
First Panoche	20	300
Second Panoche	18	290
Third Panoche	12	140
Fourth Panoche	10	87

2.4.2.4 Mineralogy and Geochemistry Analysis

The mineralogy around the Mendota site is assumed to be like that from the well NAPA AVE A/1. The core XRD report indicates the presence of quartz, K-feldspar, plagioclase, pyrite, clay, and calcite stringers, as shown in Table 4 (California Department of Conservation, Division of Oil, Gas and Geothermal Resources, 1998). Expected geochemical reactions to the injected CO₂ stream are discussed in sections 2.8.2 Mineral Composition of the Injection Zone through 2.8.5 Simulated Reaction Pathways of this narrative. A more comprehensive analysis is planned using core and geochemical logs from a characterization well in a future phase of this project.

Table 4. Mineralogy summary from core XRD for NAPA AVE A 1.

Depth	Quartz	K-Feldspar	Plagioclase	Calcite	Ankerite	Siderite	Pyrite	Barite	Clay
ft	%	%	%	%	%	%	%	%	%
8,200	32	22	35	—	—	—	4	—	7
8,208	15	10	22	1	—	—	7	—	45
8,222	19	13	20	—	—	—	5	3	33
8,612	36	20	33	—	—	—	—	—	9
8,618	20	12	16	25	3	11	—	—	9
8,751	36	20	33	—	—	—	—	1	10

2.4.3 Geocellular Modeling and Volumetrics

To estimate the spatial distribution of rock properties between wells, structural surfaces discussed in Section 2.4.1 were used to build the skeleton for a 3D geocellular model. The lateral grid resolution (cell size) was defined as 400 ft by 400 ft. A finer resolution grid will be considered for future modeling after incorporation of 3D seismic data. Log data from the 10 petrophysical wells (Figure 9) were upscaled using an arithmetic average into the cells along the wellbore (Figure 28). The upscaled log data (discussed in Section 2.4.2) provide the basis for populating the geomodel properties, which include effective porosity, permeability, clay volume, and pore volume. Petrophysical properties were distributed through the model domain using the Gaussian random function simulation (GRFS) algorithm. This kriging-based algorithm was used because it can generate multiple equiprobable realizations, which is preferred when working with sparse well data. Before this simulation is run, it is necessary to define vertical, major, and minor variograms to guide property distribution. Variogram modeling based on petrophysical logs shows a NE-SW depositional trend, with a vertical resolution of roughly 20 ft. The 20 ft resolution is likely representative of larger depositional changes (for example from highstand to lowstand sea level). To capture smaller changes within each depositional cycle, 4 ft-layer increments were defined for each zone. Because modeled zones are based on estimated facies changes, facies logs were not used as bias in the porosity or permeability models at this time. Facies biasing and kriging to 3D seismic data will be considered in future model iterations.

Histograms for porosity and permeability comparing petrophysical logs to upscaled (averaged based on layer increment) and to full-field simulated properties are illustrated in Figure 29 and Figure 30. The relationship between porosity and permeability is shown in the crossplots in Figure 31 and Figure 32. The Figure 31 porosity-permeability crossplot compares the raw logs in blue to upscaling results in green. Blue and green distributions are overlying one another, which indicates that the upscaling results provide a close match to raw log well data. The porosity-permeability crossplot in Figure 32 shows full field property distributions per zone, which follow trends similar to those observed in Figure 31. The close match suggests estimated porosity and permeability ranges can be predicted for the injection and confining zones based on the input legacy data. Figure 33 and Figure 34 show the simulated average porosity and simulated permeability thickness (KH) for each modeled zone is consistent with regional geology and predicted lithology type. The Moreno shale is regionally continuous and estimated to have low

porosity and low permeability, which is a requirement for an effective seal. The Second Panoche injection zone is estimated to have high porosity and permeability throughout the model domain area to support the injection of CO₂. Figure 35 shows a base map with Mendota_INJ_1 at the center and N-S (purple) and E-W (orange) transverses. Figure 36 shows this same view in 3D, along with simulated effective porosity for the N-S and E-W transverses. This 3D view shows the Second Panoche and First Panoche shale to be continuous within the model domain, with low porosity confining zones present above and below the Second Panoche target injection zone to contain injected CO₂. Spatial distributions across the N-E and E-W transects for porosity, clay volume, and permeability are illustrated in Figure 37 through Figure 42. The seal integrity of the First Panoche shale (primary seal) and the Moreno shale (secondary seal) was only evaluated in terms of continuity and thickness at this time due to lack of site-specific data.

Within a 2.5-mile radius of the Mendota_INJ_1, the total pore volume of the Second Panoche injection zone was calculated using the 3D geocellular model; for each model cell, the porosity was multiplied by the cell volume. CO₂ storage capacity was calculated using the DOE's equation for CO₂ storage resource estimate potential in saline formations (DOE, 2015):

$$G_{CO_2} = A_f H_g f_{tot} \rho E_{saline}$$

where G_{CO_2} represents the mass of CO₂ that would be stored in the respective geologic medium; A_f represents area of formation; H_g is thickness of formation, f_{tot} is total volume of pore space; ρ CO₂ density; and E_{saline} is the efficiency factor based on P10, P50, and P90 (DOE, 2015). Efficiency factor represents the estimated percentage of pore space that may be occupied by CO₂ during injection.

Pore volume (10⁶ m³) was calculated to determine the storage capacity of the First and Second Panoche sands (Table 5). CO₂ density was estimated from pressure and temperature gradients at the midpoints of both the First Panoche sand and Second Panoche sand intervals. The pressure and temperature gradients were obtained from nearby oilfield data (California Department of Conservation, Division of Oil, Gas and Geothermal Resources, 1998). P10, P50, and P90 efficiency factors are defined by the DOE as 0.51%, 2%, and 5.5% and represent the fraction of the total pore volume of the saline formation that will contain injected CO₂. The results of this calculation estimate that the Second Panoche formation is suitable to receive the forecasted 350,000 tonnes/year of CO₂. The current DOE methodology used to calculate CO₂ capacity is normally applied for basin-scale estimates and does not consider certain variables such as multiphase flow processes, geochemical interactions, or trapping mechanism (EPA, Class VI Guidance Documents, 2019a). Injection formation factors such as porosity, percentage of sand, pressure, and temperature could cause the capacity to vary from the reported estimate. Static storage capacity estimation and methodology will be reassessed after formation-specific temperature and pressure are acquired from site specific well data as discussed in Section 2.4.4.

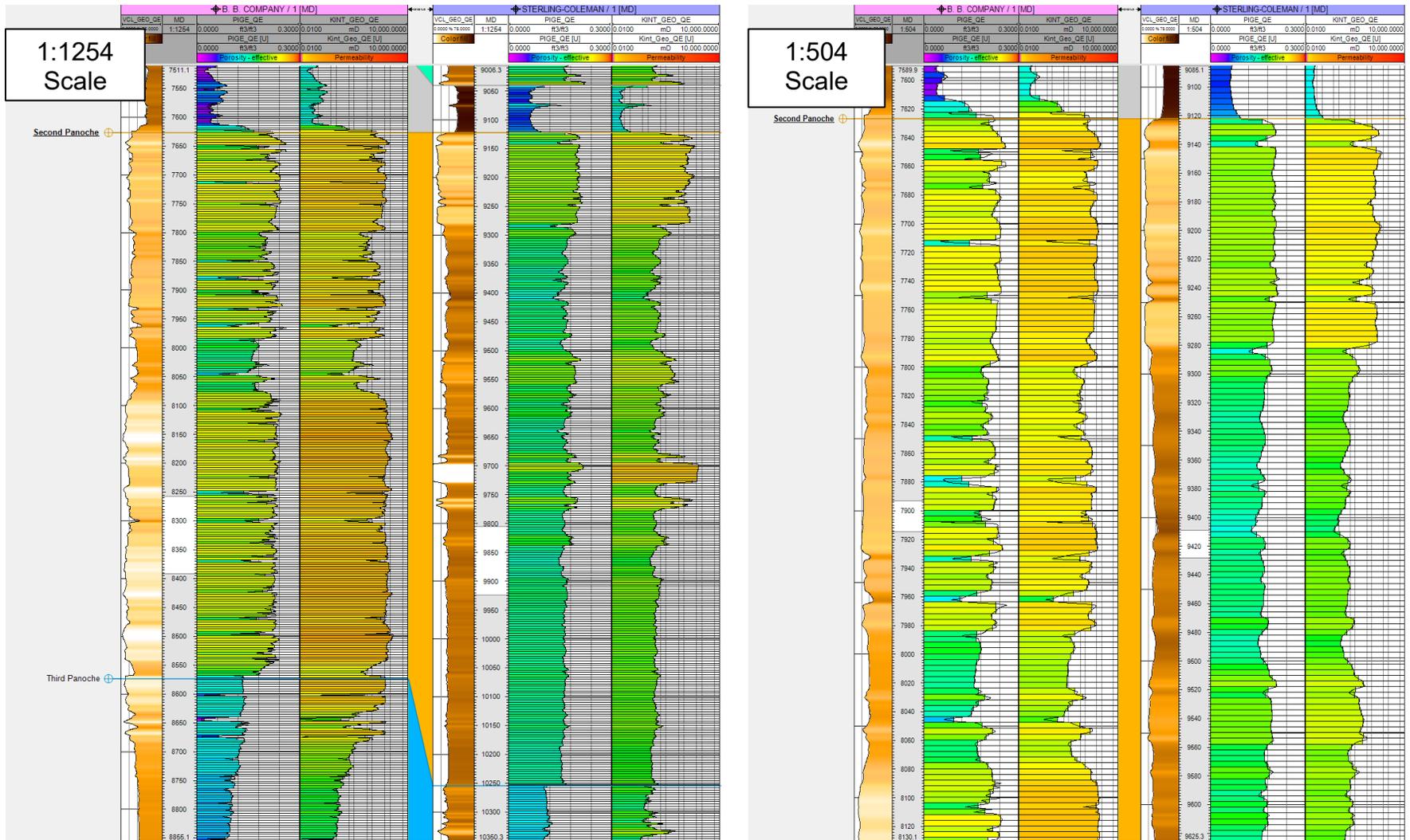


Figure 28. Example of PIGE and KINT upscaled well logs results for B.B. Company 1 and Sterling-Coleman 1 (closest petrophysical wells to Mendota_INJ_1 at different scales.

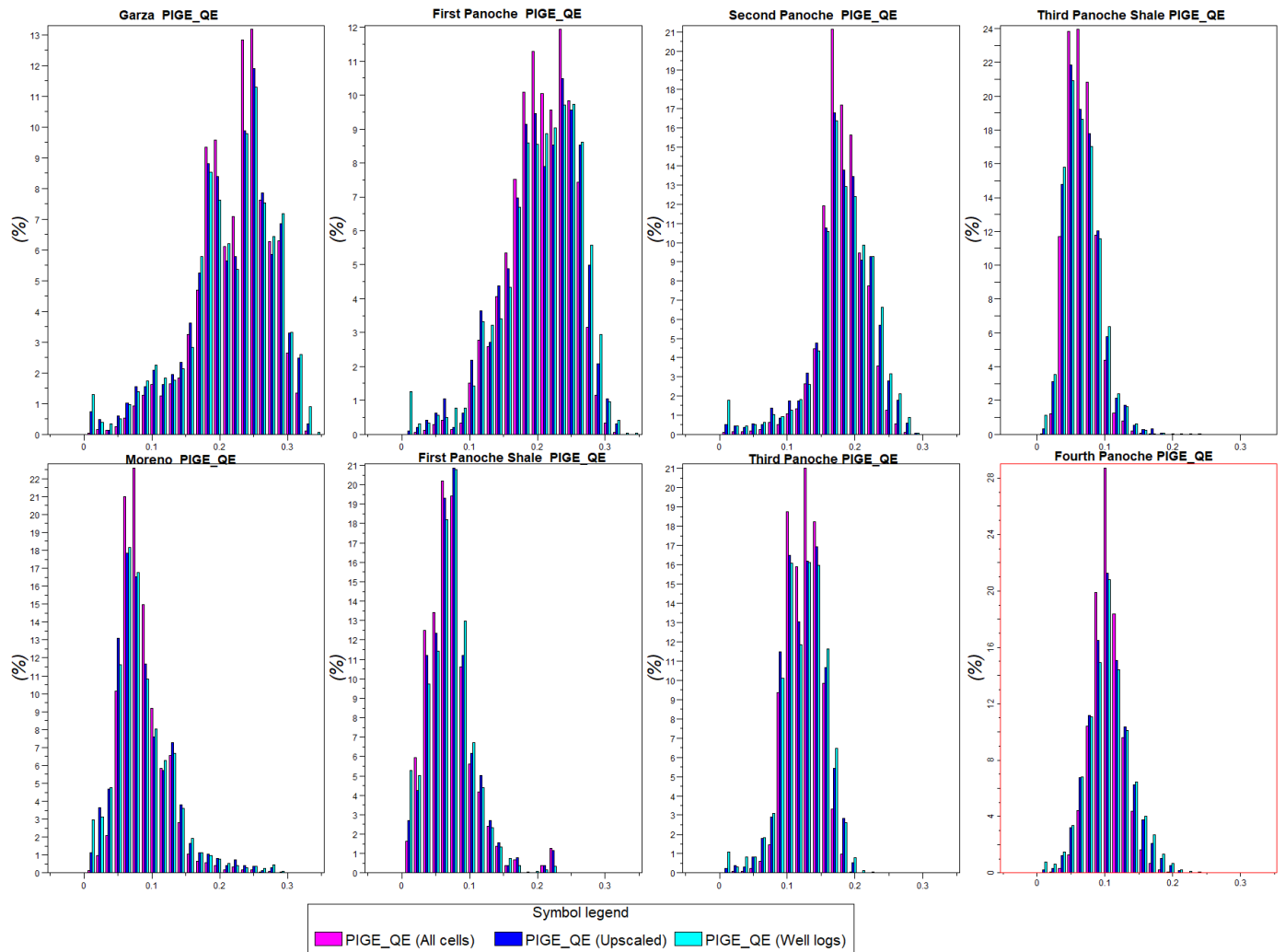


Figure 29. Porosity histograms of well logs, upscaled cells, and model cells.

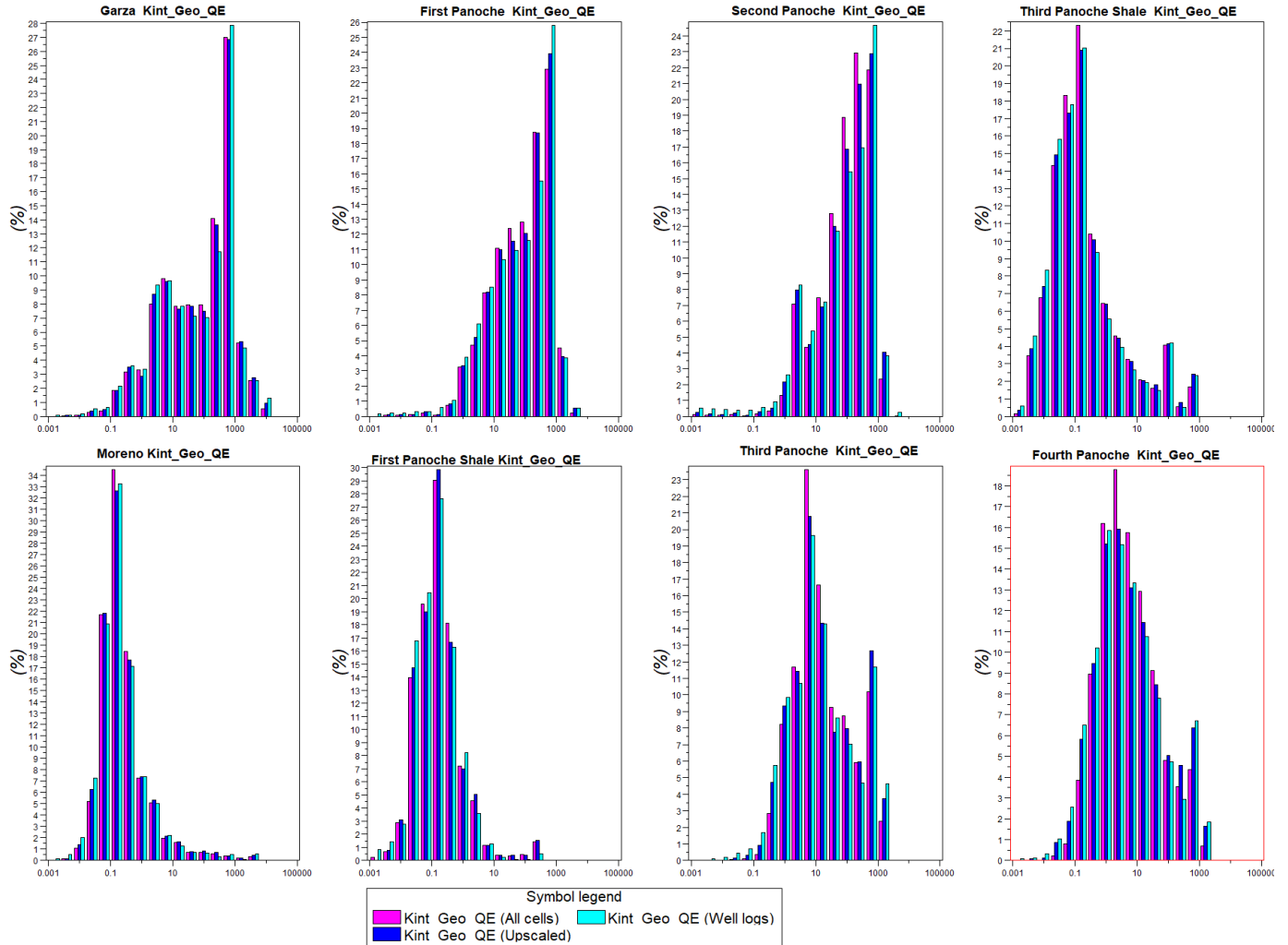


Figure 30. Permeability histograms of well logs, upscaled cells, and model cells.

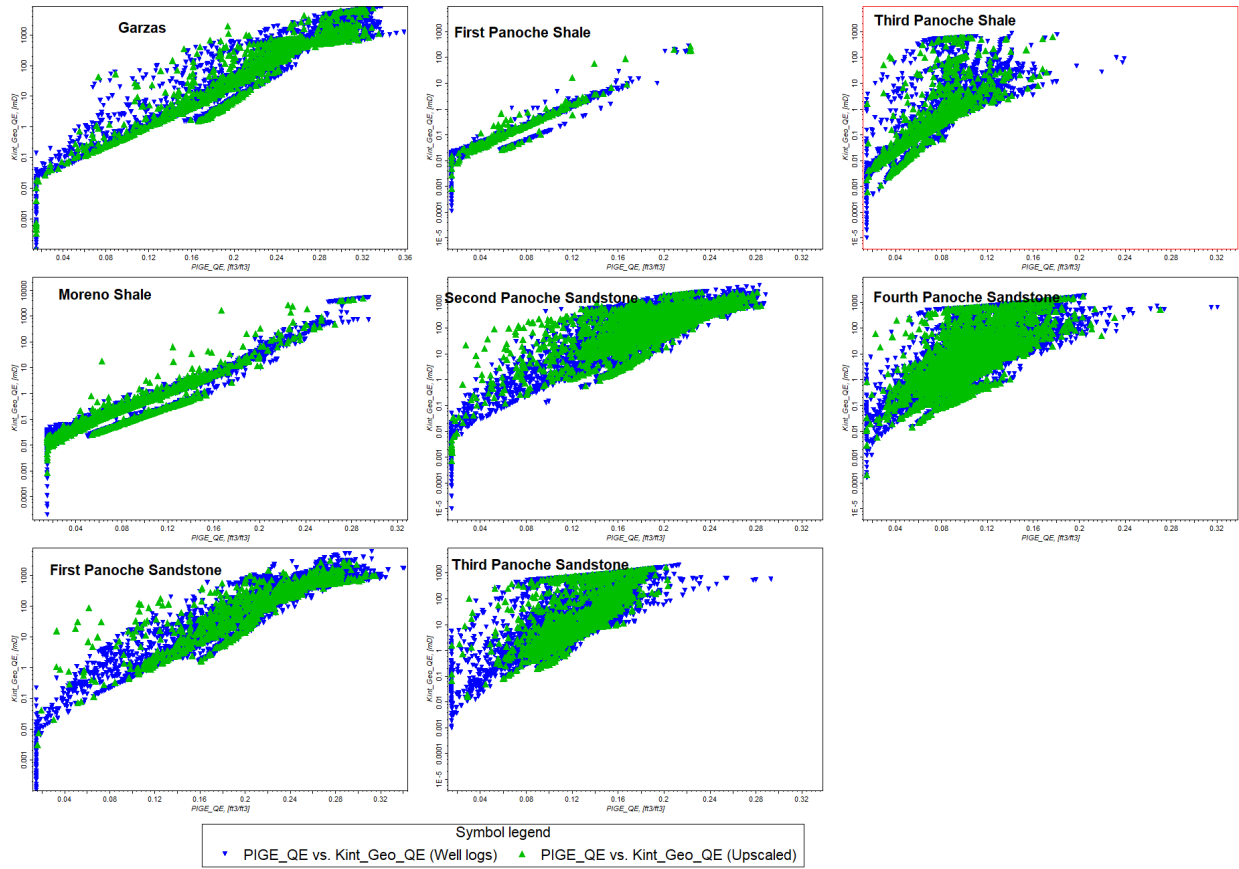


Figure 31. Porosity-permeability crossplots of well logs and upscaled cells.

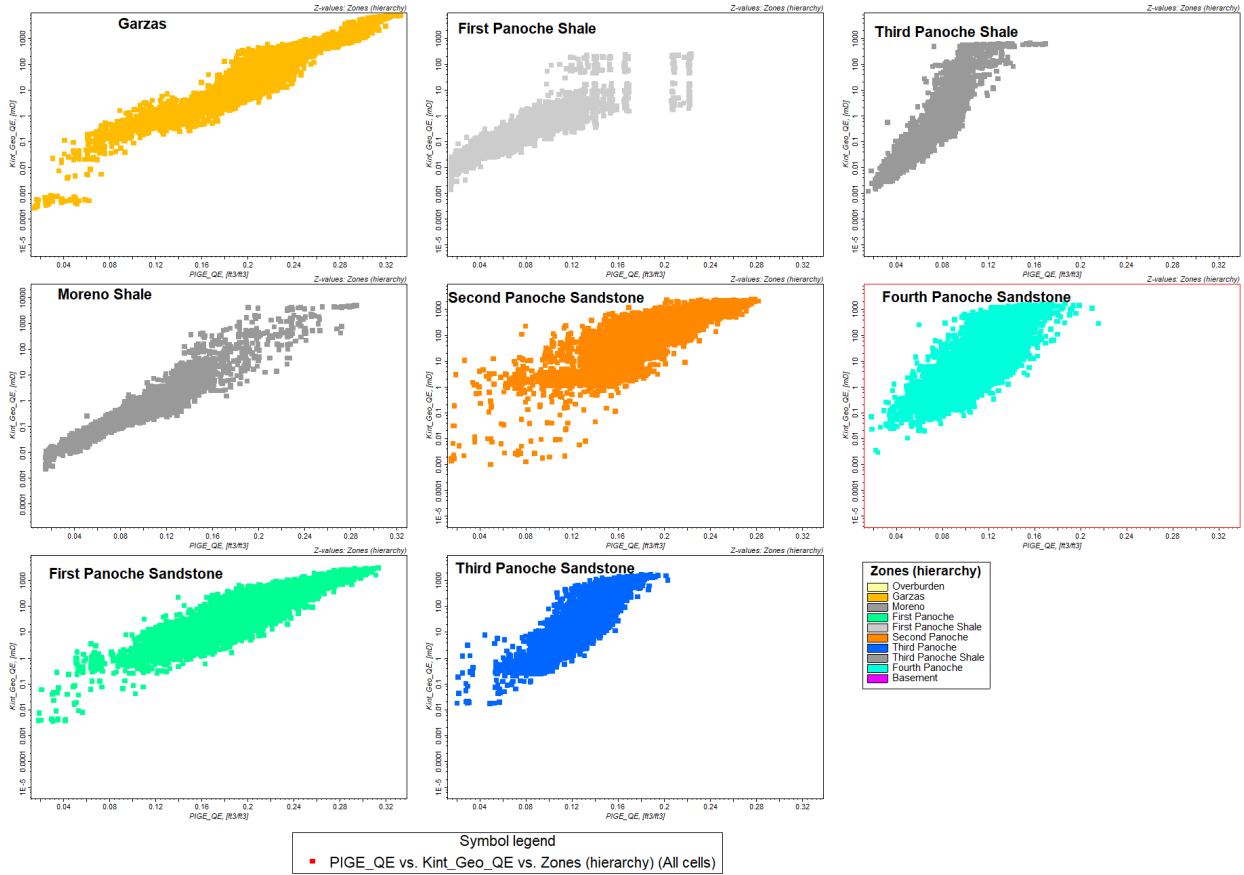


Figure 32. Porosity-permeability crossplot model cells colored by formation.

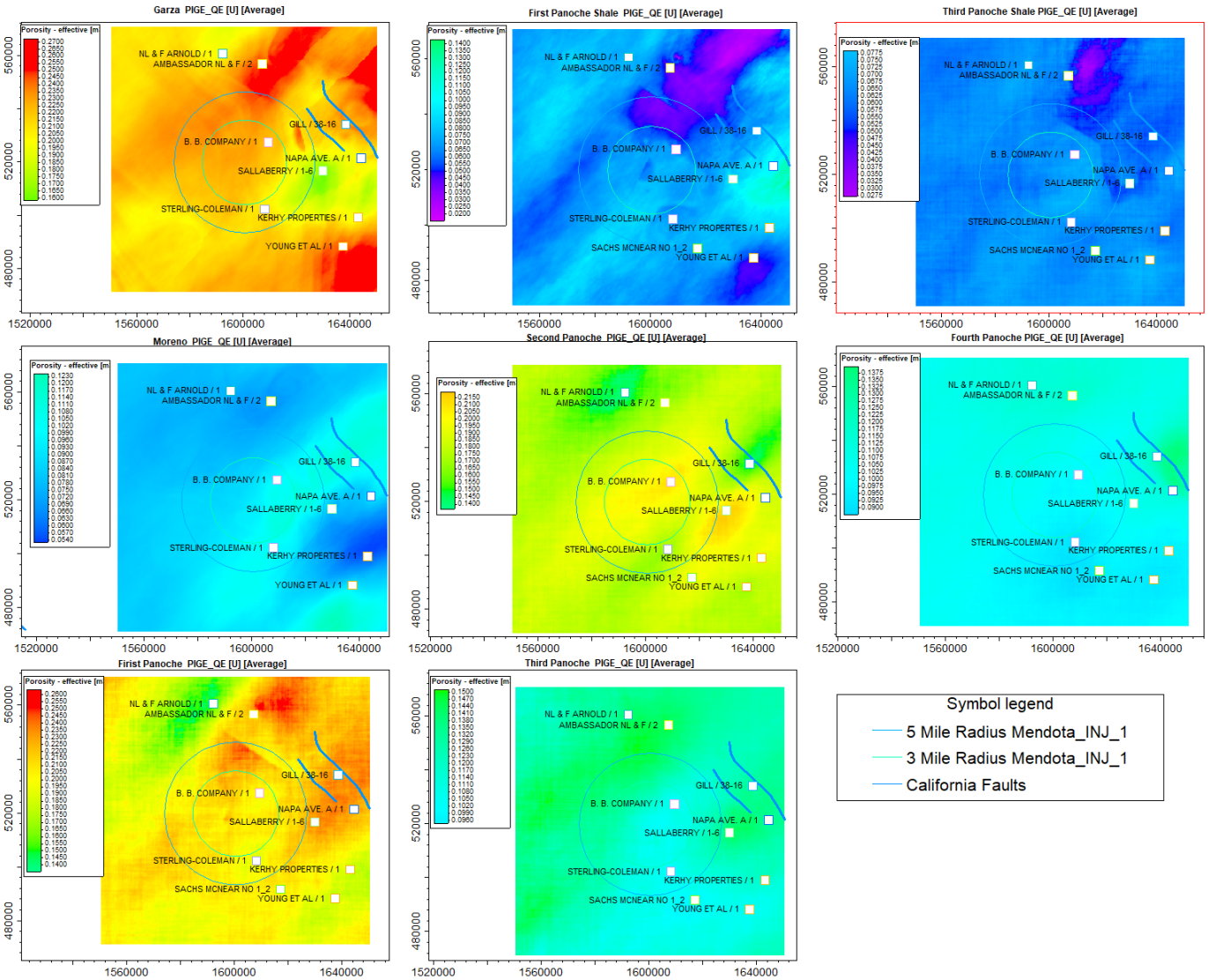


Figure 33. Modeled average porosity maps for each formation.

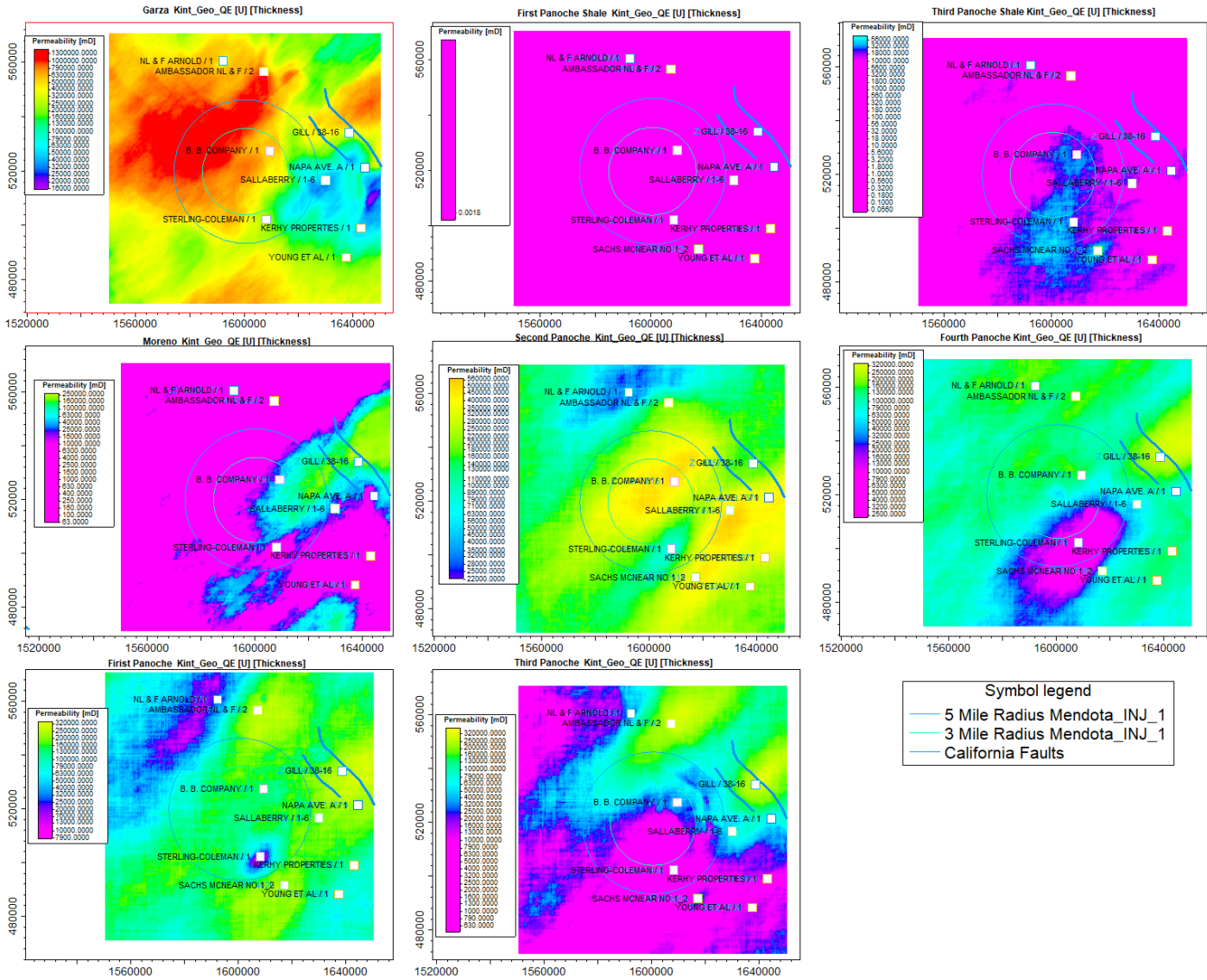


Figure 34. Modeled permeability thickness (KH) maps for each formation.

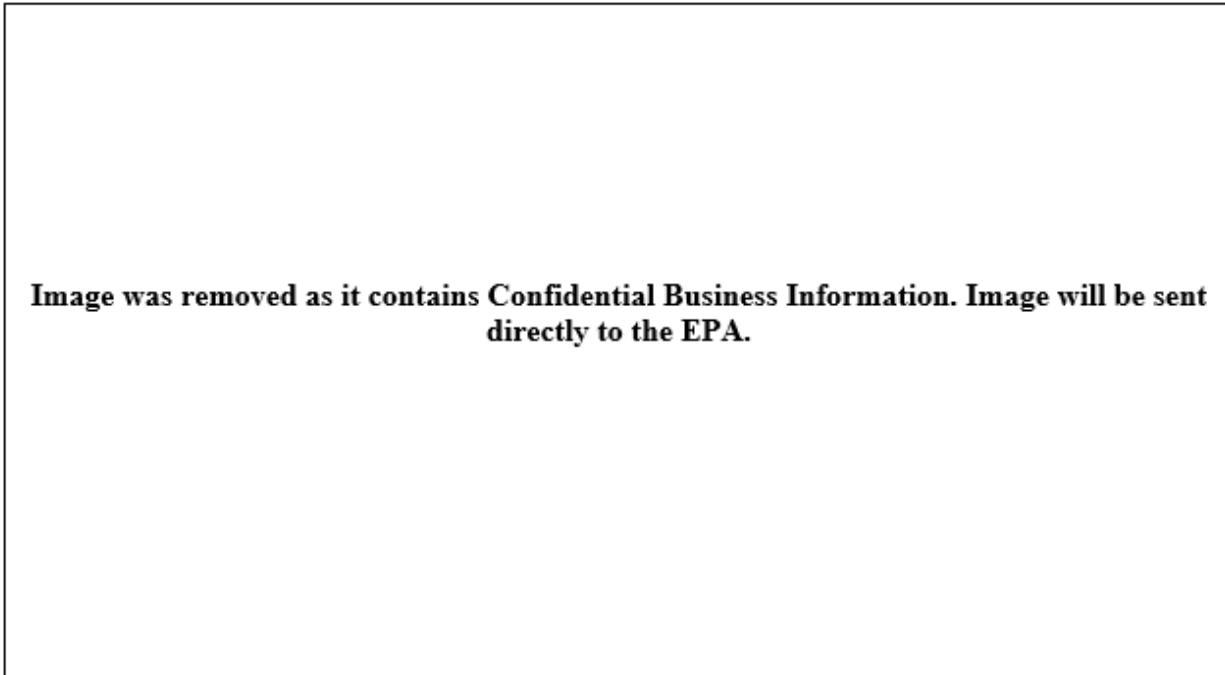


Figure 35. CONFIDENTIAL BUSINESS INFORMATION: Injection well cross-section traverse map, N-S and E-W. This image displays SEI data (2019), and it is marked as Confidential Business Information.

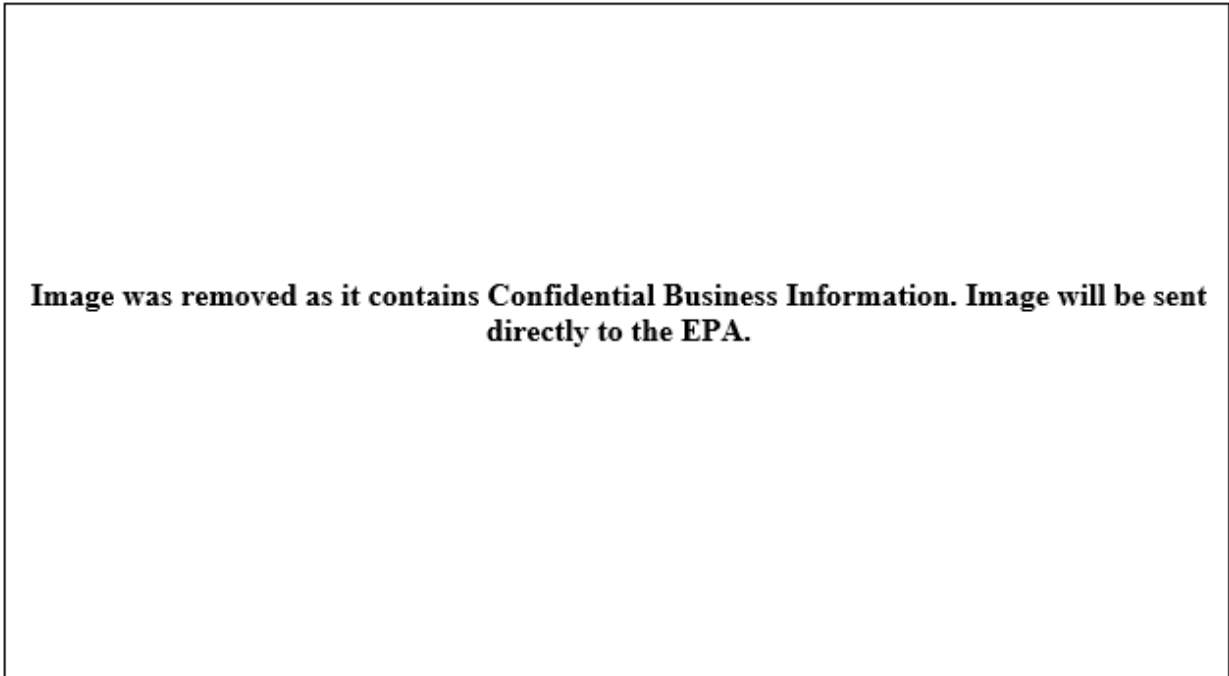


Figure 36. CONFIDENTIAL BUSINESS INFORMATION: 3D perspective of N-S and E-W porosity cross sections at Mendota_INJ_1. This image displays SEI data (2019), and it is marked as Confidential Business Information.

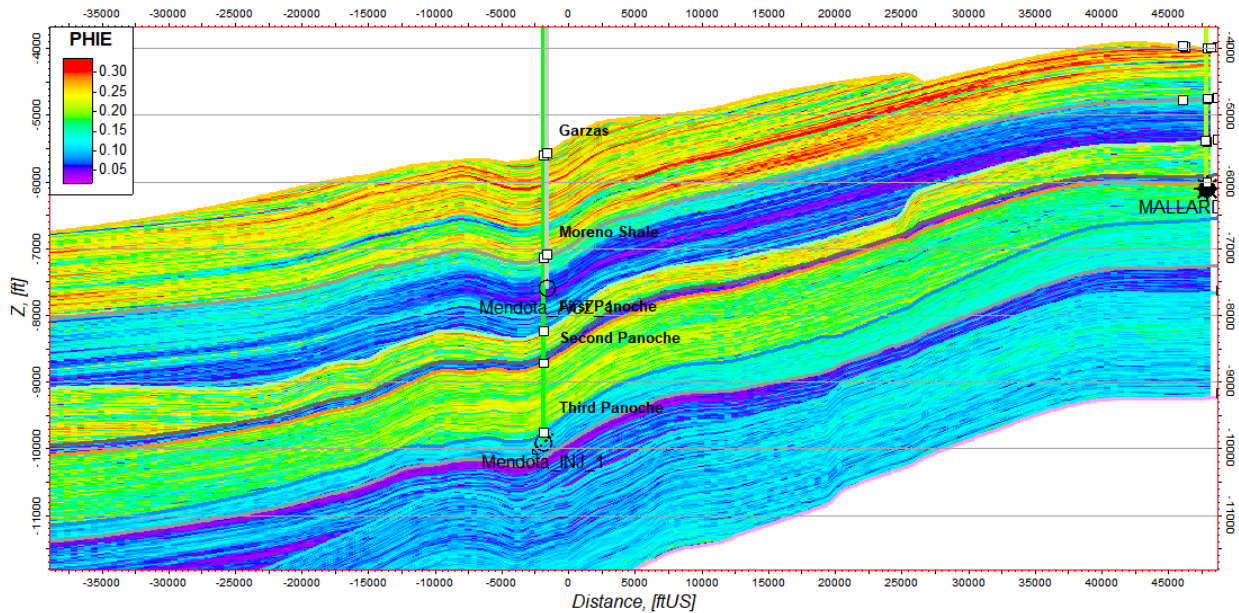


Figure 37. Effective porosity model cross section (N-S).

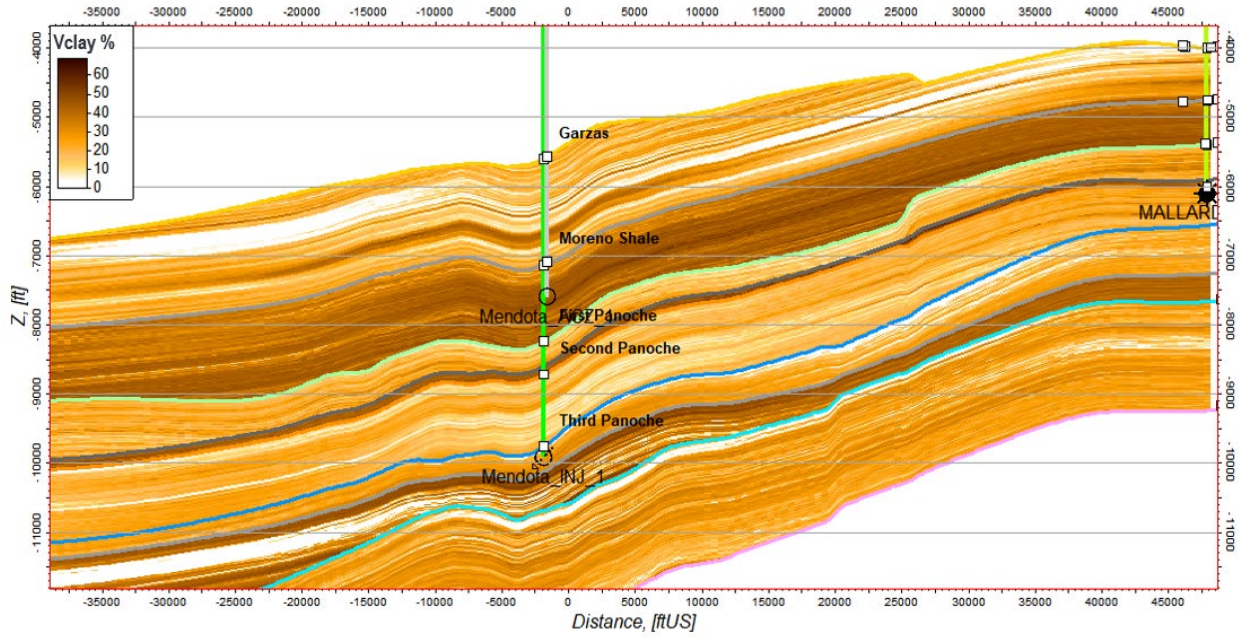


Figure 38. Volume clay model cross section (N-S).

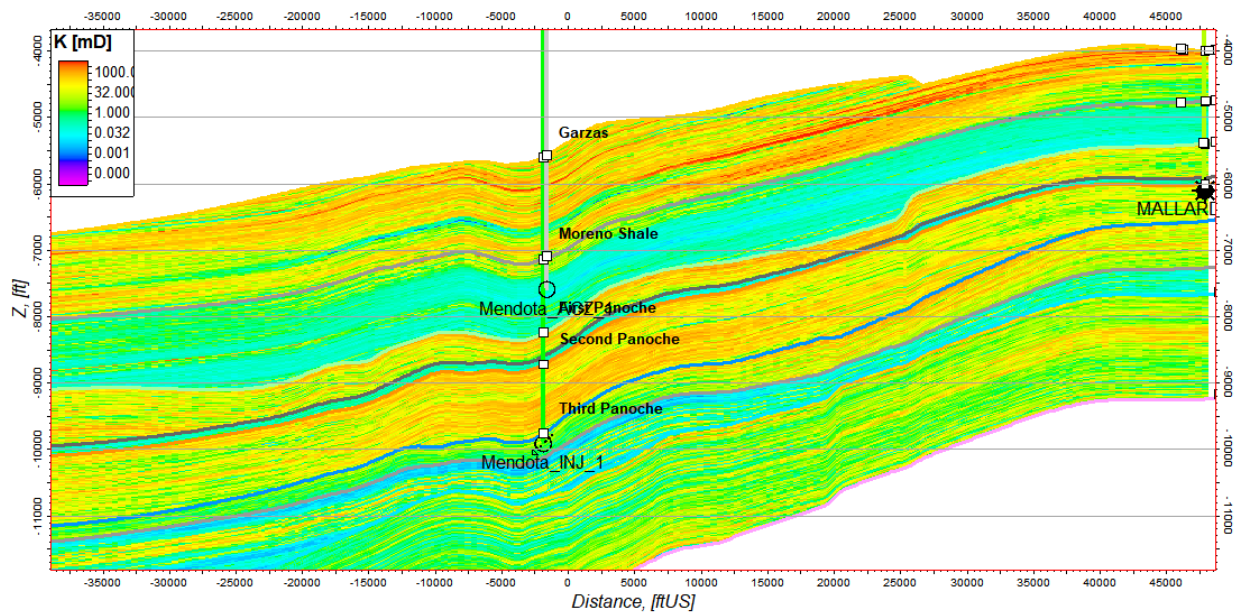


Figure 39. Permeability model cross section (N-S).

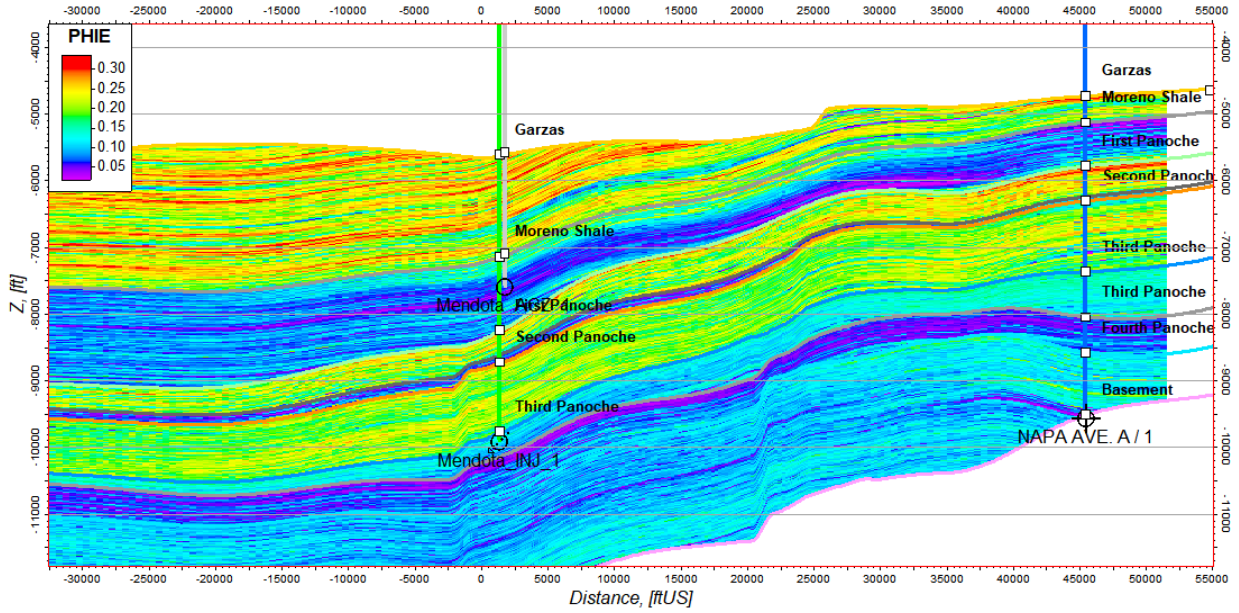


Figure 40. Effective porosity model cross section (E-W).

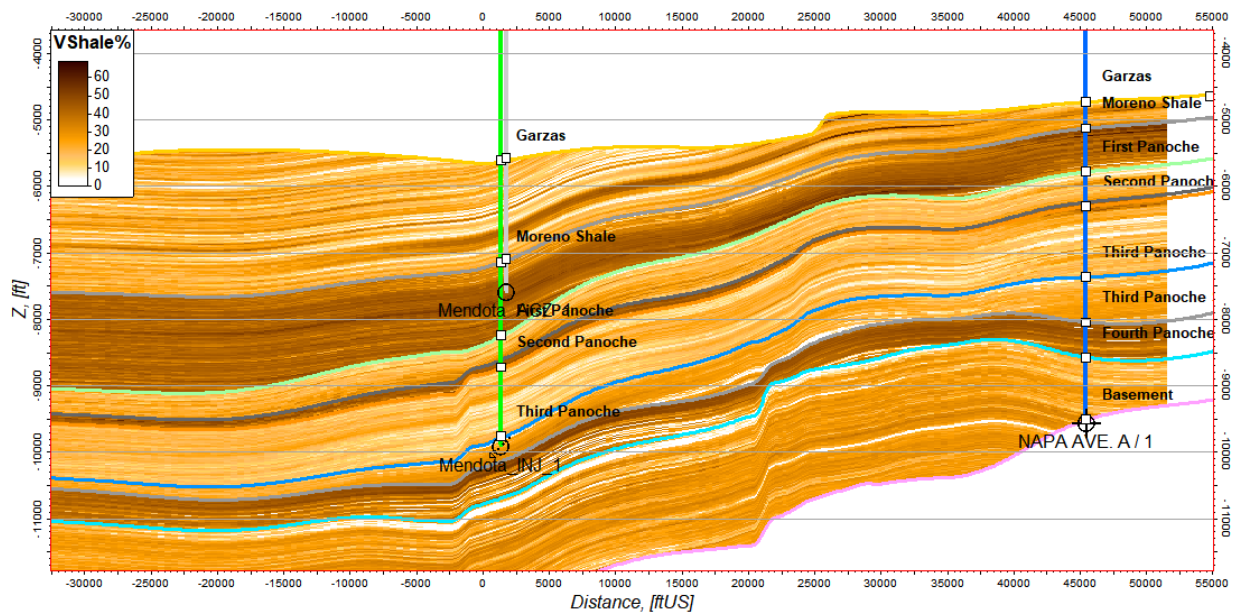


Figure 41. Volume shale model cross section (E-W).

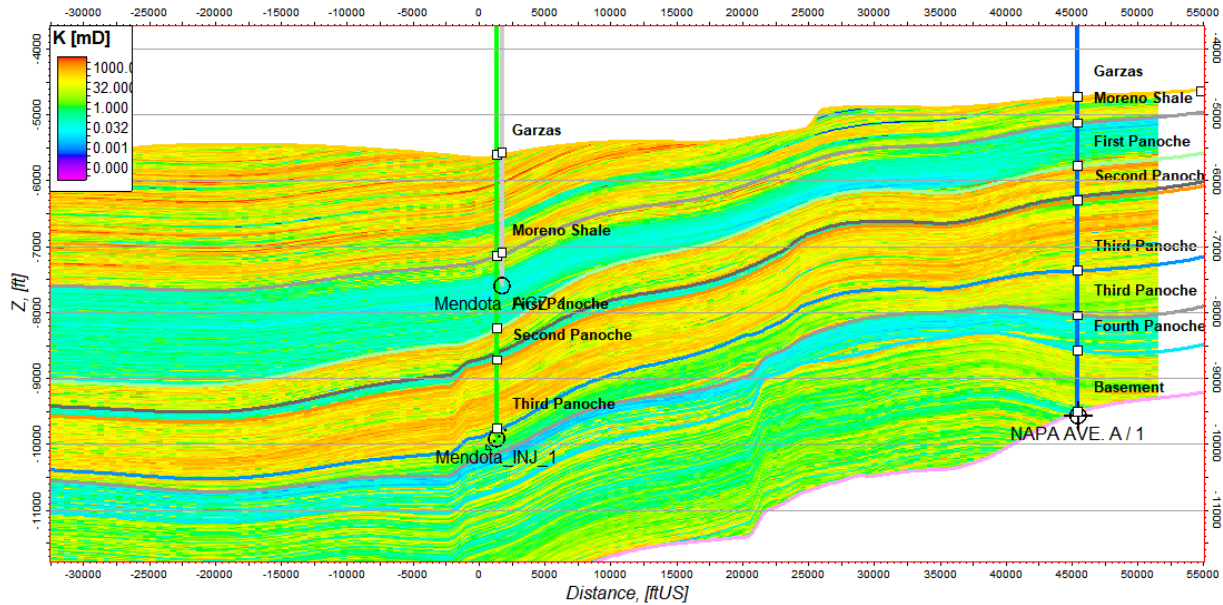


Figure 42. Permeability model cross-section (E-W).

Table 5. Storage capacity input parameters and results showing P50 capacity estimate in million tonnes.

	Temperature (°F)	Pressure (psi)	Density kg/m ³	Pore Volume 10×6 m ³	P50 Million Tonnes
First Panoche Sand	177.2	3,727	692.6	1,466	20.3
Second Panoche Sand	187.6	4,035	693	3,000	41.58

2.4.4 Pre-Operational Testing Requirements

Because a characterization well has not yet been drilled, and 3D seismic data were not included in this evaluation, there are many areas of uncertainty to be considered. The largest uncertainty is lateral thickness and homogeneity of injection and confining zones. Additionally, without 3D seismic data, the spatial extent and distribution of faulting are uncertain. Uncertainties can be better addressed in future iterations of modeling when newly acquired 3D seismic and seismic inversion products become available and can be integrated into the geomodel. Seismic elastic properties (Poisson’s ratio or Vp/Vs) and seismic inversion products (acoustic impedance and porosity) can be cokriged to well data to guide extrapolation of petrophysical properties in the model domain where well data do not exist. Moreover, geomechanical log properties should be acquired in the new well including anisotropic shear sonic for geomechanical analysis and for 3D stress analysis. This sonic data would also provide the basis for prestack seismic inversion to derive Poisson’s ratio or Vp/Vs from the 3D seismic data. Further, fracture logs from wellbore images from the FMI* formation microimager can be used to calibrate parameterization of seismic discontinuity analysis for detailed fault and fracture delineation, which, in turn, can be

used for developing a discrete fracture network. To support calibration of the geomechanical model, a geomechanics core testing program that includes uniaxial and triaxial compression testing to determine elastic and mechanical strength properties should be undertaken.

Because of the absence of laboratory measurement currently, capillary pressure in the confining zone (shale) was determined using the Van Genuchten model. Detailed description of the capillary pressure model and parameters applied to the model are found in Attachment B: Area of Review and Corrective Action Plan (Schlumberger, 2021b). Additional data that could help measure confinement zone integrity would include FMI image log measurements and drillstem test (DST) or MDT* modular dynamics tester stress testing information. These tests will also provide information on injection formation pressure and temperature to recalibrate the storage capacity estimate and dynamic simulation results.

2.5 Geomechanical and Petrophysical Information [40 CFR 146.82(a)(3)(iv)]

The petrophysical properties of the confining Moreno shale are summarized in Section 2.4.2. The elastic properties at Mendota_INJ_1 were evaluated using the existing acoustic and density logs of nearby wells shown in Figure 9. The average density in the Moreno shale is 2.13 g/cm³, and the average compressional slowness is 107 μs/ft (Figure 43) based on well logs from NAPA AVE A 1. An empirical correlation (Han, Nur, & and Morgan, 1986) was applied to derive the shear slowness due to the lack of shear measurements in available log data. The dynamic elastic properties including Young's modulus and Poisson's ratio are computed based on the density and compressional and modeled shear slownesses. The average dynamic Young's modulus and Poisson's ratio in Moreno shale is 1.9 Mpsi and 0.29, respectively (Figure 43). Due to the lack of core measurements from laboratory, there are no specific core data for the rock strength and ductility. Chanchani et al. (2003) measured rock mechanical properties of the Antelope shale in the Buena Vista Hills field with unconfined compressive strength in the range of 92 to 126 MPa (13,000 to 18,000 psi). Shales are typically more ductile than sand or limestone at the same confining pressure. Winters et al. (1987) showed that the ductility in shale can be 1.5% at a confining pressure of 5,000 psi. The geomechanical properties of the confining zone including the elastic properties, rock strength, and ductility can be measured in the laboratory using the triaxial compressional test.

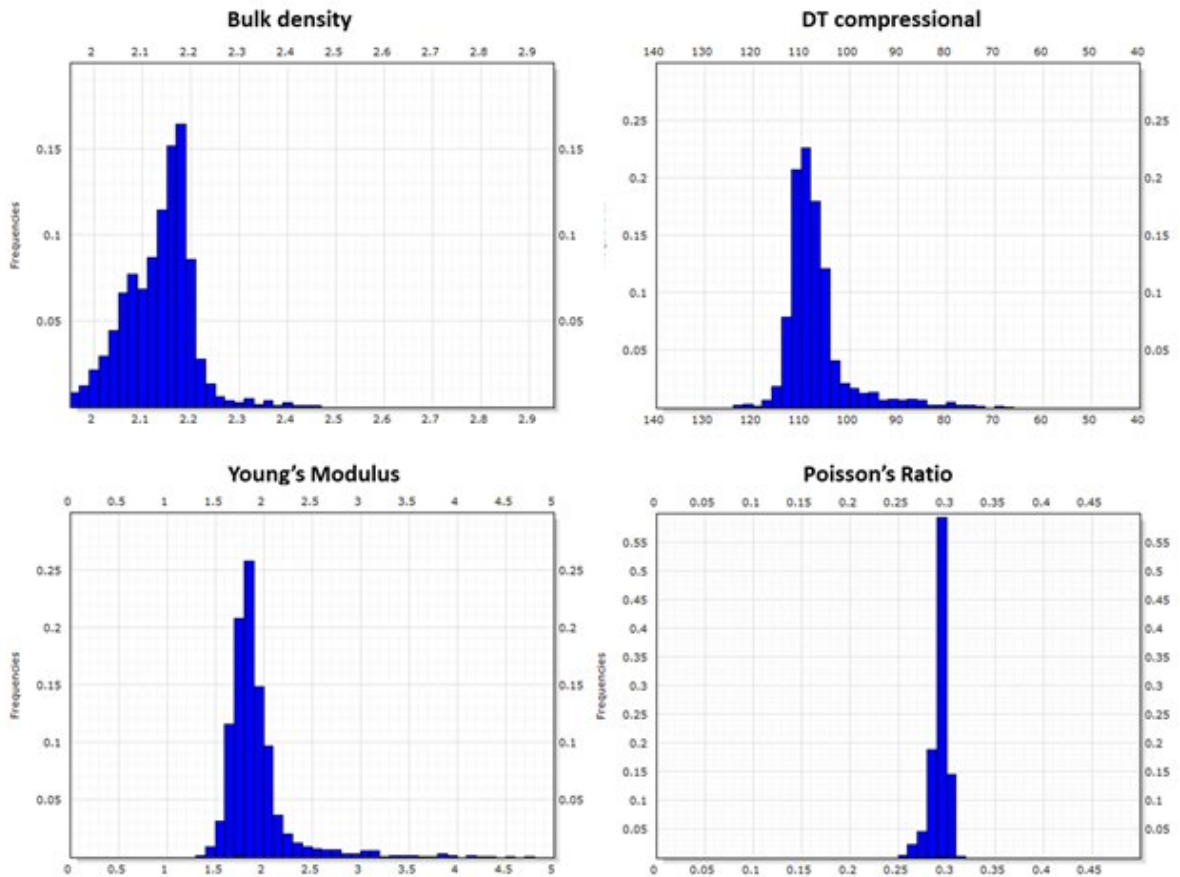


Figure 43. Density, acoustic, and elastic properties in the Moreno shale.

The amount of fracturing in the injection formation is not known at this time because of the lack of borehole image logs and 3D seismic data. In future phases of this project, borehole image logs will be acquired and used with 3D seismic data to determine the intensity of fractures in a discrete fracture model (see Section 2.3 Faults and Fractures [40 CFR 146.82(a)(3)(ii)]).

There are no direct measurements for in-situ stress. The in-situ stress field consists of three components: vertical stress, minimum horizontal stress, and maximum horizontal stress. The vertical stress can be determined by integrating the density of the rock above the depth of interest. Based on the available density logs in the area, the average density of the overburden rock is estimated to be 2.18 g/cm³ (or 0.94 psi/ft). The minimum horizontal stress (Shmin), which is typically the minimum principal stress, can be measured using minifrac or extended leakoff tests. The maximum horizontal stress (Shmax) can be obtained using different methods including the modeling of wellbore failure features such as drilling-induced tensile fractures or borehole breakout and the breakdown pressure from hydraulic fracture (Zoback, et al., 2003; Vernik & Zoback, 1989). In addition to the stress magnitude, the orientation of the maximum horizontal stress can be determined from the borehole image logs based on drilling-induced fractures and/or breakout. The world stress map indicates a maximum horizontal stress direction of N 40 to 57° E based on the earthquake focal mechanism and wellbore failure features. The in-

situ stress field will be better characterized in the next phase of this project after pilot hole logs and well test data are collected.

The stability and sealing capacity of the faults are also not clearly understood at this time because of limited site-specific data. A characterization well planned for the pre-operation phase of this project will include collecting important geomechanical information. These data will include geomechanical core analysis, pilot hole logs, and well test data. These data will be combined with 3D seismic data to build a 3D geomechanical model to provide a better characterization of the in-situ stress field, pore pressure, and rock strength, for the fault stability analysis and sealing capacity of these faults (Chiaromonte, Zoback, Friedmann, & Stamp, 2008). The analysis will be conducted at this time.

A normal pore pressure gradient was assumed at this point without additional well test data. Initial reservoir pressure was collected from a nearby oil and gas field (<20 mile) reported by the California Department of Conservation (1998). Pressure gradient of 0.4339 psi/ft is estimated based on the data (Schlumberger, 2021b).

2.6 Seismic History [40 CFR 146.82(a)(3)(v)]

Because California is situated along the Pacific and North American plate boundary, the region experiences significant earthquake activity. Figure 44 shows general earthquake activity and risk in relation to the Mendota site (CEMA, 2010). The relative risk of the proposed site is low compared with the active zones associated with major faulting.

Historical earthquake data were obtained from the USGS Earthquake Hazards database and imported into the Petrel platform for analysis (USGS, 2019a). All area earthquakes with a magnitude greater than 2.5 occurring since 1900 were considered for risk analysis.

Figure 45 shows the major fault systems in the region associated with primary earthquake activity and a map showing the USGS earthquake data highlighting the position of earthquake locations by relative strength in relation to the AoR. A narrow lineament of quake activity is associated with the San Andreas Fault located approximately 40 miles southwest of Mendota_INJ_1.

A cluster of smaller quakes of less than 5.0 magnitude (denoted by the red circle in Figure 45) occurred historically along an extension of the San Joaquin and Ortigalita fault systems trending NW-SE offset approximately 15 to 20 miles south and west of the AoR. The largest proximal quake in the area was the Coalinga Quake with a magnitude of 6.7 on May 2, 1983, located approximately 36 miles south of the AoR (USGS, 1983).

The AoR is positioned in a comparatively tectonically quiet area near the center of the San Joaquin Basin. Most activity occurs along the margins of the basin and is principally associated with tectonically induced faulting. The local earthquake activity near the AoR is shown in

Figure 46 with the magnitude, depth, and date annotated. A summary of the local quakes shown in this map is provided in Table 6.

The exact magnitude and proximity required for an earthquake to have disruptive impacts on CO₂ plume containment is unknown at this time. Various factors such as local stresses and fracture networks will need to be considered and are a source of uncertainty. Future iterations of modeling should integrate newly acquired geomechanical information (dipole sonic logs), FMI image logs, and microseismic monitoring to better address uncertainties regarding local tectonics and stress. Since 2000, there have only been three earthquakes located by the USGS Advanced National Seismic Survey within a 10-mile radius of the proposed injection site: a magnitude 2.64 recorded in 2003, a magnitude 1.96 in 2008, and a magnitude 1.8 in 2011 (USGS, 2021). None of these events were correlated with USGS-mapped faults (USGS, U.S. Quarternary Faults, 2019c) (Figure 47). It is difficult to ascertain the exact regularity of natural microseismic events but recording for at least 1 month prior to injection should provide enough natural baseline and ensure the array is adequately tested with locatable events. This was demonstrated at the Illinois Basin Decatur CCS project (Smith & Jaques, 2016), which is also in a region of low natural seismicity, as roughly three events were located per month prior to the start of injection. However, the exact timing for recording a microseismic baseline will be dependent on items such as array sensitivity assessment and drilling and perforating timelines.

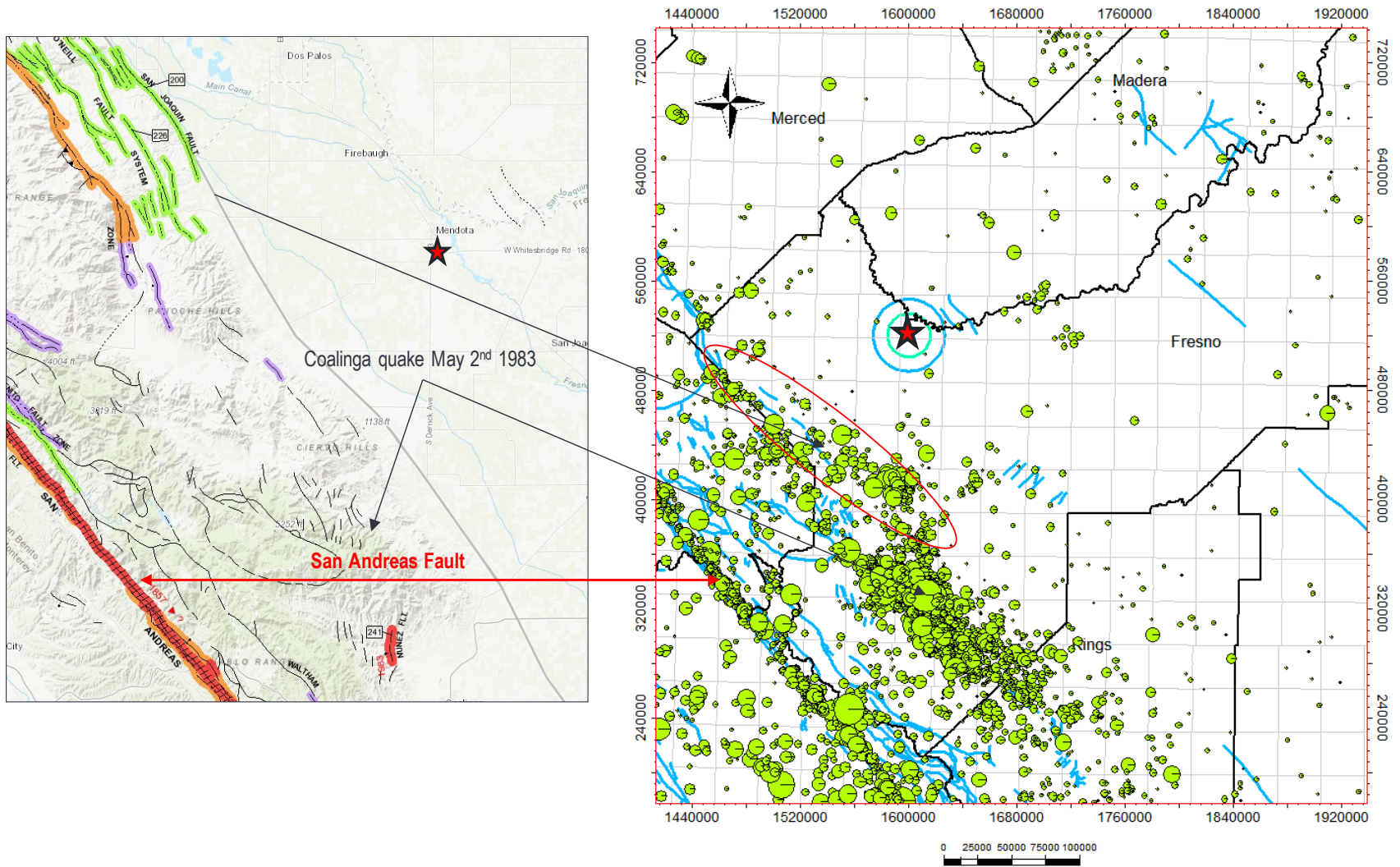


Figure 45. Regional faulting from the Department of Conservation (1998)(left) and quakes with magnitudes greater than 2.5 since 1900 (USGS, 2019a) (right). Red star represents the location of the Mendota site.

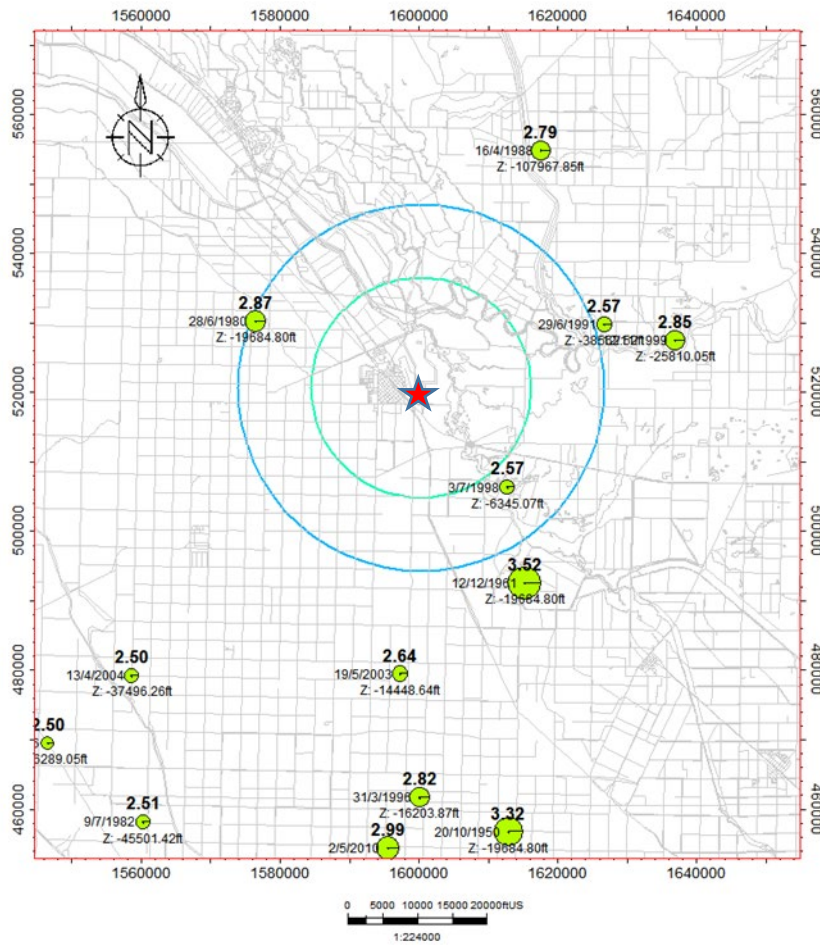


Figure 46. Historical earthquakes near AoR greater than 2.5 since 1900. Red star represents Mendota site.

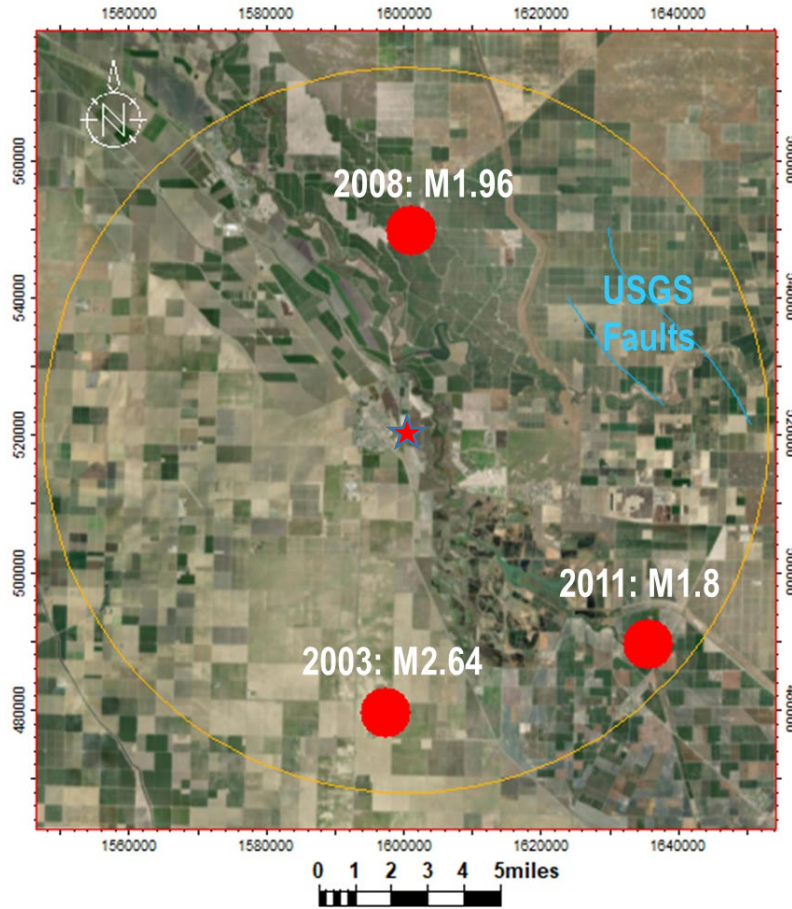


Figure 47. All earthquakes (red) located by the USGS Advanced National Seismic Survey within a 10-mile radius of the proposed injection site since 2000 with the year and magnitude shown. Faults provided by the USGS are also shown in blue with the 10-mile radius in orange. Red star represents Mendota site.

Table 6. Historical earthquakes near AoR greater than 2.5 since 1900. X and Y values are projected in California State Plane Zone IV, NAD27.

Date	Depth	Magnitude	X	Y
May 02 2010	-38857.8	2.99	1595566.51	454365.79
May 04 2006	-26289.05	2.5	1546520.09	469493.49
Apr 13 2004	-37496.26	2.5	1558657.91	479191.94
May 19 2003	-14448.64	2.64	1597294.84	479402.01
Nov 12 1999	-25810.05	2.85	1636938.66	527468.16
Jul 03 1998	-6345.07	2.57	1612726.91	506309.9
Mar 31 1996	-16203.87	2.82	1600123.78	461643.08
Jun 29 1991	-38562.52	2.57	1626716.98	529725.84
Apr 16 1988	-107967.85	2.79	1617588.21	554788.88
Jul 09 1982	-45501.42	2.51	1560285.29	458109.97
Jun 28 1980	-19684.8	2.87	1576493.55	530194.57
Dec 12 1961	-19684.8	3.52	1615274.11	492500.45
Oct 20 1950	-19684.8	3.32	1612875.91	456671.38

2.7 Hydrologic and Hydrogeologic Information [40 CFR 146.82(a)(3)(vi), 146.82(a)(5)]

2.7.1 Depth to the Deepest USDWs – 40 CFR 146.93(c)(1)(x)

USDW protection is a primary objective of any CCS project; to protect the USDWs, it is important to know how deep they are in the AoR. A USDW is defined as any formation that has formation water with less than 10,000 ppm total dissolved solids (TDS). At Mendota, this depth is estimated to be at 1,415 ft TVDSS. This depth was calculated by using the resistivity logs of five wells near the Mendota site. The resistivity image logs were digitized, and Archie's equation was used to estimate the resistivity of the water (R_{wa}) using standard parameters and a porosity of 0.35 p.u. R_{wa} was then converted to an estimated water salinity.

Matheson 1 and Amstar 1, 0.5 miles and 1.5 from the Mendota site, respectively, had resistivity logs above the estimated base of freshwater (BFW) recorded in the California Division of Oil, Gas and Geothermal Resources (DOGGR) well data sheets (Figure 48) (DOGGR, 2019). DOGGR (now CalGEM) defines BFW as less than 3,000 ppm salinity. There is reasonable agreement of water salinity around 3,000 ppm for the estimated BFW of Matheson 1 and Amstar 1. The calculated water salinity indicates the base of USDW for the five wells near Mendota between 1,200 to 1,415 ft TVDSS. Because the estimation is based on log calculations, there is some uncertainty, which will be resolved when data becomes available from the drilling of a characterization well. The largest uncertainties in the water salinity estimate are formation porosity, Archie equation parameters, and the effect of clay that may be present. Using a lower estimated porosity would raise the estimated water salinity whereas clay may reduce the estimate. The USDW will need to be verified by acquiring samples from the characterization well. The water salinity estimates for the three wells closest to the proposed Mendota_INJ_1 site are shown in Figure 49.



Figure 48. Wells used to calculate the depth to the deepest USDW.

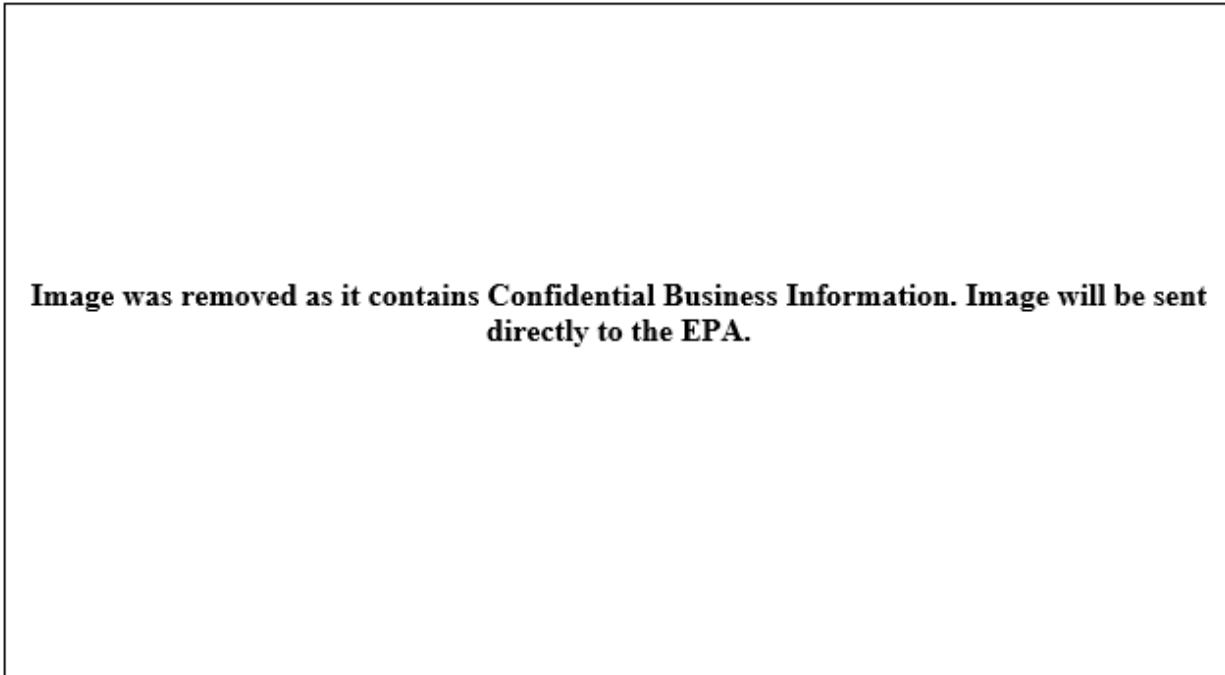


Figure 49. CONFIDENTIAL BUSINESS INFORMATION: USDW estimated using resistivity measured in wells near the Mendota site. This image displays IHS data (IHS, 2019), and it is marked as Confidential Business Information.

Additionally, the California Oil & Gas Fields field data sheets published for nearby fields show formation water salinity information for some formations and estimated BFW for the field. The published water salinity for the Eocene and Cretaceous formations generally ranges between 17,100 and 26,500 ppm. The exceptions are the Jergins formation at Cheney Ranch and Blewett formation at Merrill Ave. The Jergins and Blewett formations are in the Moreno formation and have published salinities of 8,500 and 15,000 ppm, respectively. The wells near the Mendota site do not show lower water salinities based on the resistivity response for sands in the Moreno formation but have been identified as a potential risk. The salinities for permeable formations near the Moreno formation will need to be verified by sampling in the characterization well.

Formation water samples will be collected (when water is present) during the drilling of the injection and monitor wells. The newly acquired resistivity log data will be compared to the other well data available in the area. Water samples will be collected within the Jergins and Blewitt formations (when water is present) and analyzed to confirm whether the formations are USDWs.

2.7.2 Local Near-Surface Groundwater

The characteristics of water wells and the piezometric elevation of the near-surface shallow groundwater was evaluated. Figure 50 shows the location of groundwater wells in the area (California Department of Water Resources, 2021). These wells include observation and

irrigation wells. At the proposed Mendota_INJ_1 location, the depth to the deepest USDW is estimated to be ~1,609 ft BGS (~1,415 ft SSTVD; Section 2.7.1); this is 7,165 ft above the top of the Second Panoche injection formation.

There are 79 water wells within a 2.5-mile radius of the proposed Mendota_INJ_1 location. These wells range in depth from approximately 20 ft to 550 ft MD. The recorded water levels were filtered by most recent recorded groundwater level measurement to determine an approximate piezometric elevation surface, as the dataset does not denote depth of individual aquifers. The data do provide a reasonable representation of shallow groundwater elevation and flow direction shown in Figure 51. The San Joaquin River flows from north to south and is 0.6 miles east of the site. At this time, understanding of local aquifers is limited. In future phases of this project, a more detailed evaluation of surface groundwater will be completed.

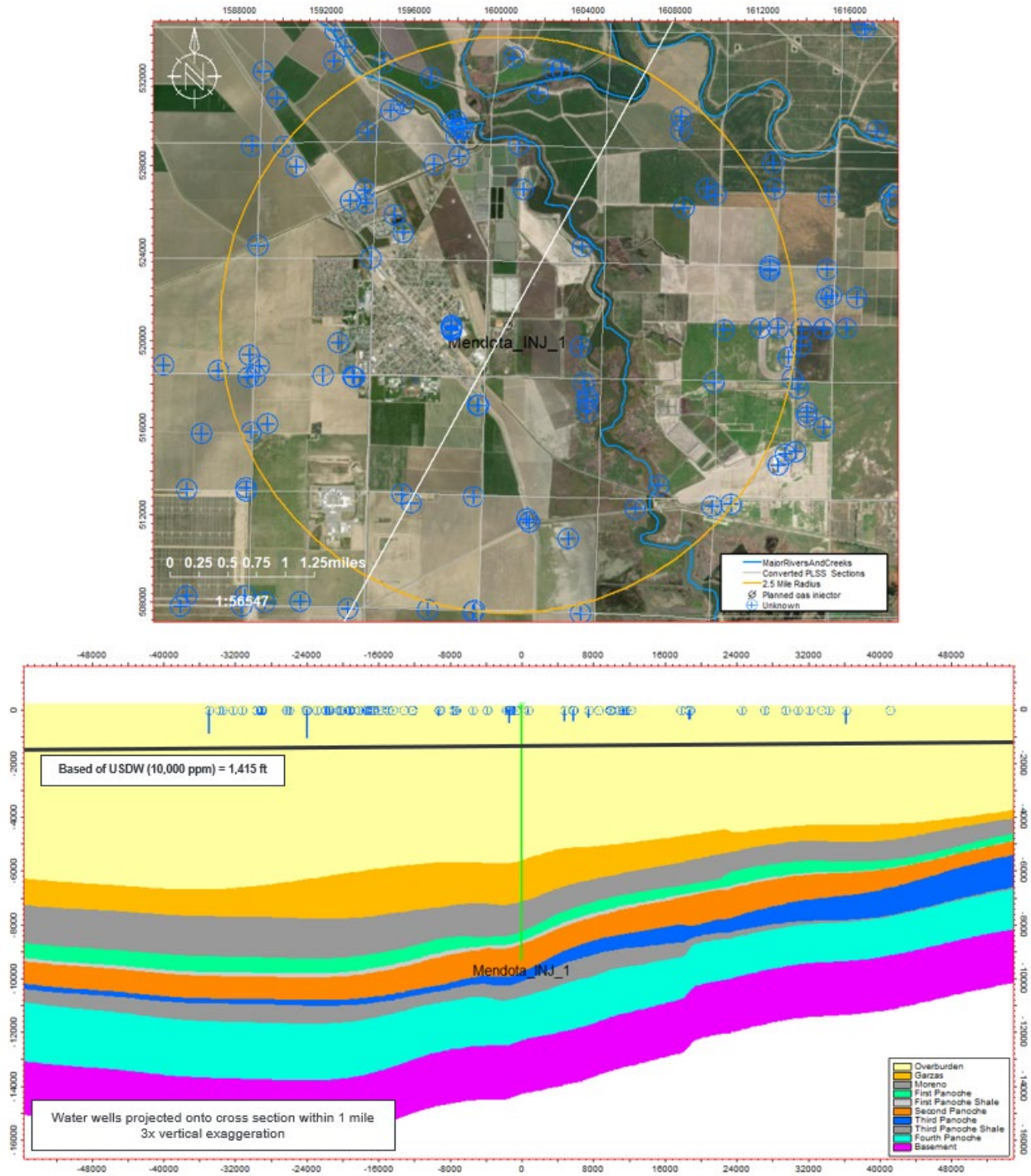


Figure 50. Map of water wells and cross section depicting water wells and elevation of lowermost USDW. The vertical distance from the First Panoche sandstone to the calculated lowermost USDW (1,415 ft TVDSS).

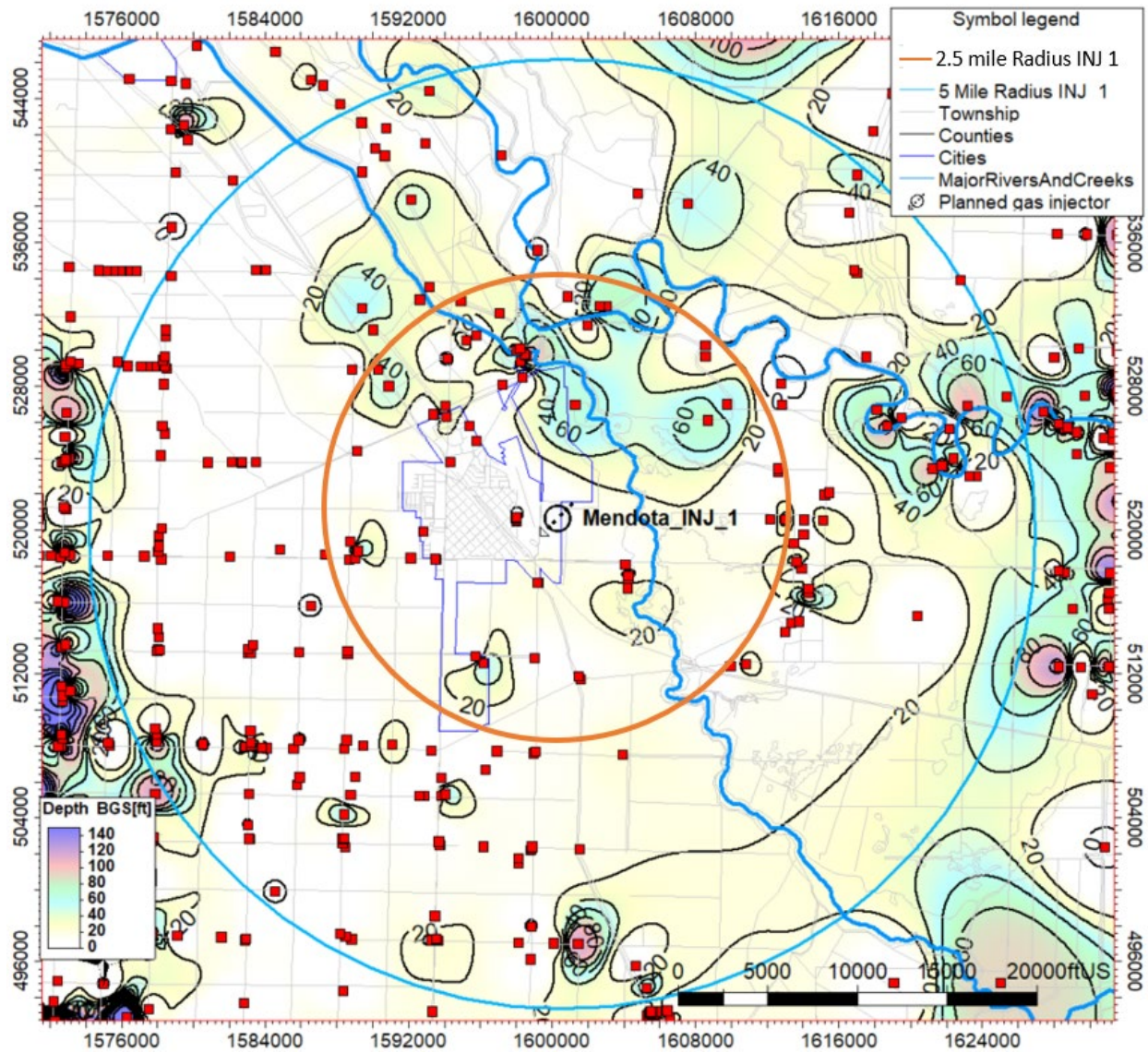


Figure 51. Potentiometric map of the approximate shallowest groundwater surface.

2.8 Geochemistry [40 CFR 146.82(a)(6)]

2.8.1 Characteristics of Injection Zone Formation Water

There was no available formation water information in the target Panoche sands at the proposed storage site; however, several oil and gas fields nearby produced from the Cretaceous Panoche formation and overlying formations; providing salinity of the formation waters and related information. Available data on water quality consists of fluid samples from the wells near the proposed site; these data are listed in Table 7. Salinity is taken from California Department of Conservation (1998). That report does not provide the well IDs or the perforation depths (water sample depth). In Table 7, formation depths are likely average depths of the geologic units from which water samples were obtained and are from a DOGGR report (DOGGR, 1992). The average depths may be somewhat different from the perforation depths of the wells from which the formation waters were sampled. Perforations and BFW (3,000 ppm) were recorded as part of USGS study (Davis, Bennett, Metzger, & al., 2018), Table 8 shows well top perforation and BFW recorded from the Gill Ranch field as part of this study. Although not specified by the publicly available data, it is assumed that water samples come from the perforation interval.

Table 7. Salinity of the formation waters from the oil and gas fields near the proposed Mendota site (California Department of Conservation, Division of Oil, Gas and Geothermal Resources, 1998).

County	Field	Formation	Depth (ft)	Salinity (ppm)	TDS (ppm)
Fresno	Raisin City	Miocene	5,080	44,000	44,200
Fresno	Moffat Ranch	Eocene	3,900	26,500	—
Fresno	Gill Ranch	Eocene	4,430	25,700	42,000
Fresno	Raisin City	Eocene	8,450	22,300	22,500
Fresno	San Joaquin	Eocene	7,000	21,100	
Fresno	Cheney Ranch	Moreno	7,000	8,500	14,000
Fresno	Gill Ranch	Panoche	5,850	20,000	20,900

Table 8. Gill Ranch wells from USGS study, showing top perforation and BFW (3,000 ppm) (Davis, Bennett, Metzger, & al., 2018) (CalGEMS, 2020).

API	Field	Type	Perforation Top (ft)	Base of Fresh Water (ft)
03900040	Gill Ranch Gas	Dry Hole	N/A	850
03900047	Gill Ranch Gas	Dry Hole	4,305	650
03900052	Gill Ranch Gas	Waste Disposal	3,240	937

03900053	Gill Ranch Gas	Gas Storage	4,435	871
03900057	Gill Ranch Gas	Waste Disposal	3,250	965

The Gill Ranch gas field is approximately 6.5 miles northeast of Mendota. There are wells that penetrate through the Fourth Panoche sand and the basement at about 9,000 ft. Salinity of the formation water from the First Panoche sand is 20,000 ppm (NaCl). The TDS of 20,900 ppm is close to salinity, suggesting Na- and Cl-dominated water chemistry. Salinity from the rest of the Upper Cretaceous is like that of the Panoche formation. The Panoche formation is also penetrated at the Moffat Ranch gas field 8.5 miles north of Mendota; however, no water chemistry data are available. The formation water from the Gill Ranch field is likely similar to that of the Mendota site as they share similar initial pore water (seawater) during deposition and similar pore water evolution; however, the lateral continuity of the sandstones between these sites is uncertain, and they may have discontinuous hydrologic systems. The sandstones at Gill Ranch are located updip and could be deltaic whereas those near the injection location are expected to be turbidites on the slope. There is a greater possibility of meteoric water infiltration into the sandstones updip and dilution of the pore water during the burial history, which indicates higher salinity at the injection site downdip. Regionally, salinity tends to increase to the west away from the recharge area (Gillespie, Kong, & Anderson, 2017), which also indicates a slightly higher salinity (around 25,000 ppm) in the Panoche formation at the injection site.

Salinity in the Eocene at the Gill Ranch field is reported as 25,700 ppm and 26,500 ppm at Moffat Ranch field, which is somewhat higher than that of the Panoche formation water in those fields. TDS in the Eocene is much higher, at 42,000 ppm, at Gill Ranch, suggesting a significant change of water chemistry. The Miocene Zilch formation has higher salinity 44,000 ppm (NaCl) at the Raisin City oil field, which is 16 miles southeast to Mendota. TDS is reported at 44,200 ppm, suggesting Na- and Cl- dominated water composition. The Cheney Ranch gas field, approximately 12 miles southwest of Mendota, reports formation water salinity of 8,500 ppm and TDS of 14,000 ppm in the Jergins sand at the bottom of the Moreno formation. Because the Cheney Ranch field targets the Jergins sandstone overlying the Panoche formation in the Moreno formation, it is uncertain whether the data point, which shows significantly lower salinity, is representative of the Panoche formation at the proposed Mendota_INJ_1 site.

Review of the resistivity logs from wells in the AoR do not indicate a sand with formation water fresher than the Panoche formation, but it has been recognized as a potential risk. The planned testing program for the characterization well includes formation water sampling for the Panoche and overlying sands (Schlumberger, 2021g). Fluid samples from the injection zone are required to confirm the formulation fluid chemistry.

2.8.2 Mineral Composition of the Injection Zone

The Cretaceous Panoche formation sandstones are the target CO₂ sequestration storage zones (between 7,000 and 10,000 ft), with the overlying Moreno shale acting as a confining seal. The Panoche formation consists of deep-marine shale and submarine fan deposit intervals (McGuire,

1988). A core description was available for the interval 11,422 to 11,471 ft corresponding to the Fourth Panoche sand in the B.B. Co 1 well, which is within 2.5 miles of the proposed storage site. Conglomerate and sandstones are identified in the core. The sandstones are mostly composed of fine- to coarse-grained, poorly sorted quartz and feldspar grains and locally well cemented by calcite. Biotite is abundant with small amounts of chlorite and muscovite. Trace amounts of pyrite are also present. Both tuff interbeds and tuffaceous matrix are noted in the sandstone below 11,430 ft. Weathered volcanic rock fragments are also noted and likely contain abundant feldspar minerals and quartz. Based on the core description, a generalized mineral composition of the sandstones is proposed for geochemical modeling (Table 9).

Table 9. Estimated mineral composition (wt.%) for the Panoche formation used in geochemical modeling.

Quartz	K-feldspar	Plagioclase	Calcite	Pyrite	Muscovite	Chlorite	Illite	Kaolinite
60	10	15	4.5	0.5	2	2	6	Trace

2.8.3 Composition of the Injectate

The gas stream for injection will contain 96.78% CO₂ with some impurities (Table 10). O₂ is the most notable impurity at 1.15% because it is reactive when redox-sensitive minerals are present in the formation. It also requires surface and well components, which are resistant to that environment. To understand its effect, O₂ is included in the geochemical models.

Table 10. Composition of the injectate (mass fractions).

Component	Mass Fraction
H ₂ O	0.002245
O ₂	0.011536
H ₂	0.000164
N ₂	0.001475
CO	0.005322
CO ₂	0.967834
Ar	0.01119
NO	9.01E-05
NO ₂	9.03E-08
H ₂ S	0.000144
NH ₃	1.93E-10

2.8.4 Geochemical Modeling Setup

Geochemical modeling was conducted using the React module of Geochemist's Workbench* version 12 software and the resident thermo database to predict the reaction paths between the rock-forming minerals, the formation water, and injectate. A solution of 25,154 mg/kg TDS was

constructed by equilibrating a NaCl solution with minerals (quartz, K-feldspar, albite, calcite, illite, kaolinite, muscovite, and chlorite) in the React module of Geochemist’s Workbench (Table 11). Initial pH in the models was set to neutral. Mineral composition used in the models was estimated from the core description of the B.B. Co. 1 well (Table 9). The mineral reaction rate constants from Palandri and Kharaka (2004) were applied to the models. CO₂ and O₂ with a ratio of 100:1 were added into the system. The modeling was set at 70°C and run for 5 years. Changing the simulation duration did not alter reaction paths.

Table 11. Chemical composition of the initial solution for geochemical modeling.

Element	Concentration (mg/kg)
Al	0.00553
Ca	0.183
Cl	13,300
Fe	0.0355
H	1.09
HCO ₃	2,340
K	63.8
Mg	0.839
Na	9,440
SO ₄	20
SiO ₂ (aq)	29.1
TDS	25,154

2.8.5 Simulated Reaction Pathways

CO₂ dissolving into the brine produces carbonic acid, which dissociates into bicarbonate and carbonate ions, HCO₃⁻ and CO₃²⁻ and lowers the brine pH. A series of mineral reactions are initiated from the drop of pH. The results show several minerals (e.g., calcite, pyrite, albite, K-feldspar, and illite, in a decreasing order in the amount of dissolution) are dissolved, whereas others (e.g., anhydrite, quartz, hematite kaolinite, muscovite, and dolomite, in a decreasing order in the amount of precipitation) precipitate in the simulation (Figure 52). The dominant mineral reactions include dissolution of calcite, pyrite, albite, illite, K-feldspar, and chlorite (chamosite). Correspondingly, the components in the solution also evolve along the simulation process (Figure 53). The dominant change is increasing HCO₃ concentration with slight increases in H⁺, Ca, SO₄, and SiO₂(aq) and slight decreases in Mg, Cl, Na, and K.

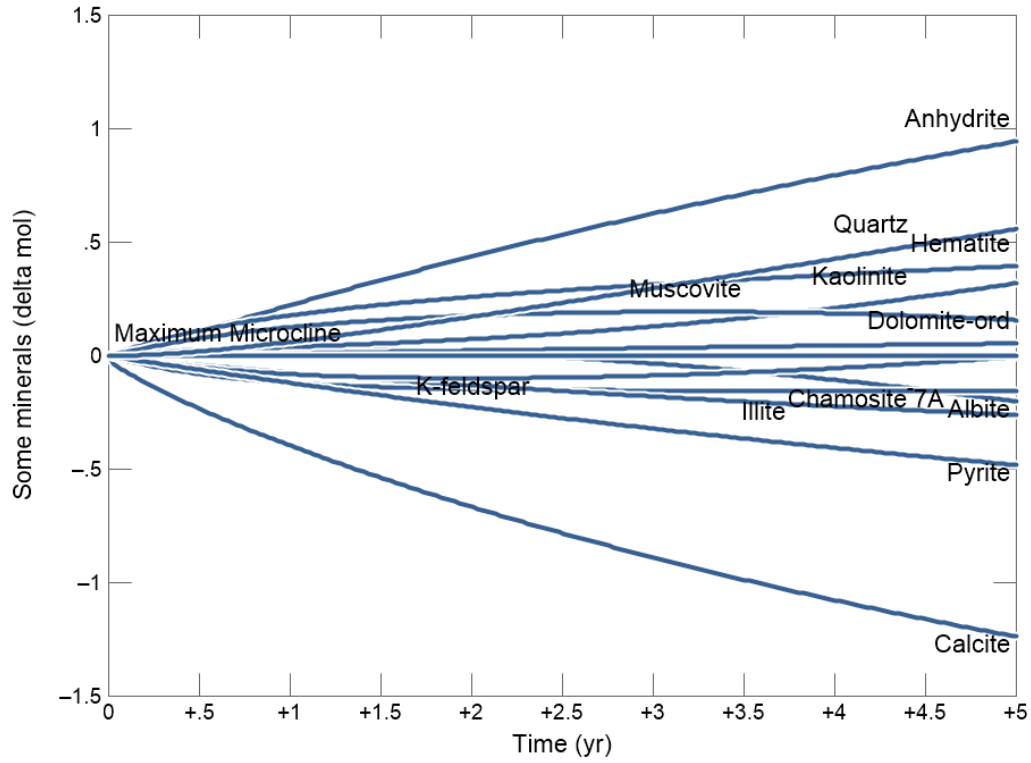


Figure 52. Changes of the amount of the minerals from the addition of CO₂ and O₂ in geochemical modeling.

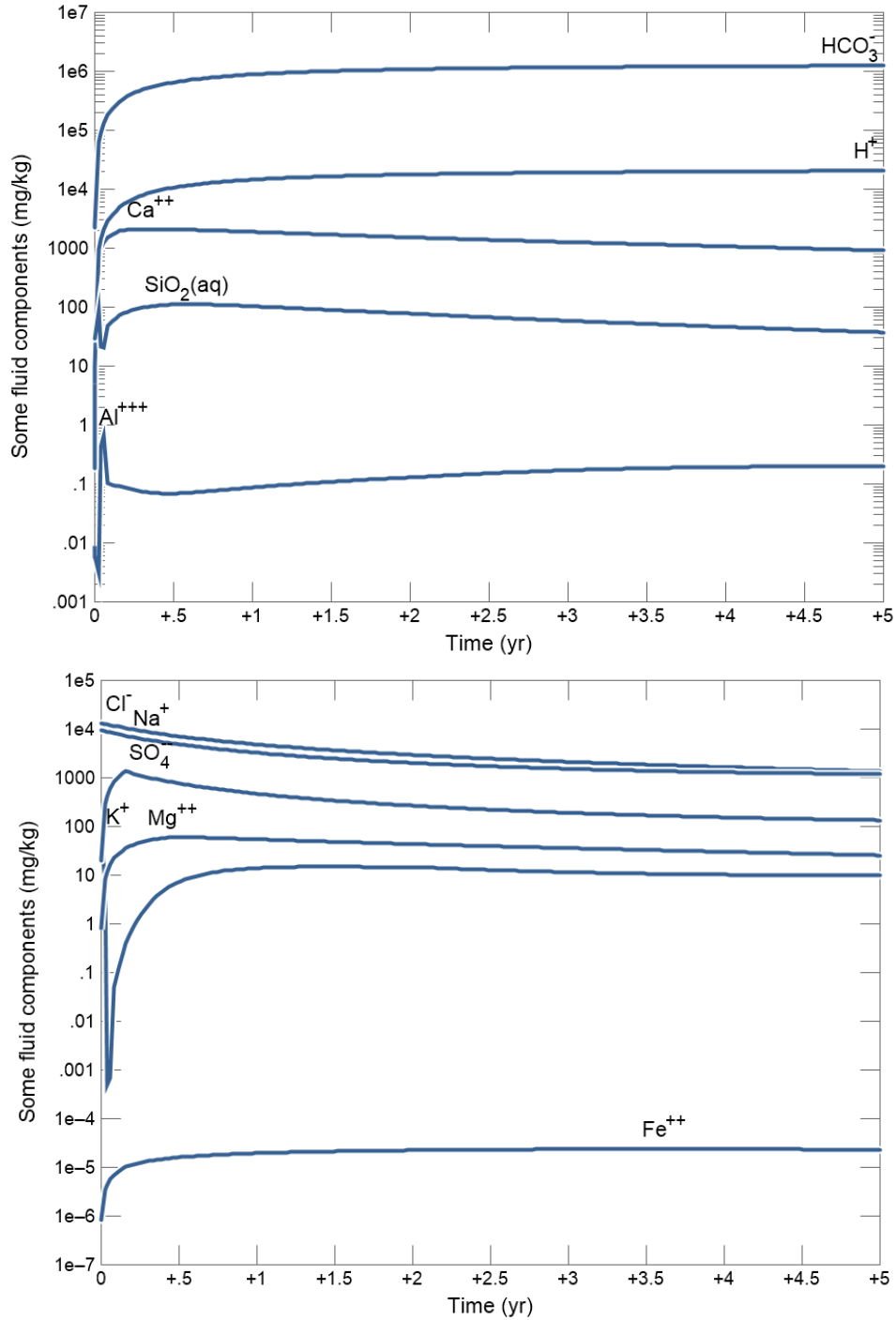
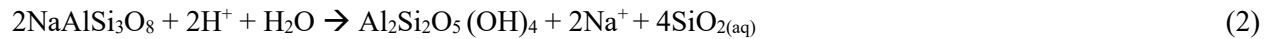


Figure 53. Aqueous composition after the addition of CO₂ and O₂ in geochemical modeling.

Simulation results of the combined mineral and aqueous phases and the major mineral reactions are listed below:



The most prominent mineral reaction initiated by the addition of CO₂ is calcite dissolution (Equation 1), which releases Ca into the solution. As a similar response to the decreasing pH, K-feldspar and albite are dissolved, releasing K and Na into the solution (Equation 2 and Equation 3). Silica and kaolinite are the probable products of feldspar dissolution.

The co-injected O₂ as an impurity will have an impact if both redox-sensitive mineral species and ferrous iron-bearing minerals (pyrite, Fe-bearing carbonates, and possibly glauconite, which contains mostly ferric Fe but also some ferrous Fe) are present in the overlying formation. Specifically, pyrite, a common mineral phase in sedimentary rocks, is oxidized to release ferrous iron and sulfate (Equation 4). Ferrous iron is further oxidized into ferric iron and precipitate as hematite (Equation 5). Both reactions will further reduce pH. The increasing SO₄ concentration from pyrite oxidation may lead to formation of anhydrite (Equation 6), gypsum, and/or barite when enough Ca and Ba are present in the solution.

Overall, the amounts of mineral reactions are limited by the availability of the reactive mineral phases and the extent of the space and time where the injectate and water co-exist. The latter is controlled by flow properties and injection dynamics. Sedimentary texture is also an important factor that determines specific surface area of each mineral component exposed to the pore water. The contact area between the reactants and solution determines the reaction rate.

The simulation results show net reduction of the rock mass and volume (Figure 54), indicating increased porosity. However, predicting permeability change is difficult because it is also affected by the morphology and site of the precipitated material. For example, the newly formed iron oxides may preferentially block the pore throat, which will reduce permeability even if there is a net increase of porosity from mineral dissolution. Autoclave CO₂-water-rock reaction experiments can be conducted with core and water samples taken from the injection zone. The core samples can be analyzed before and after the experiments to quantify the effects of mineral reactions on the flow and geomechanical properties. Aqueous chemistry data from the experiments will be used to calibrate geochemical modeling.

Generally, pyrite and other redox-sensitive minerals are not abundant in sandstones, which limits the extent of precipitation of iron oxide and sulfate minerals. Calcite dissolution usually increases porosity and permeability, which is beneficial for injection operation. The framework grains of the sandstones are predominantly quartz, which is not as reactive and will preserve the geomechanical strength of the formation.

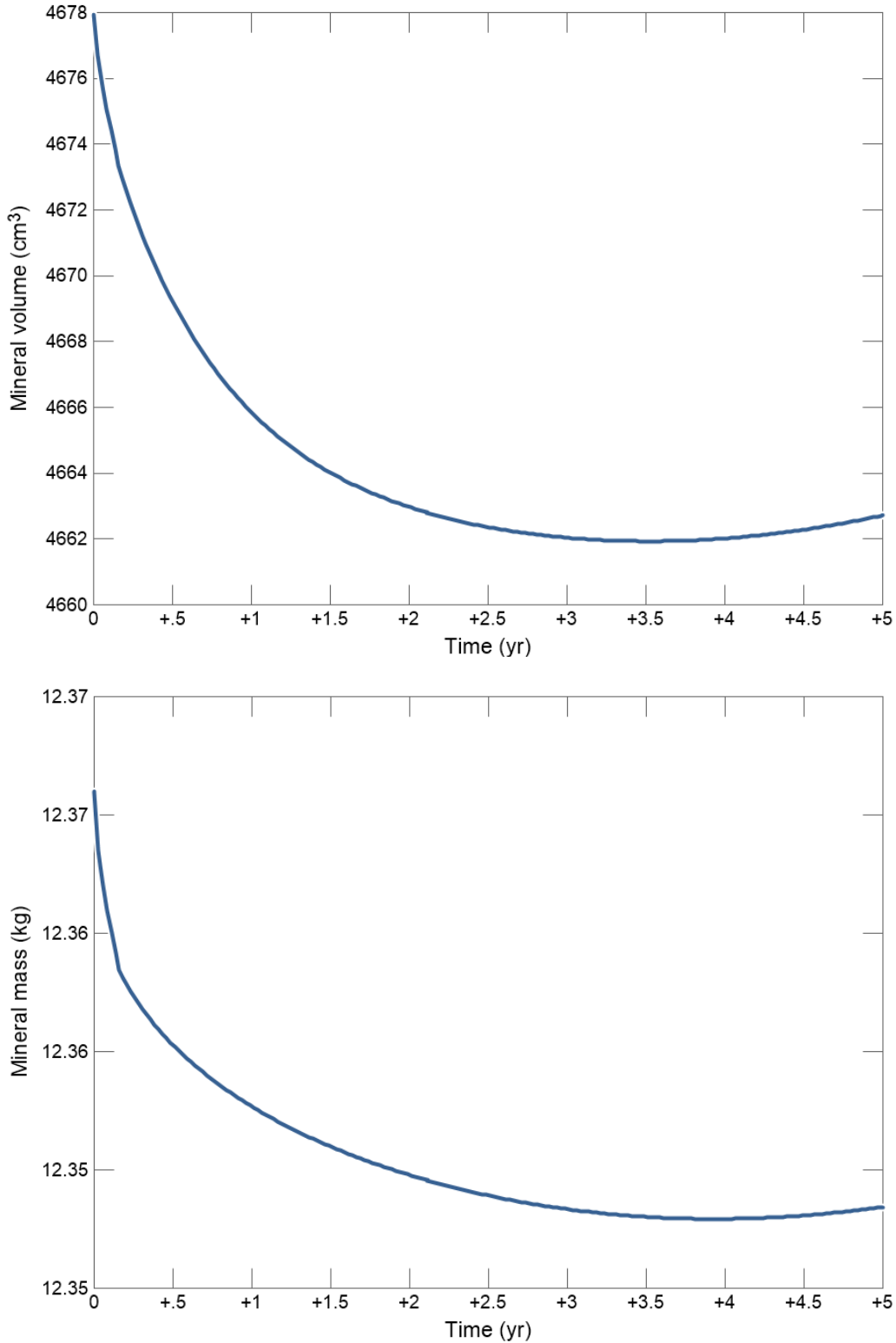


Figure 54. Mineral volume and mass after the addition of CO₂ and O₂ in the geochemical modeling.

2.9 Other Information (Including Surface Air and/or Soil Gas Data, if Applicable)

At the time of this preconstruction application, surface air and soil gas data have not been collected. Baseline data will be designed in future phases of this project.

2.10 Site Suitability [40 CFR 146.83]

The location of the Mendota_INJ_1 well is in a favorable setting for a CO₂ sequestration project based on the initial site characterization during this preconstruction phase.

Based on the interpretation of well tops and 2D seismic data, the distribution of the sandstones of the Second Panoche injection zone is interpreted to be relatively continuous within the AoR (Section 2.2). The regional dip of this and other formations is to the southwest; this implies that the injected CO₂ will migrate approximately 2 miles to the northeast (Section 3).

The gas stream for injection contains 96.78% CO₂ with some impurities. O₂ is the most notable impurity at 1.15% because it is reactive when redox-sensitive minerals are present in the formation (Section 2.8). Generally, pyrite and other redox-sensitive minerals are not abundant in sandstones, which limits the extent of precipitation of iron oxide and sulfate minerals. Calcite dissolution usually increases porosity and permeability, which is beneficial for injection operation. The framework grains of the sandstones are predominantly quartz, which is not as reactive and will preserve the geomechanical strength of the formation. The injection and monitoring wells are planned to be constructed with components made of CO₂-resistant materials, which include casing, cement, packers, safety valves, etc., and will consider gas stream impurities.

Reservoir simulations show that the injected CO₂ will be confined to the Second Panoche injection zone by the low-permeability shales of the First Panoche shale. Above this, the First Panoche sand provides secondary containment with the overlying regionally extensive Moreno shale.

There are no wells in the AoR that penetrate the Moreno shale (secondary confinement layer). There are two wells within a 2.5-mile radius of Mendota_INJ_1 (BB Co 1 and Amstar 1) that do penetrate the Moreno shale and may require remediation. Final remediation plans for these wells will be informed by updated plume simulations after site-specific data are acquired. Attachment B: Area of Review and Corrective Action Plan (Schlumberger, 2021b) details the potential corrective action plan for wells near the AoR that penetrate the Moreno shale.

The total pore volume of the Second Panoche injection zone was calculated by using the 3D geocellular model with a 2.5-mile radius around the proposed Mendota_INJ_1; the P50 storage capacity in the Second Panoche was calculated to be 41.58 million tonnes (Section 2.4.3, Table 5). Given the high porosity and permeability of the Second Panoche, this formation is suitable to receive the forecasted 350,000 tonnes/year of CO₂ for the proposed 20-year injection period.

Currently, there are no potential concerns regarding the confining zone integrity. The zones are relatively continuous, and the faults interpreted from 2D seismic data near Mendota_INJ_1 show only minor displacement. 3D seismic data acquisition (discussed in Section 2.4.4) will result in

greater certainty regarding spatial extent of faulting as well as the continuity and seal integrity of the First Panoche shale confining zone.

Using the First Panoche sand and Moreno Shale as a secondary confining zone places the deepest USDW (calculated at 1,415 ft TVDSS, see Section 2.7.1) 5,700 ft above the Moreno shale, allowing over a mile of USDW protection in case of seal integrity loss in both the First Panoche shale (primary confining zone) and Moreno shale (secondary confining zone) (Schlumberger, 2021e). The Moreno shale thickness (~1,100 ft, Figure 14), lateral extent, and relatively low porosity and permeability (Figure 33 and Figure 34) will provide very low leakage risk to the much shallower USDW.

During future phases of this project, if approved by the EPA, additional data will be gathered and assimilated into an updated reservoir characterization. The site structural geology will be accurately delineated when there is a 3D seismic survey available. After a characterization well is drilled, petrophysical, geomechanical, fracture, and geochemical properties will be much better understood. Baseline monitoring of groundwater, soil, and air will also be completed in future phases of the project.

3. AoR and Corrective Action

AoR and Corrective Action GSDT Submissions

GSDT Module: AoR and Corrective Action

Tab(s): All applicable tabs

Please use the checkbox(es) to verify the following information was submitted to the GSDT:

- Tabulation of all wells within AoR that penetrate confining zone [40 CFR 146.82(a)(4)]
- AoR and Corrective Action Plan [40 CFR 146.82(a)(13) and 146.84(b)]
- Computational modeling details [40 CFR 146.84(c)]

The above requested documents have been included in the file submission (Schlumberger, 2021b). These documents address the rule requirements for the above EPA citations.

4. Financial Responsibility

Financial Responsibility GSDT Submissions

GSDT Module: Financial Responsibility Demonstration

Tab(s): Cost Estimate tab and all applicable financial instrument tabs

Please use the checkbox(es) to verify the following information was submitted to the GSDT:

- Demonstration of financial responsibility [40 CFR 146.82(a)(14) and 146.85]

The above requested documents have been included in the file submission (Schlumberger, 2021h).
These documents address the rule requirements for the above EPA citations.

5. Injection Well Construction

The proposed injection well, Mendota_INJ_1 (Figure 55), will be a new vertical well that will be drilled with inclination of less than 5°. In this description, all hole and casing depths reference ground level. The conductor will be driven if soil samples permit; however, if not, a 26-in-diameter hole will be drilled to a depth of 86 ft. A 22-in 197.41-lb/ft conductor pipe will be inserted and cemented to surface. A 20-in-diameter hole will be drilled to a depth of 1,800 ft to cover the maximum USDW depth at 1,609 ft. The well will be logged from 86 to 1,800 ft, and a 16-in 84-lb/ft casing will be run into the hole and cemented to surface. A cased-hole cement evaluation logging suite will be run. A 14 3/4-in-diameter hole will be drilled to a depth of approximately 7,432 ft, which should be 100 ft into the top of the Moreno shale, the main seal. Well logs to provide formation properties and any needed formation sampling will be run from 7,432 ft to 1,800 ft. A 10-3/4 in 55.5-lb/ft N-80 string of casing will be run into the hole and cemented to surface. Cement and casing evaluation logs will be run. A 9-5/8 in-diameter hole will be drilled to a depth of about 10,412 ft, which should be 100 ft into the top of the Third Panoche shale with whole cores taken over the Moreno shale and First and Second Panoche sands and shales. If a competent formation to set casing is found above the Third Panoche shale, then the 9-5/8-in hole may not be drilled to 10,412 ft. The well will have extensive logging and sampling suites run from 10,412 ft to 7,432 ft to fully evaluate the Panoche sands for injection and shales for seals. A 7-in 38-lb/ft T-95 Type 1 casing will be run from 0 to 7,332 ft, and then a 7-in 38-lb/ft T95 13Cr casing will be run from 7,332 ft to 10,412 ft and cemented to surface. Cement and casing evaluation logs will be run along with baseline monitoring logs. After the cased-hole logs are run, the well will be perforated and completed with an injection packer and 3-1/2 in L-80 13Cr tubing string. The perforation interval will be selected based on the log analysis but is anticipated to be centralized around 9,437 ft. Figure 56 and Figure 57 show the pore pressure, fracture, and temperature gradients used for the well construction planning.

The base of the USDW aquifers are calculated to extend to a depth of 1,609 ft TVD. The surface casing planned depth is 1,800 ft. The 16-in 84-lb/ft N-80 casing with watertight connections in a generous 20-in fully cemented hole to surface provides sufficient protection and coverage of the USDW aquifers.

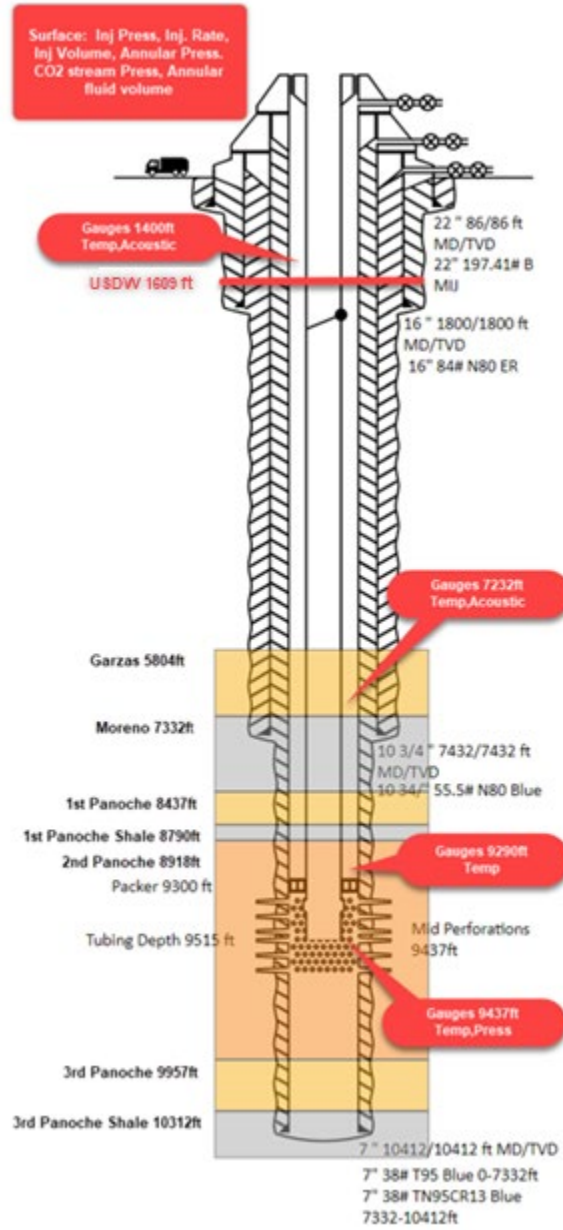


Figure 55. Mendota_INJ_1 well construction diagram.

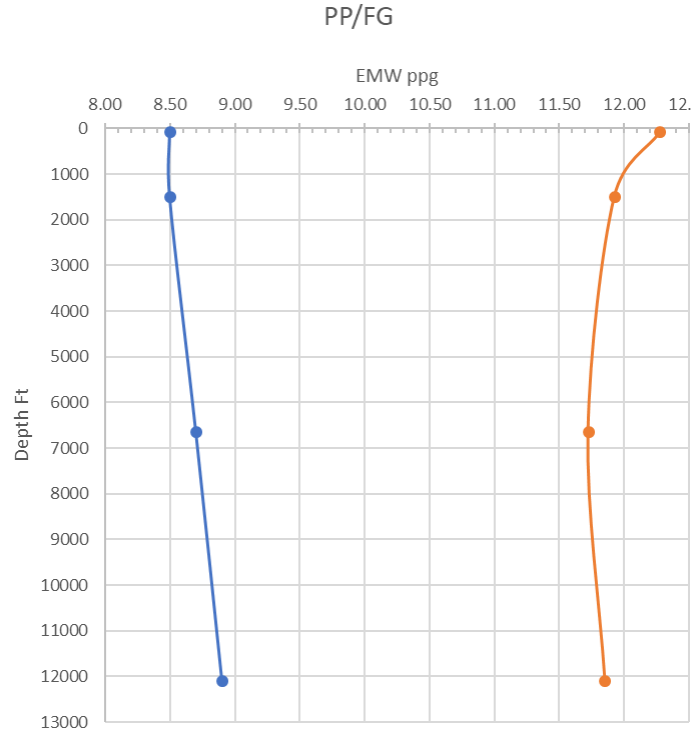


Figure 56. Pore and fracture gradients used for well construction.

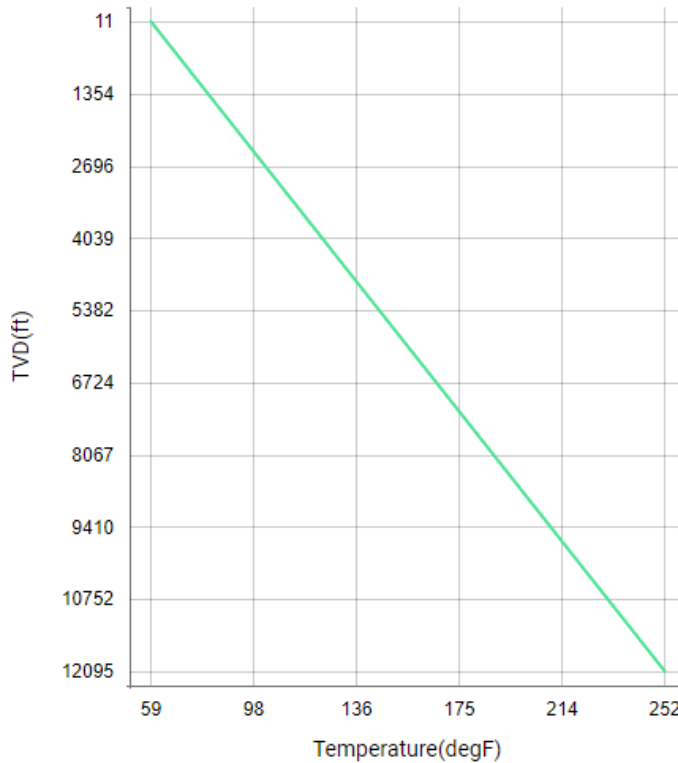


Figure 57. Temperature gradient used for well construction.

5.1 Proposed Stimulation Program [40 CFR 146.82(a)(9)]

Currently, there are no plans for stimulation at Mendota_INJ_1.

5.2 Construction Procedures [40 CFR 146.82(a)(12)]

5.2.1 Surface Wellhead Configuration

Surface wellhead will be configured for appropriate CO₂ service for those flow paths that will interact with the CO₂ injection stream or during well maintenance (Figure 58).

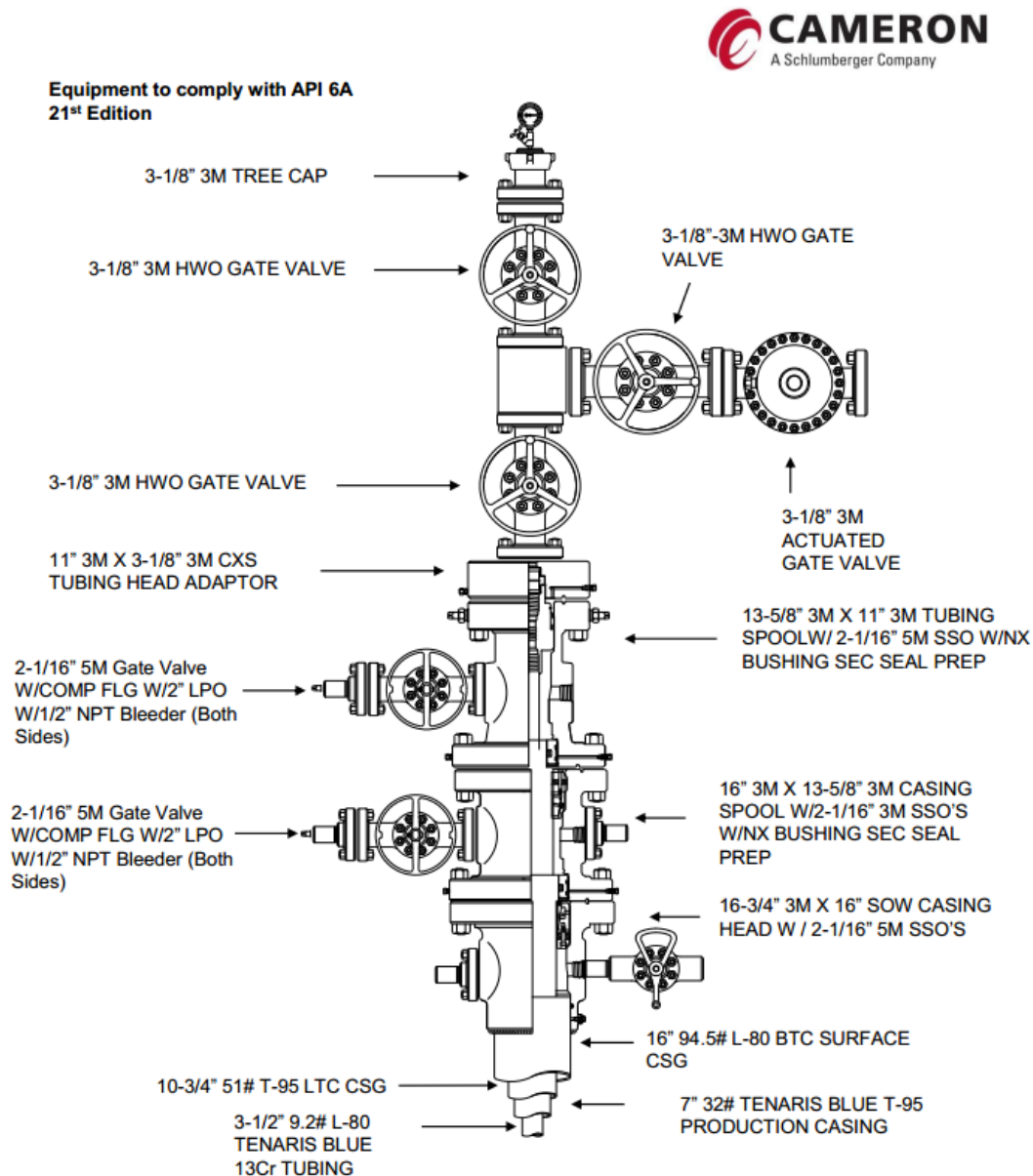


Figure 58. Surface wellhead configuration.

5.2.2 Casing

Casing selection has been evaluated against industry-standard worst-case loads to determine if selected casing sizes, material thickness, and grade are suitable for the environment in terms of pressure and temperature they will be subjected to (Table 12, Table 13). Where applicable, special loads were created to determine if the casing could handle a load not covered by current standards. Areas evaluated are casing/tubing burst, collapse, and axial and compressive strengths in unilateral, bilateral, and triaxial (Von Mises) load scenarios.

Figure 55 shows the position of the various casing, tubing, and perforations to be implemented in the Mendota_INJ_1 injection well. Correlation of the formations covered with casing and cement. Table 14 presents the various hole segments and purpose. Table 15 indicates the casing specifications and limitations.

Table 12. Casing design factors.

Burst	Collapse	Tension	Compression	VME
1.10	1.10	1.60	1.20	1.25

Table 13. Casing design loads.

String	Burst	Collapse	Tension	Compression	Von Mises
22-in Conductor	1.63	52.26	6.98	>100	1.75
16-in Surface	2.16	1.23	9.65	11.91	2.30
10 ¾-in Intermediate	1.34	1.84	3.00	3.58	1.34
7-in Long	1.25	2.00	2.23	3.44	1.25
3 ½-in Tubing	1.94	1.65	2.41	3.71	1.41

Table 14: Mendota_INJ_1 openhole diameters and intervals.

Name	Depth Interval (ft)	Openhole Diameter (in)	Comment
Conductor	86	26	Will try to drive conductor (reason for 1-in wall thickness) but need to get soil samples to determine if viable; if not viable, will drill 26-in hole
Surface	1,800	20	1,800 ft will cover any potential freshwater aquifers and provide sufficient kick tolerance for the intermediate string. Length may vary slightly in locating a formation with sufficient strength to provide a competent casing shoe.
Intermediate	8,387	14.75	This string will be set 100 ft in the Moreno shale at 7,432 ft.
Long-string	10,412	9.625	Will drill across the First, Second, and Third Panoche sands and have casing shoe below the Third Panoche shale (may be set in the above the Third Panoche shale if the formation is found suitable to set casing).

Table 15. Mendota_INJ_1 casing specifications.

Name	Depth Interval (ft)	Outside Diameter (in)	Inside Diameter (in)	Weight (lb/ft)	Grade (API)	Design Coupling (Short or Long Threaded)	Thermal Conductivity @ 77°F (BTU/ft hr, °F)	Burst Strength (psi)	Collapse Strength (psi)
Conductor	86	22	21	197.41	B	Welded	26.13	2,440	1,950
Surface	1,800	16	15.01	84	N80	Long	26.13	4,330	1,480
Intermediate	7,432	10.75	9.760	55.5	N80	Long	26.13	6,450	4,020
Long-string	7,332	7	5.920	38	T-95 Type 1	Long	26.13	12,830	13,430
Long-string	10,412	7	5.920	38	TN 95Cr13	Long	14.92	12,830	13,430

5.2.3 Discussion on Well Construction

Well construction will provide three casing barriers with generously cemented annuluses covering the USDW from surface to 1,800 ft. Covering the USDW will be the 16-in, 10-³/₄-in, and 7-in casings.

A removable 3-¹/₂-in tubing string with a retrievable seal bore packer will be used to facilitate easy movement and changeout of the tubing string and allow for fluid movement and pressure testing as needed. The tubing string will be fitted with nipple profiles to facilitate testing of the tubing, packers, and tubing annulus. Pressure and temperature monitors will be installed downhole as well as at surface on the various annular ports for the casing wellhead and tubing to keep track of variations of those parameters.

Although the offset wells did not indicate any major drilling issues in their available drilling logs, it is always good to be prepared with contingencies. Water-based muds (NaCl gelled) will be used for drilling the entire well limiting contamination in any aquifers from the drilling mud. Lost circulation will be addressed with materials such as fibers, hulls, and calcium carbonate. The nature of lost circulation material is not to penetrate the formation with any significant depth (< 3 ft but depends on porosity, surface fractures along wellbore, and size of lost circulation material) so damage to aquifers and other formations from lost circulation material will be very limited if any.

This is a vertical well, and risk for any fishing job for lost drillpipe or other fish in the hole will be minimal. In the event a fish must be left in the hole after a reasonable amount of time is dedicated to retrieve the fish, a cement plug will be placed above the fish, and sidetracking will be executed to go around the fish and back to vertical.

There are plans to take frequent deviation checks. It will be desirable to keep the wellbore as vertical as possible. The plan is to keep the well ≤ 5.0° inclination. If measurement-while-drilling (MWD) tools are not in the drilling assembly, then a drift indicator will be used with

surveys taken every 300-ft minimum. If MWD tools are not used to drill a well section, then a magnetic multishot will be dropped at the end of the section, and survey intervals of 100 ft will be taken as the final assembly is retrieved from the hole. At the end of the well, a gyro survey will be run to confirm the wellbore profile. MWD, magnetic multishot, and gyro surveys all provide three-dimensional surveys with depth, inclination, and azimuth outputs. Minimum curvature will be used to calculate the wellbore path between survey points.

All components used in the well construction will adhere to API, ASTM, ANSI, and NACE standards as referenced for that component. For example, casing is controlled by API 5C3, 5CT, and 5CRA for basic material control and dimensioning. ANSI/NACE MR0175/ISO 15156-2015 provides guidelines for corrosion control, and ASTM defines testing methods for the materials or tools.

Materials suitable for a CO₂ environment are clearly specified in API, ANSI/NACE, and ASTM standards. Suppliers of components will be required to demonstrate and provide certification that their equipment has been tested and evaluated against these standards and that they are suitable for purpose in the environment defined.

5.2.4 Tubing and Packer

Table 16 and Table 17 summarize the expected tubing and packer specifications for Mendota_INJ_1.

Table 16. Mendota_INJ_1 tubing specifications.

Name	Depth Interval (ft)	Outside Diameter (in)	Inside Diameter (in)	Weight (lb/ft)	Grade (API)	Design Coupling (Short or Long Thread)	Burst strength (psi)	Collapse strength (psi)
Injection tubing	9,430	3.5	2.992	9.2	L80Cr13	Long	10,160	10,540

Table 17. Mendota_INJ_1 packer specifications.

Packer Type and Material	Packer Setting Depth (ft BGS)	Length (in)	Nominal Casing Weight (lb/ft)	Packer Main Body Outer Diameter (in)	Packer Inner Diameter (in)
Seal Bore Packer in N80 S13Cr	93,00	64	38	5.685	4.0

Tensile Rating (lb)	Burst Rating (psi)	Collapse Rating (psi)	Maximum Casing Inner Diameter (in)	Minimum Casing Inner Diameter (in)
133.12@250°F	5,000	5,000	6.000	5.949

5.2.5 Cement

All casings will be cemented to surface. There are currently no known conditions preventing bringing cement to surface without a stage collar on the surface, intermediate, and long strings. All cement recipes will be evaluated with respect to properties and curing times in a laboratory before the job is started, and test samples from the actual slurry pumped will be evaluated. Coverage of the annulus and cement strength estimates will be achieved via a pumping schedule and associated pressures along evaluated with wireline cement bond log and ultrasonic cement evaluation logs.

5.2.5.1 Conductor

The conductor is expected to be driven but a provision has been allowed to drill a hole and grout cement the casing if soil conditions do not permit driving the casing to 86 ft.

5.2.5.2 Surface Section

The surface casing will cover the USDW aquifers at a maximum depth of 1,609 ft TVD. Surface casing depth is expected to be 1,800 ft. This is needed to provide a good kick tolerance for the intermediate section. Type II/V cement meets ASTM Specification C 150. It is a low-alkali Portland cement for general use and where high sulfate resistance is required (Table 18).

Table 18. Surface section fluid placement in annulus.

Fluid Name	Top MD ft	Bottom MD ft	Length ft	Volume bbl	Cement Sacks	Surface Density lb/gal
Drilling Fluid	0.0	0.0	0.0	0.0	—	9.00
Freshwater	0.0	0.0	0.0	40.0	—	8.32
12.4 ppg Lead Type II/V Cement	0.0	1,300.0	1,300.0	266.8	689	12.40
13.5 ppg Tail Type II/V Cement	1,300.0	1,800.0	500.0	69.9	286	13.50

5.2.5.3 Intermediate Section

The intermediate casing will be set 100 ft into the top of the capping formation for the Panoche sand, which is the Moreno shale. Cement will be brought back to surface from 7,432 ft TVD. Class G cement is an API grade cement with specifications defined in various API standards, primarily API Spec 10A. Pozzolan is an additive to allow reinforcement of the cement slurry (Table 19).

Table 19. Intermediate section fluid placement in annulus.

Fluid Name	Top MD ft	Bottom MD ft	Length ft	Volume bbl	Cement Sacks	Surface Density lb/gal
9.2 ppg Drilling Mud	0.0	0.0	0.0	0.0	—	10.00
CW100	0.0	0.0	0.0	60.0	—	8.32
11.5 ppg Lead Class G/Pozzolan	0.0	6,437.0	6,437.0	637.8	1,558	11.50
15.8 ppg Tail Class G	6437.0	7,432.0	1,000.0	99.1	391	15.80

5.2.5.4 Long String Section

The long casing string will be set 100 ft into the Third Panoche shale but may be set higher if an appropriate formation can be found. Cement will be brought back to surface from 10,412 ft TVD without a need for staging equipment. The EverCRETE* CO₂ resistance cement system will only be taken to above the Moreno shale capping formation with a top of 7,332 ft to 7,000 ft.

Class G cement is an API grade cement with specifications defined in various API standards, primarily API Spec 10A. Pozzolan is an additive to allow reinforcement of the cement slurry.

The EverCRETE system has proved to be highly resistant to CO₂ attack in the most extreme laboratory conditions, including environments with wet supercritical CO₂ and CO₂ water saturation in downhole conditions. The system reduces the risk of CO₂-induced degradation of the cement sheath that could lead to leakage. It can be incorporated into standard primary cementing operations for zonal isolation of new CO₂ injection wells. The system can also be used to plug and abandon existing wells drilled through the storage zone to reestablish long-term well integrity (Table 20).

Table 20. Long-string section fluid placement in annulus.

Fluid Name	Top MD ft	Bottom MD ft	Length ft	Volume bbl	Cement Sacks	Surface Density lb/gal
Drilling Fluid	0.0	0.0	0.0	0.0	—	9.40
10.5 MPE w Surfactant	0.0	0.0	0.0	5.1	—	10.50
10.5 MPE w Surfactant	0.0	0.0	0.0	44.9	—	10.50
10.5 MRF	0.0	0.0	0.	224.7	—	10.50
11.6 ppg Lead Class G/Pozzolan	0.0	7,000.0	7,000.0	296.8	725	11.60
12.5 ppg EverCRETE system	7,000.0	10,412.0	3,412.0	170.6	852	12.53

6. Pre-Operational Logging and Testing

Pre-Operational Logging and Testing GSDT Submissions

GSDT Module: Pre-Operational Testing

Tab(s): Welcome tab

Please use the checkbox(es) to verify the following information was submitted to the GSDT:

Proposed pre-operational testing program [40 CFR 146.82(a)(8) and 146.87]

These data are not available at this time because the characterization wells have not yet been drilled. These data will be submitted in future phases of this project. Refer to Attachment G: Construction Details (Schlumberger, 2021g) for the pre-injection test plan.

7. Well Operation

Well operations will always be monitored for pressure and temperature with surface and downhole sensors along with surface mass flow sensors. Periodic assessment of the chemical and physical characteristics of the injectorate will also be done. More details on this can be found in Attachment C: Testing and Monitoring Plan (Schlumberger, 2021c). The plan is to have the pressure, temperature and mass flow information systems connected to automated controls to assist with shut down or flow controls if certain critical parameters are reached such as maximum flow rate or pressures and temperatures at surface and downhole as well as minimum maximum flow rate or pressures and temperatures. This system is currently not defined as more details are needed to properly implement.

For the preconstruction phase, the fracture pressure at the center of perforations is estimated to be 6,134 psi at 9,437 ft using a gradient of 0.65 psi/ft. A safe formation injection pressure of 90% of the fracture gradient would be 5,677 psi. The surface injection pressure equivalent for the safe formation injection pressure assuming a 0.376 psi/ft gas gradient (more accurate information will be gained during operation with comparison of downhole and surface sensors) would be 2,026 psi injection pressure to reach the 90% fracture gradient of 5,677 psi at the perforations downhole. The PIPESIM* steady-state multiphase simulation software was used for the flow simulation within the wellbore. These parameters may change as more information is gained during the evaluation phase of the well's geophysical properties during the drilling of the characterization well.

The expected composition of the injected fluids can be found in Table 10. However, samples of the injected fluids will be evaluated per the Testing and Monitoring Plan (Schlumberger, 2021c) as part of the continuous monitoring plan during the injection period.

Protection of the USDWs are the forefront of the well design. There will be three casing and cement barriers between the injected fluids and the USDWs at 1,609 ft. Cement barriers are designed to be substantial to reduce the risk of cement channeling and ensure coverage is complete and through. In addition to multiple barriers, there will be pressure gauges on the wellhead of the outer annulus to monitor for pressure to make sure there is no breakdown in

the cement integrity. With UIC Program Director approval, the annulus between the tubing and long string will be filled with an estimated 9.4-ppg NaCl brine to provide corrosion and scaling resistance, oxygen sequestering, and microbial growth inhibition. A pressure system will be applied at the wellhead to fulfill the requirement of the tubing annulus pressure be greater than the injection pressure. This will also assist in determining if fluid levels in the tubing annulus are being maintained and if the packer seals are functioning properly.

Strict guidelines for well maintenance will be enforced with sufficient preplanning of the operations to be done to insure well integrity will be maintained before a job is started. During well maintenance, daily logs will be kept of processes completed and issues encountered so a review process can be done to improve operations.

In the event a loss of well integrity or operational control is encountered, an immediate investigation will begin to identify as expeditiously as possible the cause of the shutoff. If, upon such investigation, the well appears to be lacking mechanical integrity, or if otherwise indicates that the well may be lacking mechanical integrity, the following will occur:

1. Immediately cease injection.
2. Take all steps reasonably necessary to determine whether there may have been a release of the injected carbon dioxide stream or formation fluids into any unauthorized zone.
3. Notify the Director within 24 hours.
4. Restore and demonstrate mechanical integrity to the satisfaction of the Director prior to resuming injection.
5. Notify the Director when injection can be expected to resume.

Additional details are in Attachment F: Emergency and Remedial Response Plan (Schlumberger, 2021f).

7.1 Operational Procedures [40 CFR 146.82(a)(10)]

To achieve the target injection rate, the injection pressure must be greater than the minimum bottomhole pressure required to drive the CO₂ into the reservoir formation, but the injection pressure must be maintained below the maximum safe pressure to avoid fracturing. The minimum bottomhole pressure to provide the required flow rate into the Panoche sandstone was determined by subsurface reservoir modeling. The maximum safe bottomhole pressure was specified as 90% of the rock's fracture pressure ($0.9 \times 0.65 \text{ psi/ft} = 0.585 \text{ psi/ft}$) at the depth where the CO₂ is injected. For conservatism, the required injection pressure was calculated based on the assumption that the required bottomhole pressure is equal to the maximum safe bottomhole pressure. Maximum bottomhole injection pressure is injection depth \times 0.585 psi/ft.

A steady-state, one-dimensional flow model was used to calculate the pressure drop along a series of segments of the well. Pressure changes from frictional loss, gravity head, and acceleration of the flow are included in the model. The CO₂ density is calculated from the pressure and temperature using the CO₂ state equation of Peng-Robinson (1976). The CO₂ is assumed to be a liquid or supercritical fluid and the calculation stops if two-phase conditions occur. The internal energy at the end of a pipe segment was calculated from the energy equation accounting for the heat transfer from or into the CO₂ stream from the surrounding soil or rock,

change in potential energy due to pressure and elevation, and kinetic energy of the flow. Changes in the internal energy and temperature of the CO₂ with depth cause gradual changes in density, which, in turn, change the velocity and pressure drop. If the friction pressure drop is large (e.g., high-velocity flow through small injection tubing), fluid expansion is significant as it moves down the pressure gradient. The resulting cooling effect can potentially have a greater impact on the CO₂ temperature than heat transfer to the surroundings.

Part of the bottomhole pressure required to support the necessary flow into the rock is provided by hydrostatic head associated with the weight of the column of fluid in the well. This depends upon the fluid density, which varies with pressure and temperature because of the compressibility of CO₂. Lower temperature at the wellhead increases the fluid density and decreases the wellhead pressure required to provide the necessary bottomhole pressure. Frictional pressure drop in the injection tubing must also be overcome. High frictional losses associated with undersized tubing would make high wellhead pressures necessary to support a given flow rate. Larger tubing sizes require lower injection pressures but larger wells. Conversely, smaller well and tubing sizes require higher injection pressures.

Wellhead injection pressures were calculated for the following conditions: a flow rate of 958.0 tonnes per day (i.e., assuming 100% of the CO₂ is injected), Injection tubing of 3.5-in and 4.5-in diameter and one surface CO₂ temperature (60.8°F) represent the range of anticipated CO₂ temperatures at the injection. Required injection pressures will be higher in summer than winter due to lower density, leading to less hydrostatic in the fluid column and higher frictional losses because of higher fluid velocities.

Proposed operational procedures are shown in Table 21.

7.2 Proposed Carbon Dioxide Stream [40 CFR 146.82(a)(7)(iii) and (iv)]

CES carbon negative energy (CNE) plants use biomass as feedstock to produce syngas which passes through a gas separation unit to produce hydrogen for transportation fuel. The hydrogen-depleted syngas then passes through a CES proprietary gas generator to produce a pure stream of high-pressure CO₂. CES plans to compress this CO₂ to a supercritical state and inject it deep into the subsurface for geologic sequestration (GS).

The gas stream for injection contains 96.78% CO₂ with some impurities. O₂ is the most notable impurity at 1.15% because it is reactive when redox sensitive minerals are present in the formation. It also requires surface and well components which are resistant to that environment. To understand its effect, O₂ is included in the geochemical models. The current estimate of the gas stream composition is listed in Table 10.

In the preconstruction phase, the exact measurement as to composition, properties, and corrosiveness have not been tested. Well construction materials described in Attachment G: Construction Details (Schlumberger, 2021g) will be reviewed following these tests as well as Attachment C: Testing and Monitoring Plan (Schlumberger, 2021c) and the Quality Assurance and Surveillance Plan (Schlumberger, 2021j).

Table 21. Proposed operational conditions.

Parameters/Conditions	Limit or Permitted Value	Unit
Maximum Injection Pressure		
Surface	2,026	psi
Downhole	5,677	psi
Average Injection Pressure		
Surface	1,042	psi
Downhole	4,212	psi
Maximum Injection Rate	958.9	tonnes/day
Average Injection Rate	958.9	tonnes/day
Maximum Injection Volume and/or Mass	350,000	tonnes/year
Average Injection Volume and/or Mass	350,000	tonnes/year
Annulus Pressure @ Top of Packer	5,777	psi
Annulus Pressure/Tubing Differential @ Packer	100	psi

8. Testing and Monitoring

Testing and Monitoring GSDT Submissions

GSDT Module: Project Plan Submissions

Tab(s): Testing and Monitoring tab

Please use the checkbox(es) to verify the following information was submitted to the GSDT:

Testing and Monitoring Plan [40 CFR 146.82(a)(15) and 146.90]

The above requested documents have been included in the file submission, Attachment C: Testing and Monitoring Plan (Schlumberger, 2021c). These documents address the rule requirements for the above EPA citations.

9. Injection Well Plugging

Injection Well Plugging GSDT Submissions

GSDT Module: Project Plan Submissions

Tab(s): Injection Well Plugging tab

Please use the checkbox(es) to verify the following information was submitted to the GSDT:

Injection Well Plugging Plan [40 CFR 146.82(a)(16) and 146.92(b)]

The above requested documents have been included in the file submission, Attachment D: Injection Well Plugging Plan (Schlumberger, 2021d). These documents address the rule requirements for the above EPA citations.

10. Post-Injection Site Care (PISC) and Site Closure

PISC and Site Closure GSDT Submissions

GSDT Module: Project Plan Submissions

Tab(s): PISC and Site Closure tab

Please use the checkbox(es) to verify the following information was submitted to the GSDT:

PISC and Site Closure Plan [40 CFR 146.82(a)(17) and 146.93(a)]

GSDT Module: Alternative PISC Timeframe Demonstration

Tab(s): All tabs (only if an alternative PISC timeframe is requested)

Please use the checkbox(es) to verify the following information was submitted to the GSDT:

Alternative PISC timeframe demonstration [40 CFR 146.82(a)(18) and 146.93(c)]

The above requested documents have been included in the file submission, Attachment E: Post-Injection Site Care and Site Closure Plan (Schlumberger, 2021e). These documents address the rule requirements for the above EPA citations. CES is not requesting an Alternative PISC timeframe.

11. Emergency and Remedial Response

Emergency and Remedial Response GSDT Submissions

GSDT Module: Project Plan Submissions

Tab(s): Emergency and Remedial Response tab

Please use the checkbox(es) to verify the following information was submitted to the GSDT:

Emergency and Remedial Response Plan [40 CFR 146.82(a)(19) and 146.94(a)]

The above requested documents have been included in the file submission, Attachment F: Emergency and Remedial Response Plans (Schlumberger, 2021f). These documents address the rule requirements for the above EPA citations.

12. Injection Depth Waiver and Aquifer Exemption Expansion

Injection Depth Waiver and Aquifer Exemption Expansion GSDT Submissions

GSDT Module: Injection Depth Waivers and Aquifer Exemption Expansions

Tab(s): All applicable tabs

Please use the checkbox(es) to verify the following information was submitted to the GSDT:

Injection Depth Waiver supplemental report [40 CFR 146.82(d) and 146.95(a)]

Aquifer exemption expansion request and data [40 CFR 146.4(d) and 144.7(d)]

CES is not requesting an Injection Depth Waiver or Aquifer Exemption Expansion.

13. Other Information

There is no additional information that is not specifically requested/required useful for the permit application.

14. Approval

This preconstruction application and the associated attachment documents were prepared by a multidisciplinary team at Schlumberger and approved by Schlumberger technical leads (Table 22.) This document and attachments were delivered to CES.

- Schlumberger, Attachment A: Summary of Requirements Class VI Operating, 2021
- Schlumberger, Attachment B: Area of Review and Corrective Action Plan, 2020
- Schlumberger, Attachment C: Testing and Monitoring Plan, 2021
- Schlumberger, Attachment D: Injection Well Plugging Plan, 2021
- Schlumberger, Attachment E: Post-Injection Site Care and Site Closure Plan, 2021
- Schlumberger, Attachment F: Emergency and Remedial Response Plan, 2021
- Schlumberger, Attachment G: Construction Details Clean Energy Systems Mendota, 2021
- Schlumberger, Attachment H: Financial Assurance Demonstration, 2021
- Schlumberger, Class VI Permit Application Narrative, 2021
- Schlumberger Quality Assurance and Surveillance Plan, 2021

Table 22. Approval.

Name	Title	Signature	Date
Randal Utech	Advisor Geoscientist		January 31, 2020

Name	Title	Signature	Date
Ernest Gomez	Advisor Reservoir Geology		June 17, 2021

15. Disclaimer Statement

Disclaimer Statement

Any interpretation, research, analysis, data, results, estimates, or recommendation furnished with the services or otherwise communicated by Schlumberger to Clean Energy Systems at any time in connection with the services are opinions based on inferences from measurements, empirical relationships, and/or assumptions, which inferences, empirical relationships and/or assumptions are not infallible, and with respect to which professionals in the industry may differ. Accordingly, Schlumberger cannot and does not warrant the accuracy, correctness, or completeness of any such interpretation, research, analysis, data, results, estimates, or recommendation. Clean Energy acknowledges that it is accepting the services "as is", that Schlumberger makes no representation or warranty, express or implied, of any kind or description in respect thereto. Specifically, Clean Energy acknowledges that Schlumberger does not warrant that any interpretation, research, analysis, data, results, estimates, or recommendation is fit for a particular purpose, including but not limited to compliance with any government request or regulatory requirement. Clean Energy System further acknowledges that such services are delivered with the explicit understanding and agreement that any action taken based on the services received shall be at its own risk and responsibility and no claim shall be made against Schlumberger as a consequence thereof.

To the extent permitted by applicable law, Clean Energy Systems shall not provide this report to any third party in connection with raising finance or procuring investment (other than pursuant to an equity capital raising on a public market) without a No Reliance Letter first being completed and signed by the third party and provided to Schlumberger. The form of the No Reliance Letter being agreed to by both Clean Energy Systems and Schlumberger. Subject to this requirement and upon full payment of applicable fees, copyright ownership in this report shall vest with Clean Energy Systems. Schlumberger grants no title or license or right to Clean Energy Systems to use Schlumberger's Intellectual Property except as necessary for Clean Energy Systems to use the report.

16. References

Bartow, A. J., & Nilsen, T. H. (1990). *Review of the Great Valley Sequence, eastern Diablo Range and northern San Joaquin Valley, central California*. USGS Open-File Report 90-226.

CalGEMS. (2020). *Well Finder*. Retrieved from <https://maps.conservation.ca.gov/doggr/wellfinder/#/>

California Department of Conservation, Division of Oil, Gas and Geothermal Resources. (1998). *CALIFORNIA OIL & GAS FIELDS Volumes I, II, & III*.

California Department of Water Resources. (n.d.). Retrieved from water.ca.gov/Library/Other-DWR-Portals

- California Department of Water Resources. (2021). *Water Data Library (WDL) Station Map*. Retrieved from <https://wdl.water.ca.gov/waterdatalibrary/Map.aspx>
- California Geological Survey. (2010). *Fault Activity Map of California*. Retrieved from <https://maps.conservation.ca.gov/cgs/fam/>
- CEMA. (2010). *Central Coast ShakeOut Area - Historical Epicenters*. Retrieved from https://www.shakeout.org/california/images/Central_Coast_epicenters_map.jpg
- Chanchani, S., Zoback, M., & Barton, C. (2003). A case study of hydrocarbon transport along active faults and production-related stress changes in the Monterey formation, California. *Geological Society, London, Special Publications*, 209, 17-26.
doi:<https://doi.org/10.1144/gsl.sp.2003.209.01.03>
- Chiaromonte, L., Zoback, M. D., Friedmann, J., & Stamp, V. (2008). Seal integrity and feasibility of CO₂ sequestration in the Teapot Dome EOR pilot: Geomechanical site characterization. *Environmental Geology*, 54, 1667-1675.
doi:<https://doi.org/10.1007/s00254-007-0948-7>
- Davis, T., Bennett, G., Metzger, L., & al., e. (2018). *Data analyzed for the preliminary prioritization of California oil and Gas fields for regional groundwater monitoring*. Retrieved from USGS: <https://doi.org/10.5066/F7FJ2DV3>
- DOE. (2015). *Carbon Atlas - Fifth Edition*. NETL, Department of Energy. Retrieved from <https://www.netl.doe.gov/coal/carbon-storage/strategic-program-support/natcarb-atlas>
- DOGGR. (1992). *CALIFORNIA OIL & GAS FIELDS Volumes I, II, & III*.
- DOGGR. (2019). <https://www.conservation.ca.gov/dog>. Retrieved from Division of Oil, Gas, and Geothermal Resources.
- EPA. (2018). *Geologic Sequestration of Carbon Dioxide Underground Injection Control (UIC) Program Class VI Implementation Manual for UIC Program Directors*.
- EPA. (2019a). *Class VI Guidance Documents*. Retrieved from Class VI Guidance Documents: <https://www.epa.gov/uic/class-vi-guidance-documents>
- EPA. (2019b). *Underground Injection Control*. Retrieved from <https://www.epa.gov/uic/class-ii-permit-application-checklist>
- Gillespie, J., Kong, D., & Anderson, S. D. (2017). Groundwater salinity in the southern San Joaquin Valley. *AAPG Bulletin*, 101(8), 1239–1261.
doi:<https://doi.org/10.1306/09021616043>
- Han, D., Nur, A., & and Morgan, D. (1986). Effects of porosity and clay content on wave velocities in sandstone. *Geophysics*, 51(11), 2093-2107.
doi:<https://doi.org/10.1190/1.1442062>

- Herron, M. M. (1987). Estimating the Intrinsic Permeability of Clastic Sediments from Geochemical Data. *SPWLA 28th Annual Logging Symposium*.
- Hosford Scheirer, A., & Magoon, L. (2007a). *Age, Distribution, and Stratigraphic Relationship of Rock Units in the San Joaquin Basin Province, California*. USGS Professional Paper 1713, Chapter 5.
- Hosford Scheirer, A., & Magoon, L. (2007b). *Winters-Domengine Total Petroleum System—Northern Nonassociated Gas Assessment Unit of the San Joaquin Basin Province*. USGS Professional Paper 1713, Chapter 21.
- IHS. (2019). *IHS Markit*. Retrieved from Enerdeq, Lognet: <https://ihsmarkit.com/index.html>
- McGuire, D. (1988). Depositional framework of the Upper Cretaceous-lower Tertiary Moreno Formation, central San Joaquin basin, California. In S. Graham, & H. Olson, *Studies of the Geology of the San Joaquin Basin*. Pacific Section, SEPM, Book 60.
- Palandri, J. L., & Kharaka, Y. K. (2004). *A compilation of rate parameters of water-mineral interaction kinetics for application to geochemical modeling*. USGS Open File Report OF 2004-1068.
- Peng, D. Y., & Robinson, D. B. (1976). A New Two-Constant Equation of State. *Industrial and Engineering Chemistry: Fundamentals*, 15(1), 59–64.
doi:<https://doi.org/10.1021/i160057a011>
- Schlumberger. (2021a). *Attachment A: Summary of Requirements Class VI Operating and Reporting Conditions*.
- Schlumberger. (2021b). *Attachment B: Area of Review and Corrective Action Plan 40 CFR 146.84(b) Clean Energy Systems Mendota*.
- Schlumberger. (2021c). *Attachment C: Testing and Monitoring Plan 40 CFR 146.90 Clean Energy Systems Mendota*.
- Schlumberger. (2021d). *Attachment D: Injection Well Plugging Plan 40 CFR 146.92(B) Clean Energy Systems Mendota*.
- Schlumberger. (2021e). *Attachment E: Post-Injection Site Care and Site Closure Plan 40 CFR 146.93(A) Clean Energy Systems Mendota*.
- Schlumberger. (2021f). *Attachment F: Emergency and Remedial Response Plan 40 CFR 146.94(A) Clean energy Systems Mendota*.
- Schlumberger. (2021g). *Attachment G: Construction Details Clean Energy Systems Mendota*.
- Schlumberger. (2021h). *Attachment H: Financial Assurance Demonstration 40 CFR 146.85 Clean Energy Systems Mendota*.

- Schlumberger. (2021i). *Class VI Permit Application Narrative 40 CFR 146.82(A) Clean Energy Systems Mendota*.
- Schlumberger. (2021j). *Quality Assurance and Surveillance Plan*.
- SEI. (2019). Seismic Exchange Inc.
- Smith, V., & Jaques, P. (2016). Illinois Basin – Decatur Project pre-injection microseismic analysis. *International Journal of Greenhouse Gas Control*, 54, 362–377.
doi:<https://doi.org/10.1016/j.ijggc.2015.12.004>
- Suchsland, R. J., & Peters, J. F. (1997). Exploration and Development of the Blewett Trend, Northern San Joaquin Basin, California. In L. Knauer, *Geology of the Northern San Joaquin Basin Gas Province*. Pacific Section American Association of Petroleum Geologists Volume MP 43. doi:<https://doi.org/10.32375/1997-mp43.3>
- TGS. (2019). TGS-NOPEC Geophysical Company ASA.
- USGS. (1983). *The Coalinga, California, Earthquake of May 2, 1983*. USGS. Retrieved from <https://pubs.usgs.gov/pp/1487/report.pdf>
- USGS. (2003). In *Petroleum Systems and Geologic Assessment of Oil and Gas in the San Joaquin*.
- USGS. (2005). *National Assessment of Oil and Gas Project - San Joaquin Basin Province (010) Boundary*. (C. R. Team, Producer) Retrieved from <https://catalog.data.gov/dataset/national-assessment-of-oil-and-gas-project-san-joaquin-basin-province-010-boundary>
- USGS. (2019a). *Earthquake Hazards Program*. Retrieved from <https://earthquake.usgs.gov/>
- USGS. (2019a). *USGS California Geological Map Data*. Retrieved from <https://mrdata.usgs.gov/geology/state/state.php?state=CA>
- USGS. (2019c). *U.S. Quarternary Faults*. Retrieved from USGS Geologic Hazard Science Center:
<https://usgs.maps.arcgis.com/apps/webappviewer/index.html?id=5a6038b3a1684561a9b0aadf88412fcf>
- USGS. (2021). *ANSS Comprehensive Earthquake Catalog (ComCat) Documentation*. Retrieved from USGS: <https://earthquake.usgs.gov/data/comcat/>
- Vernik, L., & Zoback, M. (1989). Effects of rock elastic and strength properties in estimation of the state of stress at depth. *Proc International Symposium on Rock at Great Depth, Pau 28–31 August 1989V2*, P1033–1040. doi:[https://doi.org/10.1016/0148-9062\(91\)93462-F](https://doi.org/10.1016/0148-9062(91)93462-F)

- Winters, W., Warren, T., & Onyia, E. (1987). Roller bit model with rock ductility and cone offset. *SPE Annual Technical Conference and Exhibition*. Dallas Texas.
doi:<https://doi.org/10.2118/16696-MS>
- Yielding. (2002). Shale Gouge Ratio - calibration by geohistory. *Norwegian Petroleum Society Special Publications*, 1-15. doi:[https://doi.org/10.1016/s0928-8937\(02\)80003-0](https://doi.org/10.1016/s0928-8937(02)80003-0)
- Yielding, G., Freeman, B., & Needham, D. (1997). Quantitative Fault Seal Prediction. *AAPG Bulletin*, 81, 897-917. doi:<https://doi.org/10.1306/522b498d-1727-11d7-8645000102c1865d>
- Zoback, M., Barton, C., Brudy, M., Castillo, D., Finkbeiner, T., Grollimund, B., . . . Wiprut, D. (2003). Determination of stress orientation and magnitude in deep wells. *International Journal of Rock Mechanics and Mining Sciences*, 40, 1049-1076.
doi:<https://doi.org/10.1016/j.ijrmms.2003.07.001>

17. Appendix A: Stratigraphic Nomenclature, San Joaquin Basin

As mentioned previously, one of the challenges in describing the stratigraphy is the inconsistency in naming conventions. The following paragraphs are included here to clarify the stratigraphy of the proposed storage complex.

The depositional models that have been proposed for the northern San Joaquin Basin (Figure 4) describe the depositional setting and expected reservoir or injection zone sandstones for the Mendota_INJ_1 site. The names of the specific target stratigraphic intervals remain problematic because of the inconsistencies in published papers and reports across the basin. This section describes the uncertainty in the naming conventions and stratigraphy for the proposed injection zone, which may represent deltaic shelf deposits, the slope and basin floor fan deposits, or both, and discusses the implications of connection between sands of the two types of deposits. A comprehensive report addressing these inconsistencies is USGS Professional Paper 1713, specifically Chapter 5 (Hosford Scheirer & Magoon, 2007a). The conclusions of this report were summarized with respect to the Mendota study area and present the naming conventions applied to clarify the terminology and to support our choice of stratigraphic nomenclature for the Mendota_INJ_1 site.

Hosford Scheirer and Magoon (Hosford Scheirer & Magoon, 2007a) attempted to apply consistent stratigraphic age, biostratigraphy, and lithostratigraphic boundaries to the geologic column and geological naming conventions in the San Joaquin Basin. As they note, some of the inconsistencies arise from applying similar subsurface correlations and lithofacies names to subsurface stratigraphic units that may not be correlative.

For the late Cretaceous to early Paleocene of the northern Joaquin Basin, Hosford Scheirer and Magoon have separated the late Cretaceous to early Paleocene stratigraphic section into a lower Panoche formation and upper Moreno formation, with the Panoche bracketed between 83.5 to 73.5 Ma and the Moreno from 73.5 to 61 Ma. A lower unconformity separates the base of the section from the Sierran arc basement at 120 Ma from an upper unconformity at the top the section in the middle Eocene. The entire section can be divided into a more proximal stratigraphic section representing the deltaic deposition of the Starkey sands and the more distal slope and basin floor fan deposits (Figure 59).

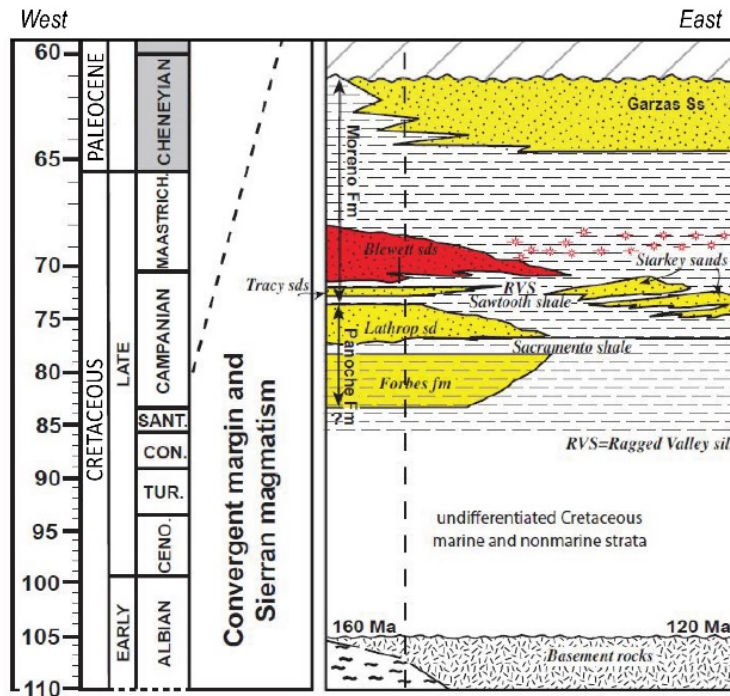


Figure 59. Stratigraphic column from northern San Joaquin Basin showing Cretaceous to Lower Paleocene section; modified from (Hosford Scheirer & Magoon, 2007a).

The Panoche formation includes, in the more distal section to the west, a lower Forbes sandstone overlain by the Sacramento shale followed by the Lathrop sandstones. There are no proximal sands in the east that are time equivalent or correlative to the deeper water, more distal Panoche in the west. In subsurface wells, the Panoche sands have been labeled as First, Second, Third, and Fourth Panoche sands. These picks may or may not correspond to the specific sands labeled but may be sands within these members.

The Sawtooth shale overlies the Lathrop sands and is the lowest member of the Moreno formation. This shale is overlain by the Tracy sands followed by the time-transgressive Ragged Valley silt and the Blewett sands, which underlie the Moreno shale, which is a regional top seal. The Cretaceous to Paleocene widespread Garza sandstone is the youngest unit in the Moreno formation.

Unlike the Panoche formation, the members of the Moreno formation to the west are coeval to sands in a more proximal location to the east, which are the Starkey sands. These are interpreted as three principal sand units often identified as Starkey one, two, and three, and they correlate distally with the Sawtooth shale, Tracy sands, and Ragged Valley silt. In some instances, the lower Starkey sands are considered coeval with the Panoche Lathrop sands.

Although Hosford Scheirer and Magoon (Hosford Scheirer & Magoon, 2007a) provide a current interpretation of the stratigraphic correlations for the Cretaceous section in the northern San Joaquin basin, there remains debate about which formations specific sandstones should be assigned to, or, in the subsurface, even which sandstones are intersected by the wells. For

instance, Chapter 21 in USGS Professional Paper 1713 (Hosford Scheirer & Magoon, 2007b) has reproduced historical maps and well sections, such as that from the Gill Ranch field, where the Starkey sands have been labeled as Panoche first to fourth Panoche. In fact, the historical log and cross-sectional images in Chapter 21 of the USGS report highlight the inconsistencies in the labeling of the stratigraphic sections.

Given the inconsistency in the stratigraphic names in the subsurface and to avoid confusion by incorrectly labeling a sandstone target, it was decided to label all sandstones as Panoche, which may include the proximal and more distal sands from the Moreno and Panoche formations as described in Hosford Scheirer and Magoon (Hosford Scheirer & Magoon, 2007a). In this case, the first sandstone encountered beneath the Moreno shale penetrated by the well is labelled as First Panoche sand with an incremental increase in the number for each subsequent sandstone. Based on the stratigraphic setting, description, and local well constraints, there is confidence that sands will be encountered. It cannot be determined with accuracy, however, that the more distal or proximal sands or something in between will be intersected. For instance, it might be possible that the well intersects the First Panoche sand, the top of the Moreno Blewett sandstone, but subsequent sands are the distal terminations of the Starkey sands. If the section intersected is the more distal sands, there is a greater chance that these will terminate updip into shales. However, if the Starkey sands are intersected by the well, there may be communication updip. This is an unlikely scenario given the proposed well distance from the paleo shelf edge. However, to consider this riskier scenario for updip CO₂ migration, sands connected from the proximal to the distal locations need to be modeled (Figure 4c).